REGIONE AUTONOMA DELLA SARDEGNA

UNIVERSITA' DEGLI STUDI DI CAGLIARI

uniss

UNIVERSITÀ DEGLI STUDI DI SASSARI

Università degli Studi di Cagliari Università degli Studi di Sassari

PHD DEGREE

Chemical Science and Technology

Cycle XXXII

TITLE OF THE PHD THESIS

Carbon-based nanostructures in hybrid materials for detection and removal of water pollutants

Scientific Disciplinary Sector(s)

ING-IND/22

PhD Student:	Róbert Ludmerczki
Coordinator of the PhD Programme:	Prof. Stefano Enzo
Supervisor:	Prof. Luca Malfatti
Co-supervisor:	Dr. Laura Borgese

Final exam. Academic Year 2018 - 2019

Thesis defence: June - July 2020 Session

Édesanyámnak…

Table of contents

Preface

The thesis is mainly focused on the better understanding of carbon dots (C-dots) formation in bottom-up syntheses, by identifying the key chemical processes and correlating them to the observed fluorescence. Therefore, several types of C-dots were studied, by systematically varying the used (molecular) precursor ratios and reaction times. Selected samples were surface functionalized by organosilanes to reveal the role of the C-dots surface functional groups in the overall photoluminescence. As better understanding of the ongoing processes finally achieved, the synthesized C-dots were applied in photocatalysis experiments by combining them with titania and an appropriate C-dot was tested as a nitrite ion sensor.

Chapter 1 gives an introduction of syntheses, purification, properties and applications of C-dots, and summarizes the aims of the present thesis.

Chapter 2 details the analytical methods used through the thesis.

Chapter 3. As a starting point of the experimental work, the common laboratory scale bottom-up synthesis methods for obtaining C-dots were compared, to find optimal procedures for the following experiments.

Chapter 4.1. Pyrolysis of pure citric acid was investigated, the key intermediates identified and surface functionalization with APTES was performed, resulting a blue shift in the PL emission. These findings serve as a base for the following N-doped citric acid based C-dots.

Chapter 4.2. Reaction of citric acid and tris(hydroxymethyl)aminomethane (Tris) yielded strongly fluorescent products in 10-20 minutes reaction times via a polymerization process. APTES functionalization did not result a blue shift, while significant increase in the PL was observed.

Chapter 4.3 was devoted to the peculiar C-dots formed upon reaction of citric acid and urea. The observed dual emission was tuned by investigating the effect of precursor ratios on the reaction and on the PL emission spectra. Effects of APTES functionalization was also investigated.

Chapter 4.4 describes the synthesis and the application of citric acid based C-dots in co-precipitated titania/C-dots hybrids for photocatalytic degradation of Rhodamine B.

Chapter 5.1. Synthesis of C-dots from *p*-phenylenediamine in solvothermal reactions were performed, and the crude products exhibited PL emission at 600 nm in ethanol. The mixture was successfully stabilized in acidic water, which greatly influenced the PL properties. Surface

functionalization with 3-(triethoxysilyl)propyl isocyanate was successful, as their reaction was confirmed by slowly changing PL emission.

C*hapter 5.2* utilizes the *p*-phenylenediamine derived C-dots in acidic aqueous media as a selective nitrite ion sensor in natural water samples.

The final paragraphs are dedicated to *conclusions, list of acronyms, list of publications, acknowledgements and bibliography*.

1. Introduction to carbon dots

Carbon dots (C-dots, CDs) are just teenagers in the family of carbonaceous materials as they were discovered in 2004 during the purification of single wall carbon nanotubes (SWCNTs)[1] and emerged into the spotlight of nanoscience due to their optimal properties for several applications. C-dots are carbon-made or carbon-rich nanosized (generally spherical) objects with an average diameter around or below 10 nm[2,3] and known for their relatively strong fluorescence characteristics. C-dots are often derived from non-toxic organic compounds and appear stable in aqueous media which is an important factor in terms of biological applications.[4] Surface engineering through chemical processes plays a significant role for C-dots in diverse applications like chemical sensing (e.g. explosive detection), food safety, drug delivery, bioimaging, energy conversion and photocatalysis.

Chemical and photophysical properties of the C-dots vary by tuning their shapes and sizes and also by doping with heteroatoms such as oxygen, nitrogen, phosphorus, sulfur, and boron.[5] Furthermore, the high quantum yields, photostability, biocompatibility, low toxicity, good conductivity, water solubility, and environmental friendliness of C-dots gives advantage over other types of the well-recognized quantum dots (QDs) like graphene quantum dots (GQDs), metal oxides (TiO_2, ZnO), and inorganic quantum dots (CdSe, ZnO-PbS, CuInS/ZnS). In fact, noncarbon QDs are not so much universal in their applications fields, compared to C-dots, mainly because of their serious environmental and health issues.[6,7] C-dots may be synthesized from (cheap and abundant) natural and synthetic organic precursors, and even from waste materials and renewable biomass. The frequently used synthesis approaches are hydrothermal/solvothermal, ultrasonic and microwave irradiation, laser ablation, electrochemical, arc discharge, and pyrolysis.[8]

Structure and properties

C-dots are the youngest members in the family of nanoworld. They are usually spherically shaped with an average diameter less than 10 nm.[4] GQDs have exquisitely sp^2-hybridized carbons, while C-dots are composed of the mixture of sp^2 and sp^3 carbon networks.[9] Moreover, they can be easily functionalized as carboxyl, hydroxyl, carbonyl, amino, and epoxy groups on their surfaces offer various possibilities for chemically binding both inorganic and organic moieties.[10] These functionalities allow the surface of C-dots to expose either hydrophobic or hydrophilic character, which provide their stability in different solvents, most importantly in water.[11] While pure carbon nanoparticles do not exhibit photoluminescent activities, their surface modification may lead to a strong emission.[8] Surface engineering of C-dots by different functionalities or passivating agents and their interaction with solvents provide simple methods for changing their optical properties.[12]

1.1. Preparation

Numerous synthetic methodologies have been developed for obtaining C-dots with various functionalities and photophysical properties. Synthesis of C-dots are generally categorized as (a) "bottom-up" and (b) "top-down" approaches (**figure 11.1**).

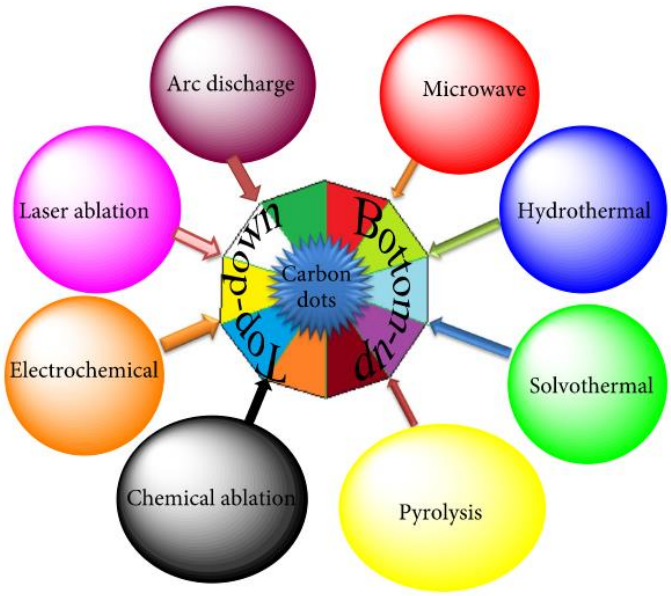

Figure 11.1. Synthetic methods for the preparation of C-dots. Reproduced from reference[13] (open access).

Bottom-up approach

In the "bottom-up" methodology, C-dots are synthesized from molecules through chemical reactions such as condensation, polymerization, decarboxylation, dehydration etc. typically by using microwave irradiation, hydrothermal synthesis or pyrolysis.

Microwave irradiation

Microwave- (MW-) assisted syntheses are widely used due to their time-saving, energy-efficient, and eco-friendly nature. The carbonization of organic molecules usually occur through microwave heating in very short reaction times. In 2009, the first reported C-dots obtained with MW assistance from carbohydrates and excellent photophysical properties have been achieved in a short reaction.[14] Another photoluminescent C-dots were obtained from glycerol and a diamine derivative by MW irradiation, providing a moderately high quantum yield (QY) due to the introduction of amino groups ($-NH_2$) on the surface of C-dots.[15] C-dots with QY of 46% were produced by MW assistance from silkworm chrysalis[16] and used for bioimaging due to their low toxicity. Recently, MW assisted reaction of citric acid and tris(hydroxymethyl)aminomethane yielded C-dots with exceptionally high 99% QY.[17] The synthesized particles were used for staining E. coli cells.

Hydrothermal/solvothermal method

One of the most promising method in recent years for the synthesis of C-dots due to their easy operational technique. In a typical procedure, a solution of organic precursors (in water or organic solvents) are sealed in the reactor and heated to high temperature and pressure. The first reported synthesis used a one-pot hydrothermal reaction to make C-dots from ascorbic acid in ethanol. A QY of 6.79% and an average particle sizes of ~2 nm were obtained.[18] Nitrogen and sulfur co-doped C-dots obtained by the reaction of methionine in a hydrothermal reactor[19] and exhibited selective detection of heavy metal ions in water. C-dots from sweet potato, as a natural source of carbon, was also used by a hydrothermal method, resulting high QY and utilized for detection of Fe^{3+} ions.[20] C-dots from hyaluronic acid with surface-modification by polyethylenimine yielded a higher QY of 26% and used for tumor targeting and gene delivery.[21]

Pyrolysis (thermal decomposition, carbonization)

It is a facile method to obtain C-dots from organic precursors, as chemical reactions carried out at very high temperature. C-dots of average diameter ~6 nm were obtained by the pyrolysis of citric acid at 180°C.[22] C-dots were also prepared from hair (keratin) by a pyrolysis method at 200°C

for 24 hours and used in the detection of Hg^{2+} with high sensitivity and selectivity.[23] Highly photoluminescent nitrogen-doped C-dots synthesized from guanidinium chloride and citric acid by pyrolysis and fluorescence quenching observed in the presence of Fe^{3+}.[24]

Top-down approach

As an opposite of the bottom-up method, C-dots or GQDs are synthesized by breaking down bigger carbon rich structures such as nanodiamonds,[25] graphite,[26] carbon nanotubes,[27] carbon soot,[28] or activated carbon,[29] typically by the use of laser ablation, (electro)chemical oxidation, arc discharge method or ultrasonication .[4,30]

Electrochemical method

The electrochemical method is used for the preparation of ultrapure C-dots from larger substances like carbon nanotubes, graphite or carbon fibers in an electrolytic process. The first reported C-dots were obtained from multi-walled carbon nanotubes in the presence of tetrabutylammonium perchlorate.[27] Water soluble pure C-dots were synthesized by an electrochemical method using graphite as electrode in the presence of a phosphate buffer at neutral pH and applied as a potential biosensor. Crystalline C-dots made by an electrochemical method from graphite exhibited size-dependent upconversion photoluminescence (PL).[31]

Laser ablation

This technique has been widely used for preparing C-dots of different sizes. In the laser ablation route, the organic macromolecules or carbon rich materials exposed to laser radiation in continuous wave or in pulsed mode, while nanosized carbon(ized) particles detach from the larger molecule. Application of this method was first reported in 2006, by using graphite powder as precursor[26] as they synthesized C-dots upon excitation from a Nd:YAG (1064 nm, 10 Hz) laser in argon at 900°C. Photoluminescent C-dots of 3 nm size have been obtained by a laser irradiation of carbon glassy particles in the presence of polyethylene glycol and applied for bioimaging.[32]

Arc discharge

Electrical discharge between two graphite electrodes results the formation of small carbon fragments or C-dots. C-dots were derived from SWCNTs by arc discharge method with bright PL in the blue-green region.[33] Boron- and nitrogen-doped C-dots were also synthesized from graphite while B_2H_6 was used for doping boron and NH_3 for nitrogen.[34]

Ultrasonication

Ultrasonic treatment is also a convenient method as the large carbon materials can be broken down by high energy ultrasound. White light emitting fluorescent C-dots were fabricated from oligomer-polyamide resin by ultrasonic treatment. The as-prepared C-dots were well dispersed, had low crystallinity, and abundant functional groups on the surface.[35]

Currently, as a wide range of synthetic methods are available to obtain fluorescent C-dots, we can finally turn our attention to their reliable and environmentally friendly production. The conventional synthetic approaches often require toxic or expensive reagents as precursors and abundant (organic) solvents or sophisticated equipment. Hydrothermal/solvothermal synthesis, even though one of the most commonly reported method, requires a large amount of heat energy since the reaction temperature is usually around or above 200°C for prolonged reaction times, and additionally, the heavy, pressure-resisting equipment (pressure tube, autoclave) has to be simultaneously heated up to high temperatures. The electrochemical methods use electric energy in prolonged syntheses to obtain C-dots, usually in very small amounts. Chemical oxidation, as a common synthesis approach, requires the use of a strong oxidizing agents (strong alkali or acid) during the synthesis,[36] which raises environmental issues as it is difficult to thoroughly neutralize. Consequently, these conventional approaches should not be favored for scaled-up or mass production of C-dots as they do not meet the requirements of green chemistry.[37]

Even though, the top-bottom approach provides better control of the C-dots composition and morphology[38] as often pure carbon (e.g. carbon nanotubes) used as precursors, the fast and simple bottom-up synthesis methods yield much more fluorescent C-dots in (very) short reaction times, which makes their production energy efficient even in large scale syntheses. Both synthetic approaches can make use of renewable biomass or even waste materials to lower the environmental footprint, but to be able to follow the formation of C-dots by various analytical techniques in fast, economical and preferably high volume syntheses, which can also provide a variety of surface functional groups for further surface modifications, we finally turned our focus on the bottom-up synthesis methods, starting from commercial, abundant and environmentally friendly pure chemicals. As a starting point of experiments, chapter 3 was devoted to the comparison of common synthetic methods by simply focusing on the archived fluorescence properties, especially on its PL intensity / mass unit values upon varying the synthesis methods, the precursor ratios and the reaction time in a model system, made of citric acid and Tris, while the reaction temperature was standardized at the moderate 180°C (even tough temperature is an important reaction parameter, and its change can have

a great influence on the products' properties). Moreover, this reaction temperature also seemed optimal to follow the gradual reaction process (slow or moderate carbonization) in chapter 4. Such a systematic comparison of methods and parameters of the same reaction for building up C-dots is hardly found in the literature.

1.2. Purification

Generally, the purity (size- and chemical homogeneity) is a pivotal question in the case of C-dots, and often neglected in relevant articles. The crude C-dots obtained by different methods usually coupled with an immediate separation/purification step in most studies and usually capillary electrophoresis or chromatographic techniques (e.g. TLC, normal or reverse phase HPLC, column chromatography, size exclusion chromatography), centrifugation, extraction and dialysis[39] alone or in combination used for this purpose. The degree of purification, and the consequent loss of (still molecular, or on the contrary, oversized aggregated, or tar-like) materials greatly influence the final product's properties, while exact reproduction of the conditions of purification is difficult, which can undoubtedly influences the conclusions of the experiments. To exclude this uncertainty, and to have the whole picture of the ongoing chemical processes of building up the C-dots, we decided to always analyze the crude products and we intentionally avoided any purification step after a few preliminary work-up attempt by column chromatography (see TLC as its 2D imitation – **figure 12.1**) and dialysis. Both method proved to be very inconvenient and ineffective, therefore, instead, we focused on the possible applications of the crude C-dots in chapters 4.4 and 5.2.

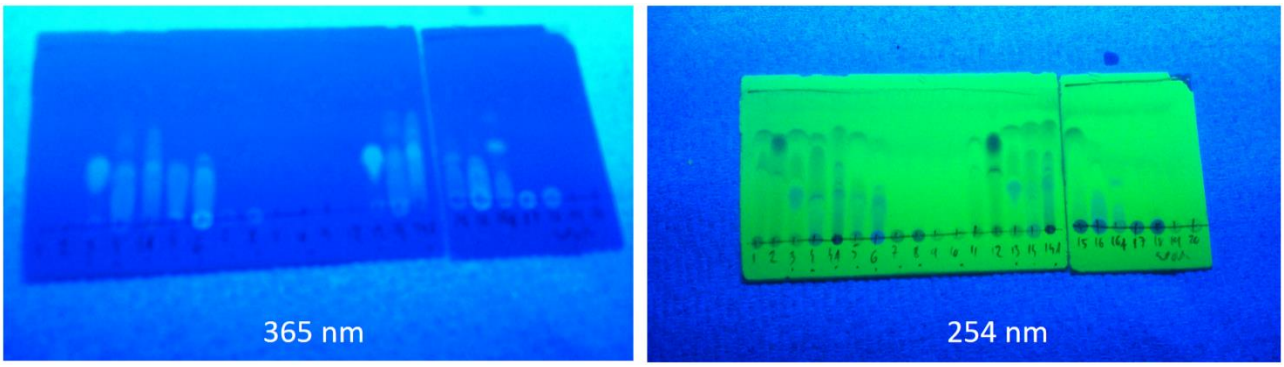

Figure 12.1. TLC (Merck Silica gel 60 F_{254}, eluent: EtOAc/acetic acid 100/1 volume/volume) of crude products described in chapter 3. Photographed under different wavelengths.

1.3. Optical properties

UV-Vis absorption

C-dots typically exhibit broad optical absorption maxima in the UV region (250-350 nm) and a weaker absorption tail in the visible region.[40] The absorption peaks appear at around ~240 nm are due to π-π* transition of C=C bonds, and peaks at ~340-360 nm are due to n-π* transition from C=O bonds of surface functional groups.[41] Surface tailoring can modify the absorption spectra of C-dots and alter their emission spectra too.[42] Doping with heteroatoms also influences the absorption spectra of C-dots due to their alteration in the π-π* energy levels.[43] The surface defects in C-dots are responsible for broad spectral signals in their absorption spectra.[44] Furthermore, carbonyl and amino functionalities promote red shifts of the absorption band maxima in the UV-Vis spectra due to their influence on HOMO-LUMO energy levels of C-dots.[45]

Photoluminescence spectroscopy

C-dots show excellent PL properties. The PL maximum for C-dots usually appears in the blue and green region.[46] PL behavior of C-dots can be tuned by varying the initial precursors and synthetic methods and by surface functionalization.[47] A reported C-dot with an average particle size of 1.5 nm, exhibited PL with maxima at ~460 nm, 540 nm, and 620 nm upon excitations with 380 nm, 460 nm, and 540 nm light, respectively.[48] C-dots derived from *m*-aminobenzoic acid with intense PL at 415 nm were synthesized and used as biosensors for the sensing of Fe^{3+} and pH.[49] C-dots passivated with oligomeric ethylene glycol diamine (PEG1500N) exhibited photoinduced electron transfer (PET) reactions, and its PL was quenched in the presence of various chemicals: Ag^{+}, 2,4-dinitrotoluene, 4-nitrotoluene, and N,N-diethylaniline.[50]

Photoluminescence quantum yield (QY)

QY is a very important parameter for light-emitting systems and defined as the ratio of the number of photons emitted and the number of photons absorbed in the photoluminescence process. High QY can be achieved by surface functionalization on C-dots.[51,52] C-dots obtained from precursors with electron-withdrawing groups like carboxylic and epoxy decrease electron density in C-dots and produce relatively low QY.[53] Surface engineering can convert electron-withdrawing groups to electron-donating groups by chemical conversion without altering the shape of the carbon particles.[54] Doping the C-dots with heteroatoms is another approach that can generate C-dots with high QY by altering the bandgap and electron densities.[55,56]

1.4. Applications of carbon dots

Due to the C-dots simple synthesis methods and its easy surface modification, which allows us to finely tune its properties (e.g. heteroatom content, hydrophilic – hydrophobic transformation, increasing stability/solubility, PL emission bands and intensities), it is widely used in the field of nanoscience.

Detection of Toxic Chemicals

Toxic materials like heavy metal ions,[57] pesticides,[58] antibiotics,[59] and non-biodegradable chemicals over their allowed concentrations may lead to serious health issues. C-dots based sensors working by PL quenching effects are successfully employed for detections of heavy and (highly) poisonous metal ions like Hg^{2+},[57,60] Cr^{6+},[61] Pb^{2+} [62] and Cu^{2+}. [63] The interaction of metal ions and the surface functional groups of C-dots leads to the formation of new electron-hole recombination, and results in the change of the fluorescence nature of the particles.[30] In most of the cases, linear relationships between the quenched PL intensity and the concentration of metal ions have been observed.[64,65] Besides metal ions, anions like F^-,[66] PO_4^{3-},[67] and I^- [68] can be detected by utilizing the C-dots-based sensors.

The present thesis discusses the possibility of using crude C-dots as a nitrite ion (NO_2^-, see chapter 5.2) sensor for aqueous samples, acting through a diazotization/decomposition process, which replaces the surface amino functionalities (as remnants of the precursor *p*-phenylenediamine) to diazonium- then hydroxyl groups, and as a result, fluorescence quenching occurs, which successfully utilized for nitite ion quantification, while the possible interference of naturally occurring metal ions was also explored.

Detection of explosives

Detection and monitoring of explosives have great worldwide attention, concerning national and international security.[69] Picric acid, trinitrotoluene (TNT), and dinitrotoluene (DNT) are common explosives whose presence even in trace amounts may be life threatening.[70] Therefore, the detection of such chemicals is a common task, but the current methods are usually very expensive. Interestingly, C-dots or C-dots-based composites are proved to be useful for their detections. There are reports of C-dots utilized for sensitive detection of explosives with good efficiency at low-cost.[71,72]

Drug delivery, bioimaging and biosensing

C-dots are used in medicinal chemistry for drug delivery, bioimaging and for development of biosensors[11] due to their excellent nontoxic properties. Most of the drug carrier nanomaterials have not shown any PL activities, while C-dots having PL properties, may act as an advanced drug carrier as their emission helps in tracing drugs in healthy and abnormal cells. A C-dot modified with oxaliplatin was used as an efficient cancer drug.[73] The composite C-dots released oxaliplatin within the malignant cells, then, free C-dots assisted to carry out analysis of the cancer cell. A recently synthesized composite of curcumin with ionic liquid-based C-dots showed its efficacy as anticancer drug, exhibiting excellent drug-carrying potential and high cell-penetration power. The composite exhibited 69% drug loading and 88% cell viability on HeLa cells.[74]

In vitro and *in vivo* bioimaging studies are essential tools for clinical purposes in the detection of disease-affected cells. C-dots synthesized from arginine have been successfully utilized *in vitro* cytotoxicity tests on different cells with very high cell viability (above 90%).[75]

Solar energy conversion

Doped C-dots[12] greatly contributed for the development of solar cells by utilizing the C-dots.[76,77] Development of eco-friendly solar cells, free from toxic chemicals is of much importance. A reported N-rich C-dots-perovskite-based composite exhibited better efficiency in comparison with the normal perovskite solar cells.[78] Another unique C-dots based solar cell was operating at very low light intensities, even during the night.[79]

Photocatalysis

C-dots play an important role in photocatalytic water treatment and chemical degradation. In the photocatalytic process, electrons (e^-) of the photocatalyst are excited by light and promoted from the valence band to the conduction band. Simultaneously, the holes (h^+) generated in the valence bond migrate to the surface of photocatalysts, specifically, to the attached C-dots which acting as an acceptor of the photogenerated holes and prevent the electron-hole recombination during the photocatalytic processes.[80]

The electrons at the surface initiate reduction reactions, forming superoxide radicals ($^{\cdot}O_2^-$) with a reductive potential between +0.5 and −1.5 V vs. NHE (normal or standard hydrogen electrode), while the holes initiate oxidation reactions and produce hydroxyl radicals ($^{\cdot}OH$) with an oxidative potential between +1.0 and +3.5 V vs. NHE.[81]

The photoreduction of methylene blue under visible light was reported and the process was catalyzed by C-dots and other nanoparticle-based materials, such as SiO_2/C-dots, TiO_2/C-dots, SiO_2 and TiO_2 nanoparticles. The degradation of methylene blue was observed in the presence of SiO_2/C-dots and TiO_2/C-dots, while SiO_2 and TiO_2 nanoparticles, and the C-dots had no effect on dye degradation. Therefore, C-dots proved their essential role in photodegradation under visible-light (as pure SiO_2 and TiO_2 were found inactive).[31] Upon photoillumination of the TiO_2/C-dots or SiO_2/C-dots photocatalyst, the C-dots absorb visible light, and then emit at shorter wavelengths (325 to 425 nm), which excites TiO_2 or SiO_2 to form electron/hole (e^-/h^+) pairs, which react with the adsorbed oxidants/reducers (usually O_2/OH^-) to produce active oxygen radicals like $\cdot O_2^-$, $\cdot OH$, which finally cause the degradation of methylene blue. Promising photocatalytic activity for Rhodamine B degradation was also achieved by sulfur and nitrogen co-doped C-dots(/TiO_2 composites under excitation at 420–520 nm.[82]

This function of C-dots is discussed in chapter 4.4 in which citric acid based crude C-dots with different characteristic PL excitation-emission wavelengths (chapters 4.1-4.2-4.3) were co-precipitated with TiO_2 and their photocatalytic activities towards Rhodamine B were tested under natural light irradiation.

Our aim was to develop a very simple method to obtain a titania/C-dots photocatalysts by a simple co-precipitation method, in which we make use of various crude C-dots (synthesized as described in chapter 4) exhibiting light absorption in different ranges of UV-Vis light. This approach minimized reaction times and the used solvents were limited to the environmentally friendly water and ethanol. Unfortunately, the approach failed, as advanced photocatalytic effects were not observed, however some conclusions might be learned from the detailed results in chapter 4.4 for possible future modifications.

1.5. Research purpose of the thesis

As the title says we wished to make use of "carbon-based nanostructures in hybrid materials for detection and removal of water pollutants" therefore, as first approach we decided to use the most recent stars of carbonaceous nanomaterials: the carbon dots as our main (later only) group of materials to achieve these goals as C-dots have numerous advantageous properties, most importantly their strong fluorescence, simple preparation and easy modification of their various functionalities on their surface, which are mainly determined by the used synthetic methods and precursors. This variety makes them ideal candidates for sensing their environment through a PL-response and provides easy surface modification for embedding into hybrid matrices.

C-dots can be easily obtained by their bottom up synthesis, which also makes possible to follow the ongoing chemical processes, by comparing optical data with the spectra of the pure molecular precursors. As formation and optical properties of C-dots are still not perfectly understood, therefore we intended to perform a simultaneous study on structure-PL relations to have a better understanding of formation of the fluorescent units, to have a better chance to optimize their properties for our purposes.

Our first goal in chapter 3 was to get handy with the common synthetic methods (hydrothermal, MW-assisted, pyrolysis) and to find the most economical, scalable, green and safe approach. For this, we used the reportedly very efficient citric acid-Tris system, and found that the simple pyrolysis in solvent free reactions can be optimal for our purposes. In parallel, a small study was also conducted on the effect of different precursor ratios on the PL intensities, which also helped us to obtain the strongest PL / mass unit in short reaction times, As this type of reaction yields C-dots belonging to the widely used citric acid family, we decided to use this synthetic approach for various precursors reacting with citric acid (chapter 4). Therefore pyrolysis of pure citric acid (chapter 4.1), citric acid with Tris (chapter 4.2) and citric acid with urea (chapter 4.3) thoroughly investigated. The obtained C-dots' syntheses were also optimized to finally have fluorescent carbon dots emitting around 410 nm, 460 nm and 520 nm. The C-dots were analyzed and used in their crude form, further improving our time- and resource-saving approach. As the C-dots were analyzed by different optical techniques and structure-PL correlations established, we also successfully surface functionalized them with appropriate organosilanes, which makes possible their future applications in silica matrices. Additionally, we observed an increased stability of C-dots and a shift and intensity change in the PL, which result is also useful for tuning C-dots optical properties. Our study revealed the role of several

molecular fluorophores along chapter 4. Most importantly the *trans*-aconitic acid, which may play a key role in most of the blue-emitting (N-doped) citric acid based C-dots.

Application of citric acid based C-dots in photocatalytic experiments were achieved, by co-precipitating them with titania precursors. Even though, these experiments were partially unsuccessful, important conclusions were obtained, for future modification of experimental settings.

Another set of experiments for the synthesis of pPD based C-dots were conducted and the obtained crude products exhibited PL emission in the range of 530-600 nm, depending on the used solvent. With these particles, we extended up to 600 nm our C-dots PL emission covered visible range, giving a way for comparing the effects of C-dots absorbing and emitting in different ranges of the UV-Vis light. As finally these feature of the whole set of C-dots was not explored, the synthesized pPD based nanoparticles were successfully surface functionalized by an organosilan, which similarly to the previous examples, resulted a shift in the PL, providing a method for tuning its optical properties. The application of these amine capped C-dots for nitrite ion sensing in (natural) water samples was successfully demonstrated, as PL quenching through a diazotization / decomposition reaction was observed.

2. Materials and methods

As numerous **chemicals and solvents** were used through the thesis, the relevant ones detailed in groups in the *experimental* part of all chapters, together with the reaction procedures and conditions.

The applied **synthesis methods** are

- microwave (MW) assisted reactions (in household MW oven and in laboratory MW reactor),
- solvothermal reactions (in a stainless steel autoclave equipped with a 50 mL Teflon inlet, which makes possible the application of high reaction temperature and pressure)
- pyrolysis (open-air reactions, the glass-made flasks immersed into a silicone oil bath)

Through the study of syntheses of C-dots, at first we systematically varied the precursor ratios, the synthesis methods, the presence or absence of solvents and the reaction times, while due to an initial technical difficulty, we used only one reaction temperature (180^{o}C), which was finally standardized for most of the experiments. As simple pyrolysis was found the best method for us, therefore, most of our later syntheses used that setting. All reactions carried out under ventilation (in a laboratory fume hood).

Analytical techniques:

Fluorescence spectroscopy (PL) measurements were performed on a Horiba Jovin Yvon Fluoromax-3. Typically, 3D PL maps of aqueous solutions were recorded in the range of 200 nm to 800 nm (for excitation and emission) and relevant data were extracted. The same spectrofluorimeter and identical measurement settings were used in all the cases for simple comparison of the obtained data. Various samples measured at different concentrations, therefore, for easy comparison, the recorded PL intensities were divided by the concentration, to obtain standardized values: count per second (CPS) / (1 mg L^{-1}). Chapters: 3, 4.1, 4.2, 4.3, 4.4, 5.1, 5.2

PL emission spectra were taken in the range of 565-700 nm upon excitation at 550 nm (optimal excitation wavelength for Rh B). All samples were diluted 30x by water, prior to measurements. Chapter 4.4.

Photoluminescence quantum yield (QY) measurements has been performed using the quanta-φ (HORIBA) integrating sphere accessory, attached to the "NanoLog" Horiba Jobin Yvon

spectrofluorometer. Measurements were performed on equal amounts of water and C-dots' aqueous solutions in the same quartz cuvette. Samples excited at 335 nm and emission typically recorded from 300 to 700 nm. Only the most fluorescent samples were analysed. The concentration of C-dots in aqueous solution was typically 100 mgL^{-1}. Chapters 3 and 4.2.

Infrared spectra were collected by a Bruker Vertex 70 spectrophotometer in absorbance mode in the 4000-400 cm^{-1} range, with 256 scans and 4 cm^{-1} resolution, using 2 mg of solid C-dots or pure chemicals to prepare KBr pellets (150 mg). The data were processed with OPUS 7.0 software. Chapters 4.1, 4.2, 4.3, 5.1 and 5.2.

UV-Vis measurements were performed in absorbance mode, using a Nicolet Evolution 300 spectrophotometer from 200 to 800 nm, at 500 $nm \cdot min^{-1}$ scan rate. Each acquisition is the average of three different scans collected with a bandwidth of 1.5 nm. C-dots solutions were typically 50 and 500 or 1000 mg L^{-1} for the analysis. The data were processed with ORIGIN Pro 8 software. Chapters 3, 4.1, 4.2, 4.3, 5.1 and 5.2.

Dynamic light scattering (DLS) measurements were performed in a Horiba LB-550 to obtain the C-dots' hydrodynamic diameter distribution in their aqueous samples. The instrument allows measuring the size of particulates dispersed in solution in a range from 1 nm to 6 μm at the laser wavelength of λ=650 nm. The allowed concentration ranges from ppm up to 40% in solids. The aqueous samples were sonicated for 15 minutes prior to analysis at 25 °C. Chapters 3 and 4.2.

SDT Q600 (TA Instruments) was used for thermal analysis. It provides simultaneous measurements of weight change (TGA) and true differential heat flow (DSC) on the same sample from ambient temperature to 1500°C. ~10 mg of samples were analysed in constant nitrogen flow and fast heating rate (20°C/min) up to 180°C; thereafter the temperature was kept constant to monitor the samples' thermal response. The solids were well powdered in a mortar prior to measurements. Chapters 4.1, 4.2 and 4.3.

In cooperation: Elemental analysis (EA) was performed on the dry samples by a PerkinElmer 2400 Series II CHNS analyzer. Chapter 4.1.

In cooperation: Raman spectra were collected using a Senterra Raman microscope (Bruker Optics, Inc.), irradiating the samples deposited on Si substrates, at the excitation wavelength of 785 nm. The spectra resolution was < 5 cm^{-1}. Chapter 4.2.

In cooperation: Time Resolved Photoluminescence (TR-PL) spectra in the picosecond–nanosecond time range were collected by exciting the samples with the 1 kHz ps third harmonic emission of a Nd:YAG laser (355 nm Spectra Physics) whose pulse width was less than 300 ps. The PL signal was detected with a streak camera (Hamamatsu C5680) coupled with an Arc-Spectra-Pro 275 monochromator (cumulative time response lower than 500 ps, spectral resolution 1 nm). All the PL measurements were gathered by exciting the samples in the front face mode to avoid reabsorption effects. Proper optical filters were applied when needed. Chapter 4.1.

In cooperation: Time-resolved Photoluminescence (TR-PL) spectra were gathered by using wavelength-tunable 100-fs-long pulses, delivered by an optical parametric amplifier (TOPAS-800-fs-UV-1) pumped by a Ti:sapphire amplified laser with 1 kHz repetition rate (Coherent Libra-F-1K-HE-230, output energy larger than 4mJ/pulse). The optical emission was dispersed by a spectrometer (ARC-SpectraPro 2300i, 50 g/mm grating, 600 nm blaze) coupled to a streak camera (Hamamatsu C10910-01). The typical operative system time response was shorter than 50 ps, the spectral resolution was 1 nm. Chapter 4.2.

In cooperation: Liquid chromatography / mass spectroscopy (LC/MS) was performed by dissolving the samples in LC-MS grade water and diluted to a final concentration of 10 mg L^{-1}. The analysis was performed by using a Thermo Fisher Scientific UltiMate 3000 SD UHPLC coupled to a Q-Exactive Plus system equipped with a heated electrospray ionization HESI-II source. Mass calibration was done prior to analysis according to the manufacturer's recommendations using external mass calibration. Gradient reversed phase elution was performed on a Phenomenex Luna C18 column (50 mm × 2.1 mm, 1.6 µm). The mobile phases for gradient elution were water with formic acid (0.1%, v/v eluent A) and acetonitrile with formic acid (0.1%, v/v eluent B). The flow rate was set to 300 µL min^{-1} using the following gradient: 0–5.0 min 100% A, 5–8 min to 100% B, 8–10 min hold 100% B, 10–12 min to 100% A, 12–13 min hold 100% A. The column temperature was 35 °C. The injection volume was 5 µL. The HESI-II source conditions for every experiment were: ionization mode negative; sheath gas, 20 AU; auxiliary gas, 5 AU; sweep gas, 0 AU; spray voltage, 2.80 kV; heater temperature, 320 °C; ion transfer capillary temperature, 320 °C; and S-lens RF level, 60.0.; ionization mode positive: sheath gas, 50 AU; auxiliary gas, 13 AU; sweep gas, 3 AU; spray voltage, 3.50 kV; heater temperature, 320 °C; ion transfer capillary temperature, 320 °C; and S-lens

RF level, 60.0. The settings for alternate full scans data acquisition were: resolution, 70,000 fwhm; microscans, 2; automatic gain control (AGC) target, 1×10^6; maximum injection time, 100 ms; scan ranges, *m/z* 50–750 negative and positive and 400-6000 negative and positive. The analysis was performed using a sequence of three injections of pure water for apparatus equilibration, followed by three injections of each sample. The data were elaborated with Thermo Fisher Xcalibur software version 3.1.66.10, extracting the current for each ion in a ±0.01 m/z range. Chapter 4.1.

In cooperation: Transmission electron microscopy (TEM) images were obtained by using a FEI TECNAI 200 microscope working with a field emission electron gun operating at 200 kV. Sample preparation was done by dispersing the nanoparticles in ethanol by ultrasonication and then dropping them onto a carbon-coated copper grid and drying them for observations. The C-dots size distribution was calculated from TEM images by using ImageJ programme. Chapter 4.1.

In cooperation: TEM images were obtained with a JEM 2010 UHR instrument equipped with a Gatan Imaging Filter (GIF) with a 15 eV window and a 794 slow scan CCD camera. At first C-dots were dispersed in n-octane, then a droplet of the solution was cast on a carbon-coated copper grid and let drying before measurement. C-dots size were calculated from 5 TEM images at x 15000 magnification, using an automated routine working on ImageJ programme.[83] Chapter 4.2.

The product were typically analysed in their crude forms.

3. Comparison of bottom-up synthesis methods

3.1. Introduction

Citric acid (CA) and 2-amino-2-(hydroxymethyl)propane-1,3-diol (Tris, **figure 3.1**) can produce highly fluorescent carbon dots (C-dots) in just 5 minutes by using only a domestic microwave oven.[17] The reaction is very easy to reproduce, but after a few preliminary experiments, the uncontrolled reaction temperature, the supposedly inhomogeneous irradiation and the release of possible flammable and poisonous vapors in our household microwave oven discouraged us to use this method, while the enchantingly intense fluorescence of the desired product called for further analysis.

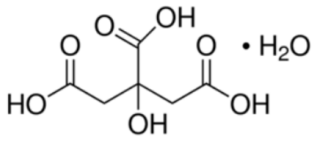

Citric acid monohydrate (CAM),
2-hydroxypropane-1,2,3-tricarboxylic acid;hydrate
CAS: 5949-29-1
M_r: 210.14
mp: 135°C
decompose: >175°C

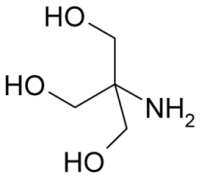

Tris(hydroxymethyl)aminomethane (Tris),
2-Amino-2-(hydroxymethyl)propane-1,3-diol
CAS: 77-86-1
M_r: 121.13
mp: 167-172°C

Figure 3.1. Structure and properties of citric acid monohydrate and Tris

In this chapter we focus on the comparison of common bottom-up synthesis methods to find a convenient, fast and simple approach to obtain strongly fluorescent C-dots, by using the CA/Tris system as a model. Further analysis of the optimized processes are detailed in chapters 4.1 and 4.2. A series of reactions were set to examine the effects on fluorescence intensity by applying different synthetic methods (such as open-air pyrolysis, reaction in a laboratory microwave reactor and in a hydrothermal reactor, **figure 3.2**) and by varying the precursor ratios from pure citric acid to pure Tris. Fluorescence quantum yields (QY), UV-Vis absorbance and hydrodynamic diameters by DLS analysis were also measured for selected samples.

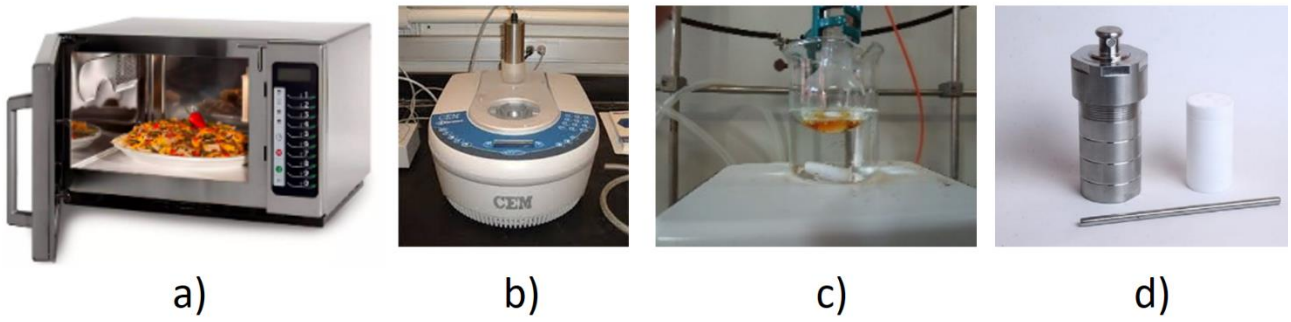

Figure 3.2. Applied equipments for C-dots synthesis: household MW oven (a), laboratory MW reactor (b), flask in oil bath (c) and hydrothermal reactor (d).

3.2. Experimental

Typically, five ratios (1:0, 3:1, 1:1, 1:3, 0:1) of citric acid and Tris were investigated by varying five synthesis methods and the reaction time. Only the best two sets of parameters were used for a hydrothermal synthesis for an extended reaction time (without MW irradiation) due to the observed ineffective (slow) reaction course. Temperature was standardized at 180°C (except in the case of using the household microwave oven, where temperature was not monitored). Stirring was not applied during the hydrothermal and household MW-reactions, while moderate agitation was possible in the case of neat reactions and in the laboratory MW reactor. Due to the observed bubbling and fuming during the reactions, all experiments were carried out under appropriate ventilation.

Chemicals and Reagents

Citric acid monohydrate (CAM)	Fluka, >99.5%
2-amino-2-(hydroxymethyl)propane-1,3-diol (Tris)	Carlo Erba, >99.5%

In-site produced Milli-Q water was used for the analysis.

All chemicals were utilized without further purification.

None of the precursors showed observable fluorescence under our measurement conditions.

Synthesis methods

Microwave assisted reactions (MW methods)

"MW-A" method – household MW oven – open vessel

A few attempts were made to reproduce (as close as we were able) the earlier reported[17] best reaction conditions. 350 mg (1.67 mmol) citric acid monohydrate and 202 mg Tris (1.67 mmol) - 1:1 molar ratio - were dissolved in 2 ml of water in a 20 mL beaker while sonicated). During the course of the reaction, the observed wild boiling/bumping controlled our heating program in the reported 5 minutes. A power **on**-off pattern in seconds: **45**-5-**35**-5-**30**-10-**15**-10-**20**-10-**25**-10-**35**-10-**35** was applied in a household MW oven (DPE srl, Italy, "Marte" type, 2450 MHz at medium level which applies 480W power (instead of the reported 350W). Colorless dense liquids were obtained. The synthesis was repeated by using 350 mg (1.67 mmol) citric acid monohydrate and 67 mg Tris (0.56 mmol) – 3:1 molar ratio.

"MW-B" method – laboratory MW reactor – closed vessel

MW irradiation experiments were carried out in a CEM-Discover MW reactor, using the standard configuration as delivered. The experiments were executed in 10 mL MW process vials with control of the temperature by infrared detection. Typically, 1 mmol starting material(s) were dissolved in 1 mL of water, heated to 175±5^{o}C (our reactor operation limit due to a pressure safety limit) in 5 minutes and kept at that temperature for another 15 or 30 minutes and finally cooled to ca. 50^{o}C in a matter of minutes. (Longer reaction times were applied because of the less intense irradiation compared to MW-A method). Power limit was set to 300W and pressure safety limit to 200 psi. Stirring at medium intensity was applied, and finally, the solvent was evaporated and the obtained colourless or yellowish oils were dried in vacuum until constant weight.

Reactions in oil baths (oil methods)

"Oil-C" method, starting from solution

1 mmol of reactant(s) **(table 3.2)** were placed in a 10 mL MW process vials and dissolved in 1 mL of water and immersed into a preheated 180^{o}C oil bath (100 rpm stirring rate). 15 or 30 minutes reaction times were measured after evaporation of the solvent (typically took less than 5 minutes). Colourless or yellowish oils were obtained and some of them showed signs of crystallization in a matter of weeks by storing at room temperature.

"Oil-D" method, neat reactions

1 mmol of reactant(s) **(table 3.2)** were placed in a 25 or 50 mL round bottomed flask in their crystalline form and immersed into a preheated 180°C oil bath (100 rpm stirring was applied with a Teflon coated stirring bar). Reaction times were measured from the moment of complete melting of crystals. Since the obtained molten liquid cannot homogenize without agitation, so a moderate stirring (100 rpm) was applied. (The other methods used aqueous solutions at the start point, which guaranteed the homogeneity even after evaporation of the solvent.)

Hydrothermal reactions (HT method, closed vessel)

Only the most promising citric acid:Tris 3:1 and 1:1 molar ratios were tested and monitored for several hours since short reaction times cannot be applied in such big equipment. Only the warming up and cooling down need tens of minutes, so instead of our typical 15 and 30 minutes, in this case 1, 3, 5 and 7 hours long reactions were examined.

A stainless steel reactor equipped with a 50 mL PTFE inlet was used for the reaction. 1.575 g citric acid monohydrate (7.50 mmol) and 0.303 g Tris (2.50 mmol) or 1.050 g citric acid monohydrate (5.0 mmol) and 0.606 g Tris (5.0 mmol) were dissolved in 10 mL water and the sealed hydrothermal reactor was placed in a preheated oven (120-130°C). The temperature was increased gradually to 180°C (temperature of the oven) in 30 minutes. Reaction time was measured from the instance of reaching 180°C until the removal from the oven (even though natural cooling to room temperature typically took place in hours).

All of the products appeared as colourless or yellowish oils after evaporation of the solvent (if there was any). In case of simple pyrolysis (oil-D method), as a sign of more advanced carbonization, in the lack of initial solvent, even a light brown colorization was observed.

3.3. Results and discussion

Method MW-A is the starting point of our experiments and it is a close reproduction of the reported work,[17] which resulted, in overall, only weakly fluorescent products (with high QY>90%, **figure 3.3, table 3.1**) and homogenous particle size distribution (**figure 3.4**), while another set of reactions from **methods HT, MW-B, Oil-C and D** gave us a clearer picture of the role of synthesis approaches in increased PL intensities.

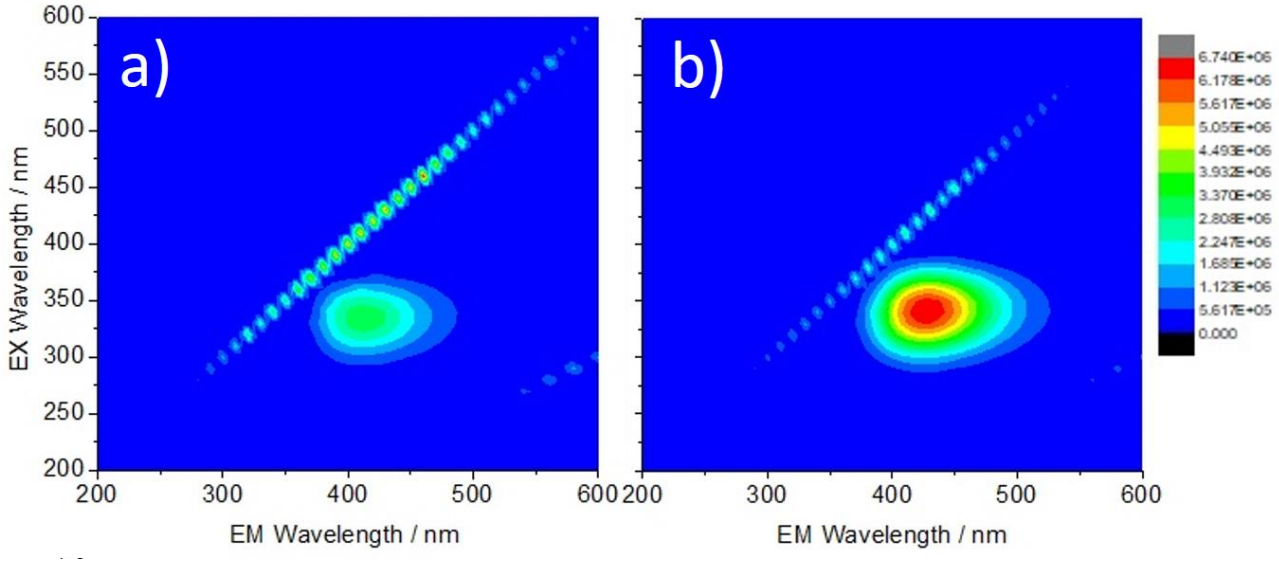

Figure 3.3: 3D emission (x-axis)-excitation (y-axis)-intensity spectra (false color scaling) of the crude product obtained from citric acid:Tris 1:1 (n/n) (a) and 3:1 (b) by the use of a household MW-oven **(MW-A method)**. Samples measured at 1000 mg/L in water.

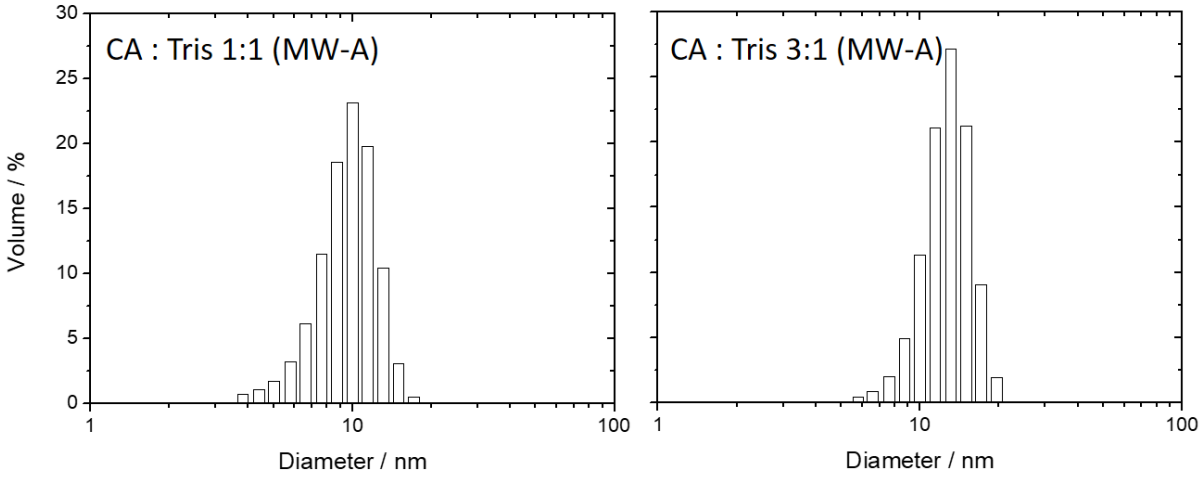

Figure 3.4. DLS results show the hydrodynamic size distribution of aqueous samples obtained by the MW-A method (household MW oven for 5 minutes) at the precursor rates of 1:1 (a) and 3:1 (b).

Citric acid:Tris (n:n)	Heating method, reaction temperature and reaction time	Max. excitation / Max. emission (nm) (concentration of the measured samples)	Maximum standardized PL-intensity, CPS/(mg/L)	Mean hydrodinamic diameter, nm	Quantum yield
1:1	MW-A, unknown, 5 min	340/415 (1000mg/L)	2,300	9.1	95
3:1	MW-A, unknown, 5 min	340/425 (1000mg/L)	6,739	11.9	91

Table 3.1. Properties of the crude products obtained by the use of a household MW-oven (MW-A method) for 5 minutes by using citric acid:Tris 1:1 and 3:1 molar ratios. (Maximum excitation/emission wavelengths, standardized maximum PL intensities, DLS and quantum yields results)

Pure citric acid, pure Tris and their different mixtures were reacted under defined conditions and their PL properties were measured and summarised in **table 3.2.** Reacting the mixture of citric acid:Tris at 1:0 (only citric acid), 3:1, 1:1, 1:3 and 0:1 (only Tris) molar ratios showed that 1:1 and especially 3:1 ratios gave the most promising results, with a 500-5000 times more intense emission that any pure component can provide in this experiment setting. The obtained data also reveal the superiority of **methods oil C and D** for simple and fast synthesis of C-dots with strong fluorescence. Even though the QYs are lower, the overall PL is much stronger in the "oil methods", indicating a faster formation (and possibly simultaneous degradation) of fluorescent species.

Compo-sition	Heating method, reaction temperature and reaction time	Max. excitation / Max. emission (nm) (concentration of the measured samples)	Maximum standardized PL-intensity, CPS/(mg/L)	Mean hydrodinamic diameter, nm	Quantum yield
Citric acid	MW-B, 180°C, 15 min	330/430 (100mg/L)	184	7.8	
	oil-C, 180°C, 15 min	340/430 (100mg/L)	2,370	8.5	
	oil-D, 180°C, 15 min	340/430 (200mg/L)	623	6.1	
	MW-B, 180°C, 30 min	340/430 (100mg/L)	1,124	9.8	
	oil-C, 180°C, 30 min	330/445 (100mg/L)	2,218	8.7	
	oil-D, 180°C, 30 min	360/445 (200mg/L)	1,204	8.9	
Citric acid : Tris 3:1 (n:n)	MW-B, 180°C, 15 min	330/410 (1 mg/L)	2,489,000	6.4	87
	oil-C, 180°C, 15 min	340/410 (1mg/L)	9,140,000	9.1	59
	oil-D, 180°C, 15 min	340/410 (1mg/L)	10,090,000	10.2	66
	MW-B, 180°C, 30 min	330/410 (1mg/L)	3,283,000	10.8	81
	oil-C, 180°C, 30 min	340/410 (1mg/L)	11,264,000	10.7	62
	oil-D, 180°C, 30 min	340/410 (1mg/L)	7,688,000	6.5	38
Citric acid : Tris 1:1 (n:n)	MW-B, 180°C, 15 min	330/405 (1mg/L)	3,223,000	8.5	86
	oil-C, 180°C, 15 min	340/410 (1mg/L)	7,061,000	10.2	87
	oil-D, 180°C, 15 min	340/410 (1mg/L)	10,744,000	8.6	66
	MW-B, 180°C, 30 min	330/410 (1mg/L)	7,962,000	7.8	72
	oil-C, 180°C, 30 min	340/420 (1mg/L)	9,975,000	8.9	75
	oil-D, 180°C, 30 min	Solubility less than 1 mg/L	no data	-	-
Citric acid:Tris 1:3 (n:n)	MW-B, 180°C, 15 min	330/410 (10mg/L)	260,000	12.1	
	oil-C, 180°C, 15 min	340/415 (10mg/L)	397,000	7.9	
	oil-D, 180°C, 15 min	330/410 (10mg/L)	591,000	8.8	
	MW-B, 180°C, 30 min	340/415 (10mg/L)	744,000	9.4	
	oil-C, 180°C, 30 min	340/415 (10mg/L)	572,000	8.8	
	oil-D, 180°C, 30 min	340/410 (10mg/L)	746,000	7.4	
Tris	MW-B, 180°C, 15 min	330/405 (100mg/L)	10,103	9.7	
	oil-C, 180°C, 15 min	340/410 (100mg/L)	1,445	9.3	
	oil-D, 180°C, 15 min	340/420 (100mg/L)	1,444	8.3	
	MW-B, 180°C, 30 min	330/410 (100mg/L)	6,823	8.2	
	oil-C, 180°C, 30 min	330/415 (100mg/L)	471	7.7	
	oil-D, 180°C, 30 min	340/420 (100mg/L)	18,519	10.0	

Table 3.2. 1 mmol of citric acid, Tris or their different mixtures (total quantity: 1 mmol, molar ratios indicated) were reacted under the above detailed conditions 3D PL spectra of all products were taken and maximum excitation/maximum emission pairs with the concentration of the analysed aqueous solutions were recorded. All DLS and some quantum yield results are also listed.

For further analysis, 3:1 and 1:1 molar ratios of citric acid and Tris were reacted in (the commonly used) hydrothermal reactor[84-86] **(HT method)**. As a consequence of the weight and volume (50 mL) of our reactor, only slow heating and cooling processes were applied. It must be also noted, that such synthetic method usually requires several hours[87] to obtain satisfactory fluorescence properties, therefore we analysed the crude products only after 1-3-5-7 h reaction times (**table 3.3**).

Composition	Heating method, reaction temperature and reaction time	Max. excitation / Max. emission (nm) (concentration of the measured samples)	Maximum standardized PL-intensity, CPS/(mg/L)	Mean hydrodinamic diameter, nm	Quantum yield
Citric acid : Tris 3:1	HT, 180°C, 1h	330/420 (100mg/L)	1,004		
	HT, 180°C, 3h	330/410 (10mg/L)	202,100	8.4	86
	HT, 180°C, 5h	340/410 (10mg/L)	324,800		
	HT, 180°C, 7h	330/405 (10mg/L)	408,800	9.2	91
Citric acid : Tris 1:1	HT, 180°C, 1h	340/415 (100mg/L)	54,060		
	HT, 180°C, 3h	340/410 (10mg/L)	129,600	10.0	98
	HT, 180°C, 5h	330/410 (10mg/L)	165,700		
	HT, 180°C, 7h	340/420 (10mg/L)	203,100	9.9	99

Table 3.3. PL properties of the crude products obtained by the hydrothermal reaction of 7.5 mmol citric acid and 2.5 mmol Tris or 5 mmol citric acid and 5 mmol Tris at 180°C for the indicated reaction time.

All of the different synthetic methods represented by their most fluorescent product in this study summarized in **figure 3.5a** (reported by their standardized PL intensities). The diagram clearly shows the inefficiency of the household-MW and hydrothermal methods (at least in our case), while simple pyrolysis in open vessels shows superior PL-properties. Additionally, it is also clear that reacting citric acid : Tris mixtures in the ratio of 3:1 and 1:1 yield the most fluorescent products (**figure 3.5b**). Since the water solubility of the product from the 3:1 mixture turned out to be better, therefore this precursor ratio (chapter 4.2) and the **oil-D** method (chapters 4.1 - 4.2 - 4.3) were selected for further studies.

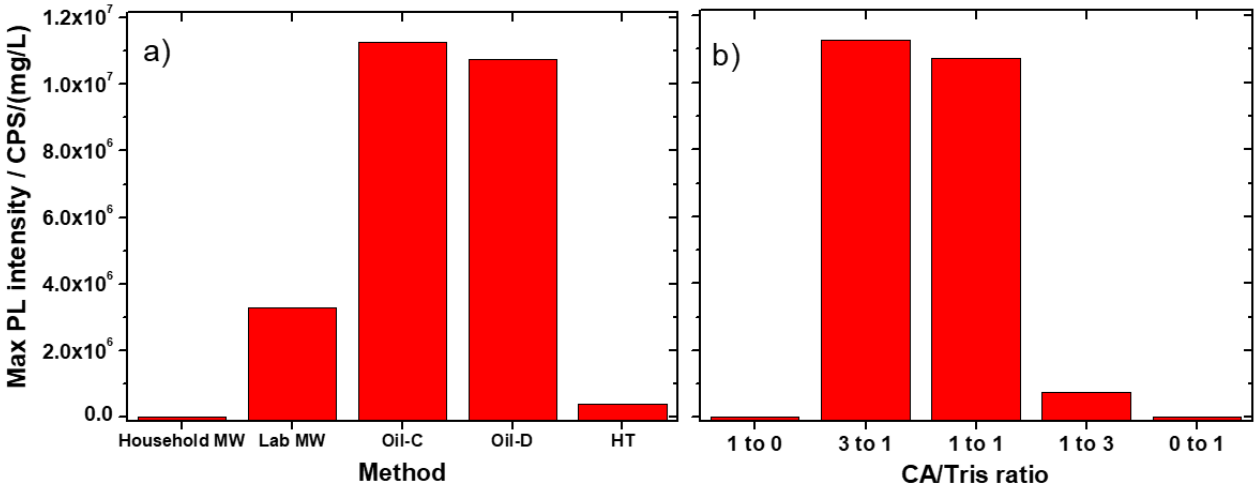

Figure 3.5. Comparison of synthesis methods (household MW-oven, laboratory MW-reactor, Oil-C: pyrolysis starting from solution, oil-D: pyrolysis starting from crystalline solids and HT: hydrothermal reaction) by their products' most intense PL emission in this study (regardless of composition or reaction time) (a) and comparison of different starting citric acid/Tris ratios by their products with the most intense PL emission (regardless of synthesis method or reaction time) (b).

The PL emission of the synthesized C-dots are typically in the range of 405-420 nm (violet light) for all the Tris containing samples, while >430 nm in the case of using only citric acid as precursor, which indicates different fluorophores in these crude C-dots. The phenomena is further studied in chapters 4.1 and 4.2.

Analysis of the QY results (**tables 3.1-3.2-3.3**) also reveal, that synthesis methods using (an initial) solvent, usually results higher light absorption-emission efficiency (QY), but simultaneously a weaker overall PL. This can be explained by the difference in the samples' carbonization degree. An additional solvent seemingly slows the reaction process and also preserve more intact fluorophores during the formation of C-dots. These probably still molecule-like PL sources have higher QYs, while the advanced carbonization process in the solvent free (**oil-D**) method gives way for faster reactions through condensation and decarboxylation steps (detailed in chapters 4.1 and 4.2) alongside with possible decomposition of such fluorescent structures, to finally give a lower average QY and at the same time a higher overall PL intensity. By selecting the CA:Tris 3:1 based samples with the highest QY (**HT**, 7h, QY: 91%) and the one with highest overall PL intensity (**Oil-C**, 30 min, QY: 62%) and plotting their UV-Vis spectra (**figure 3.6**), we can see that **HT method** (as the reaction carried out in water) yields a product with minimal absorbance at 340 nm, compared to the one obtained by the **Oil-C** method, where the initial solvent eliminates at the beginning of the reaction.

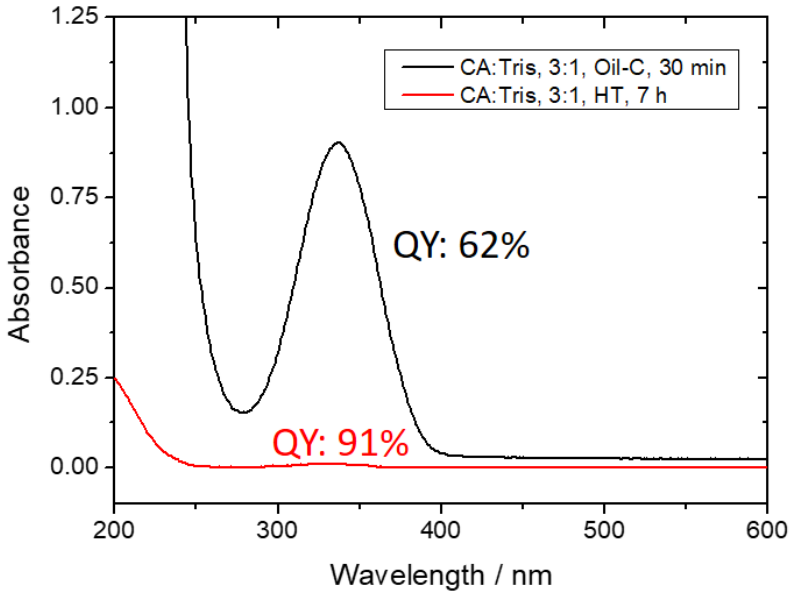

Figure 3.6. UV-Vis absorbance spectrum of CA:Tris 3:1 based product synthesized by HT method for 7 h, exhibiting very high QY (91%) and low absorbance at 340 nm, (red line), and the UV-Vis spectrum of the product obtained by the Oil-C method in 30 minutes exhibiting intense absorbance at 340 nm, and only lower, 62% overall QY (black line). The samples measured at 100 mg/L (aq) concentration.

The mean hydrodynamic diameter values obtained by DLS measurements (**figure 3.4** and **tables 3.1 – 3.2 – 3.3**) vary between 6 and 12 nm and no trends in aspects of reaction times, methods or precursor ratios were observed. However these results are well in accordance to the reported data.[17]

3.4. Conclusions

A thorough investigation of the effects of different C-dots synthesis methods, precursor ratios and reaction times on the mixtures of citric acid and Tris was conducted and the results analyzed to find the most convenient method for obtaining highly fluorescent C-dots in short reaction times. The results clearly show that using the citric acid-Tris model system, the most efficient method is the simple pyrolysis of the precursors. This approach can be considered “green” not just for the elimination of any solvents from the synthesis, but for the shorter reaction times too. By applying the same reaction temperature through the tested methods, pyrolysis turned out to be the fastest, which

can greatly reduce the consumed energy during the synthesis. The obtained products, in an optimal case, can be easily dissolved in water and analyzed or stored for later applications.

While description of different methods for synthesis of C-dots, usually with numerous non-relating examples, are often reported in literature, but at the same time, testing of the same model system by various (bottom-up) synthetic approaches, can hardly be found. Therefore, this chapter can be considered as a unique attempt to reveal the chemical behavior of molecular precursors building up fluorescent units in common bottom-up synthesis methods. On the other hand, optimization of precursors and reaction conditions within one synthetic approach (e.g. only hydrothermal or only MW-assisted) is more popular and it was also part of this experimental setup as the series of experiments also revealed, that citric acid and Tris, reacting in optimal ratios (1:1 or 3:1) can give very intense photoluminescence, possibly even thousands of times stronger, than precursors alone.

The findings of this chapter encouraged us to use the simple pyrolysis method for most of our experiments and to further study the roles of the precursors in the formation of C-dots and their contribution in the achieved PL. Therefore, we thoroughly investigated C-dots syntheses in the citric acid family (chapter 4), staring with the simplest system, by the pyrolysis of citric acid (chapter 4.1) and followed by a more extended study on the citric acid-Tris system in chapter 4.2.

4. Syntheses and applications of citric acid based carbon dots

4.1. Citric acid based carbon dots

The results and discussion in this chapter were summarized and published in the following article[88] :

Ludmerczki R, Mura S, Carbonaro C.M, Mandity I.M, Carraro M, Senes N, Garroni S, Granozzi G, Calvillo L, Marras S, Malfatti L, Innocenzi P,
Carbon Dots from Citric Acid and its Intermediates Formed by Thermal Decomposition,
Chemistry - A European Journal, **2019**, 25, 11963-11974
DOI: 10.1002/chem.201902497
Its various contents are reproduced here with permission of the publisher: John Wiley & Sons, Inc.

4.1.1. Introduction

Citric acid (CA) is a common organic acid (**figure 41.1**) and it is largely employed as a low cost precursor, alone[89,90] or in combination with other compounds,[91,92] to produce fluorescent carbon dots (C-dots). C-dots synthesized from CA typically exhibit a blue luminescence in low intensity in comparison to C-dots prepared from other precursors (chapter 4.2 and 4.3).[93-95] However, CA C-dots and other citrate-based fluorescent materials have intrinsic advantages, which are their low toxicity and good biocompatibility. They have been, therefore, widely used for developing fluorophores for biomedical applications.[96-99]

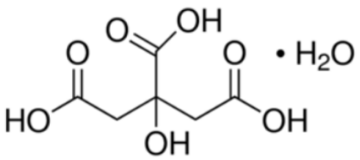

Citric acid monohydrate (CAM),
2-hydroxypropane-1,2,3-tricarboxylic acid;hydrate
CAS: 5949-29-1
M_r: 210.14
mp: 135°C
decompose: >175°C

Figure 41.1. Structure and properties of citric acid monohydrate

The simplest route to synthesize fluorescent C-dots from citric acid is thermal decomposition. In the process, it is dehydrated and partially decomposed in the 180-200°C temperature range to obtain fluorescent materials. The preparation of C-dots from citric acid (CA) is, however, very sensitive to the synthesis conditions, such as reaction temperature, time of thermal treatment[100] and type of solvent. A study on thermal decomposition of CA has proved that several intermediates may be formed during the process.[101] Thermal decomposition, in this case, includes dehydration and decarboxylation to form methyl-maleic acid; during the process other intermediates are formed as products of dehydration, in particular the *cis* and *trans* forms of the aconitic acid (AA) (*trans* prop-1-ene-1,2,3-tricarboxylic acid). Decomposition of CA follows a complex reaction pathway because the intermediates, such as the *cis* and *trans* forms of AA, show different thermal stability.[101]

Understanding and controlling thermal decomposition of CA is, therefore, a hard task, especially if the process is used for obtaining fluorescent C-dots.[102] Some articles have been dedicated to this subject, but the degree of the thermal decomposition as a function of fluorescence response not have been yet completely explained. In particular, the correlation between emission properties and the formation of intermediates during the thermal decomposition has been overlooked because a connection between structure and fluorescence is difficult to reveal. We have mainly used FTIR method to analyze the structural changes during the thermal decomposition. This method has been very effective, in combination with the measure of the optical properties, to understand the complex reaction paths behind a very simple bottom-up route to prepare fluorescent C-dots. Some of the intermediates may be also considered as potential precursors for the synthesis of fluorescent C-dots, however, emissive products and the different routes need to be understood and studied in detail.

Control of the C-dots' optical stability by the design of the surface state is another problematic task and it requires to link the emission properties with the C-dots structure and surface.[103] The surface functionalization of the citrate-based C-dots with organosilanes, to stabilize their optical properties and to effectively incorporate into sol-gel processed hybrid materials is therefore a very important issue.[104-106] The optical properties of C-dots can be modified by functionalization with organosilanes, but a precise correlation is still far from understood.

Therefore we thoroughly studied the changes in optical response during the thermal decomposition of CA and the product has been modified with an organosilane bearing an aminopropyl group, which has been proved to be an effective way to enhance the stability of C-dots.

The goal of the present work is to get a better insight to the chemical processes, which lead to the formation of C-dots starting from CA.

4.1.2. Experimental

Chemicals and Reagents

citric acid monohydrate (CAM)	Fluka, >99.5%
anhydrous citric acid (ACA)	Alfa Aesar, >99.5%
trans-aconitic acid (AA)	Alfa Aesar, 98%
itaconic acid	Alfa Aesar, 99%
itaconic anhydride	Alfa Aesar, 97%
citraconic acid	Alfa Aesar, >98%
citraconic anhydride	Aldrich, 98%
3-(aminopropyl)triethoxysilane (APTES)	Aldrich, 99%
FTIR grade potassium bromide	Aldrich >99%

All chemicals were utilized without further purification.

In-site produced Milli-Q water was used for the analysis.

Only the *trans*-aconitic acid showed observable fluorescence under our measurement conditions.

Synthesis of C-dots from CAM

4200 mg (20 mmol) citric acid monohydrate was placed in a 50 mL round bottomed flask and immersed into a preheated 180°C oil bath. (Magnetic stirring at 100 rpm was applied.) Samples were taken in every 15 minutes from the moment the citric acid completely melted (2-3 minutes) up to 120 minutes of reaction time. The colourless liquid turned to light yellow then orange-yellow and red at the end of the reaction (**figure 41.2**). All the taken samples were dense sticky liquids (and later solidified at room temperature in one week).

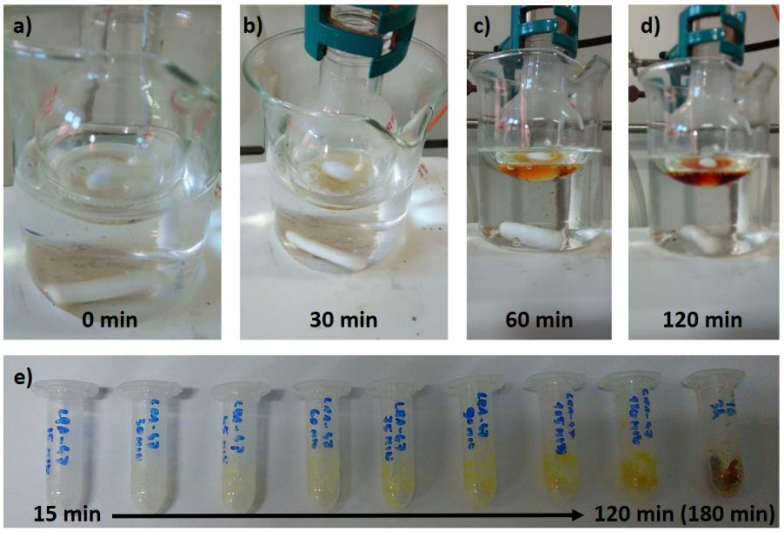

Figure 41.2. Colour change of molten citric acid (a-d) at 180°C at different reaction times and the solidified products (e).

Synthesis of C-dots from citric acid derivatives

In a typical procedure, 1.0 g of *trans*-aconitic acid or itaconic acid or itaconic anhydride or citraconic acid or citraconic anhydride was placed in a 25 mL round bottomed flask and immersed into a 180ºC oil bath (100 rpm stirring rate) for 120 minutes. In the case of *trans*-aconitic acid, 200ºC oil bath was used in the first 15 minutes to exceed its melting point (190ºC) and then the bath temperature was reduced to 180ºC.

Functionalization of C-dots with APTES

The CAM-based C-dots (from the 120 min reaction) were functionalized with APTES. 0.33 mL APTES was added to 10 mL aqueous solutions with a concentration of 1 mg mL^{-1} of the C-dots.[107] The solution was left to stir at 25°C for 24 h at 500 rpm in a sealed vessel. The pH of the C-dots solutions changed from acidic (pH 4.5) to basic (pH 11) after the addition of APTES.

4.1.3. Results and discussion

Citric acid monohydrate (CAM) has been used as precursor to prepare fluorescent C-dots. It has been reacted under stirring in an open vessel, using for heating a silicon oil bath at a temperature of 180°C. Samples to monitor the progress of the thermal decomposition reactions have been taken at different times, from 15 up to 120 min.

Citric acid monohydrate and anhydrous citric acid (ACA) FTIR absorption spectra, in the range 1900-1600 cm^{-1}, are shown in **figure 41.3**. The infrared spectrum of the molecule, in this wavenumber range, is characterized by an overlapped triplet of sharp and intense absorption bands assigned to the vibration of the three carboxylic groups, stretching mode of C=O, in citric acid which are detected at 1759, 1727 and 1688 cm^{-1} (**Figure 41.3a**). [108] On turn, the three C=O stretching bands of anhydrous citric acid (ACA), 1754, 1744 (band overlapped to that one at 1754) and 1703 cm^{-1}, show a different relative intensity and a shift with respect to CAM (**figure 41.3b**).

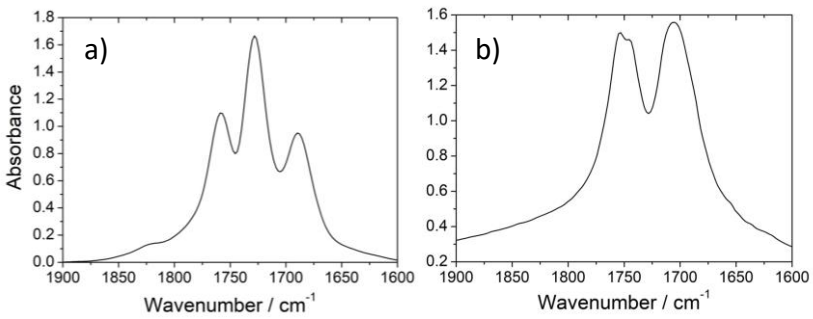

Figure 41.3. FTIR absorption spectra (1900 – 1600 cm^{-1}) of citric acid monohydrate (a) and anhydrous citric acid (b).

The FTIR absorption spectra of the samples upon different reaction times are shown in **figure 41.4** (1900–1600 cm^{-1}). After the first 15 min of reaction, different bands are detected in the C=O stretching region, at 1752, 1744 (shoulder), 1715 cm^{-1} and 1701 (shoulder) while a new absorption band of weak intensity is observed at 1622 cm^{-1} and assigned to the C=C stretching mode. The presence of this band, which is not observed in the precursor (**figure 41.3**), indicates the formation of an intermediate during the dehydration of CAM. This intermediate is itaconic acid (one of the pyrocitric acids) and the attribution has been done comparing all expected compounds and their FTIR signature in this infrared region [96] (**figure 41.5**), (**scheme 41.1**).

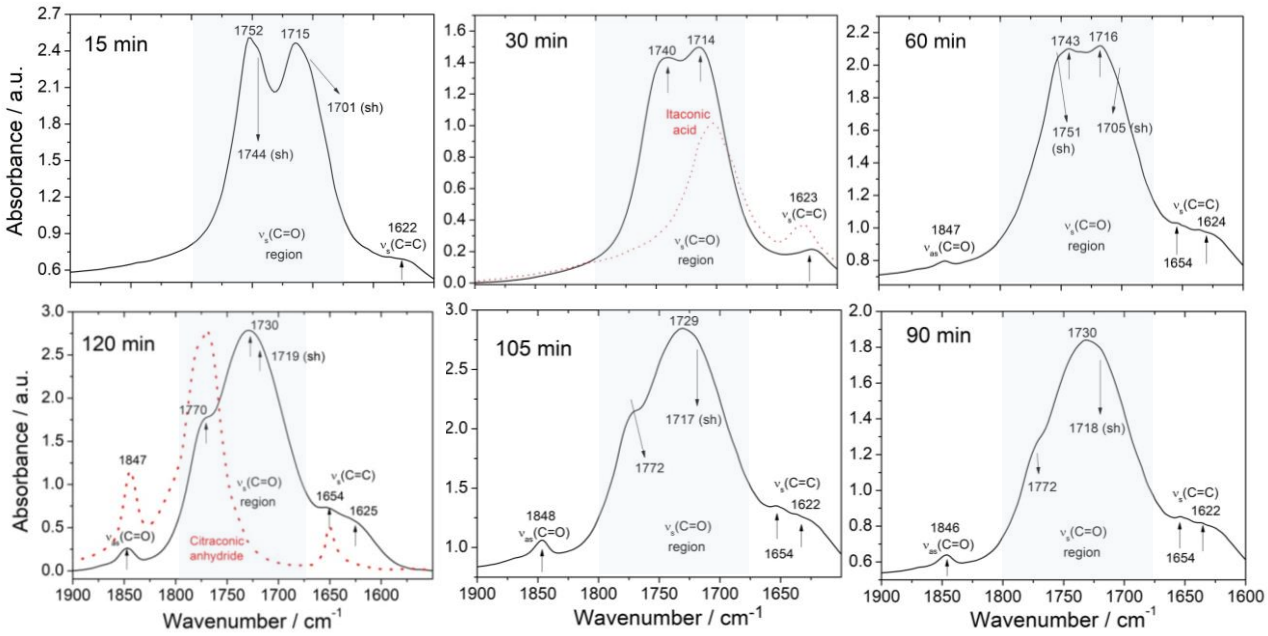

Figure 41.4. FTIR absorption spectra (1900 – 1600 cm^{-1}) of citric acid after different reaction times at 180°C. Reference spectra of itaconic acid (30 min) and citraconic anhydride (120 min) are shown as red dotted lines.

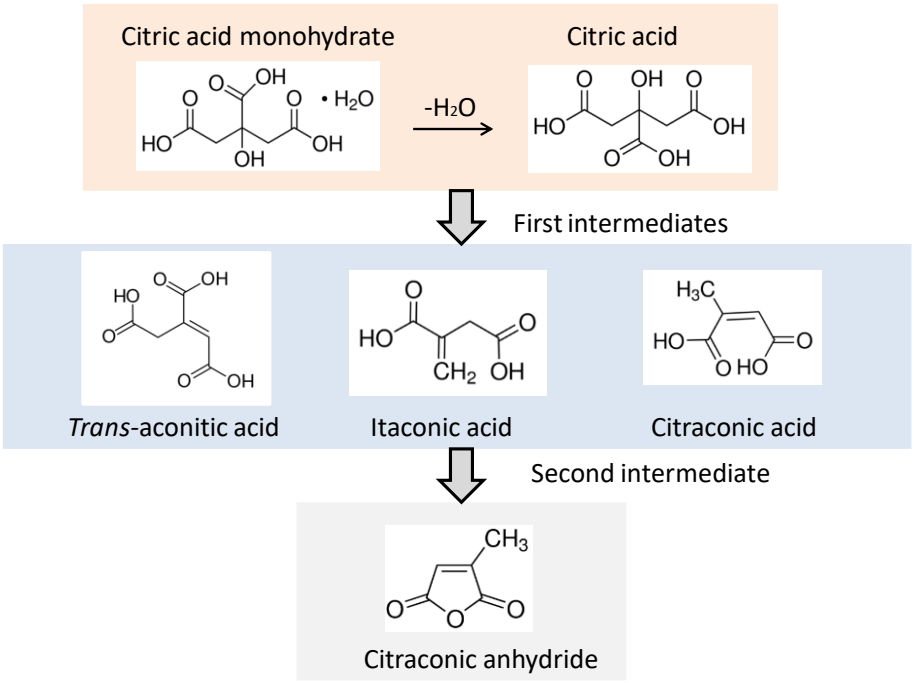

Scheme 41.1. Formation of intermediates during pyrolysis of citric acid

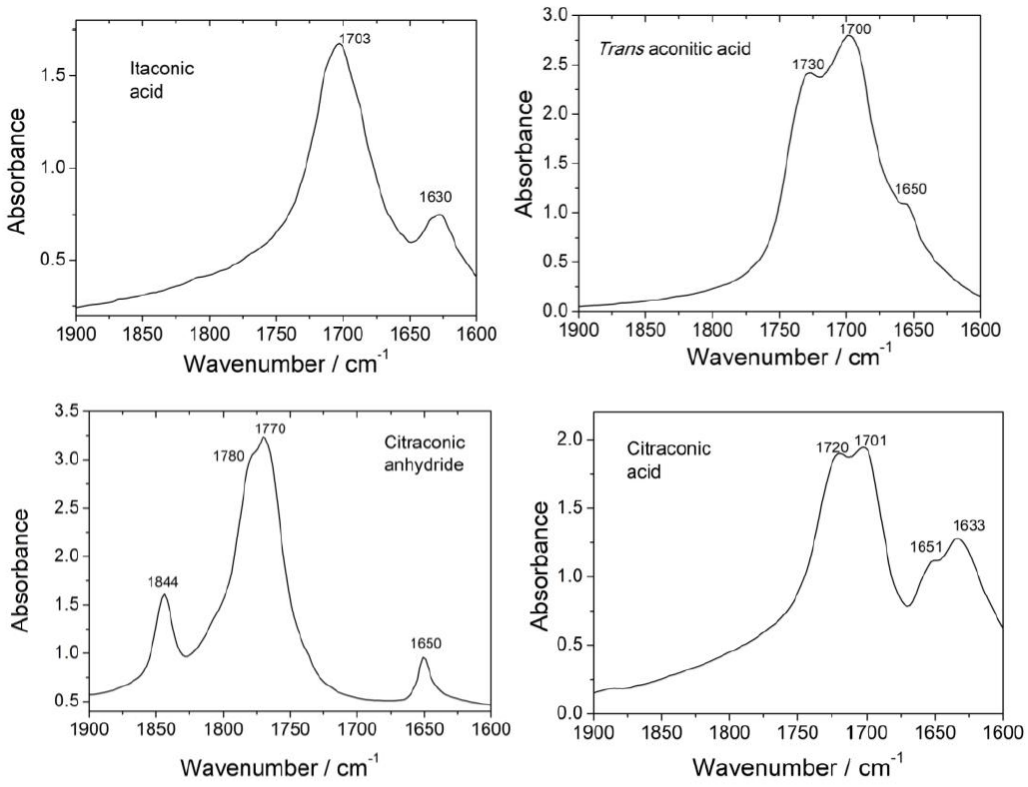

Figure 41.5. FTIR absorption spectra of the citric acid's thermal decomposition intermediates: itaconic acid, *trans*-aconitic acid, citraconic acid and citraconic anhydride, in the 1900 – 1600 cm^{-1} range.

After 30 minutes of reaction, two strong bands at 1752 and 1715 cm^{-1} with two shoulders at 1744 and 1701 cm^{-1} and the C=C band at 1622 cm^{-1} are observed. The shoulder at 1701 cm^{-1} and the increase in relative intensity of the other C=O bands is due to the progressive dehydration of CAM which is taking place in the first stage of the reaction.

After 60 minutes, the dehydration of CAM has almost gone to completion, as shown by the FTIR spectrum, which is similar to that one of ACA. At the same time a new band of small intensity observed at 1847 cm^{-1}, which is assigned to C=O antisymmetric stretching. Another new band at 1654 cm^{-1}, which overlaps with that one at 1622 cm^{-1} and is also assigned to C=C stretching, is detected. The 1654 cm^{-1} band forms after 60 minutes of reaction and increases in intensity with the reaction time; the 1622 cm^{-1} band shows a continuous increase in relative intensity from the beginning of the reaction (**figure 41.6**).

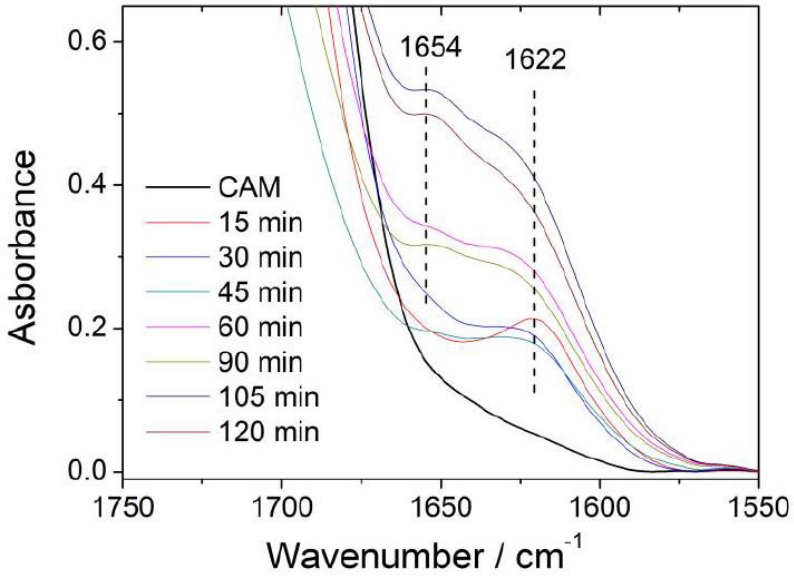

Figure 41.6. FTIR spectra in the 1750 – 1550 cm^{-1} range, of the CA samples at different reaction times.

The spectra from 60 minutes of reaction are also compatible with the formation of other intermediates, the citraconic acid and the *trans*-aconitic acid (**figure 41.5**). The *cis* form is also another possible by-product but it is degrading at lower temperatures than *trans*-aconitic acid (around 130°C) and therefore, the main intermediate that can be detected should be the *trans* species.

The 1847 and 1654 cm^{-1} bands are associated with the formation of an anhydride compound as by-product of the thermal decomposition of CAM, the citraconic anhydride (**scheme 41.1**). The FTIR spectrum of citraconic anhydride in the 1900-1600 cm^{-1} range is, in fact, characterized by intense absorption bands at 1650 (C=C stretching), 1774 (C=O stretching of anhydride carbonyl) and

1844 cm^{-1} (C=O antisymmetric stretching), as we observed in the CA samples (**figure 41.5**). At 120 min the absorption bands at 1774 and 1844 cm^{-1} become more intense and indicate an increase of the amount of the by-product of the reaction. Itaconic anhydride is also a possible product of the reaction, but its FTIR spectrum is characterized by a ν_s(C=C) absorption at a higher wavenumber, 1668 cm^{-1}, and its presence can be therefore ruled out (**figure 41.7**).

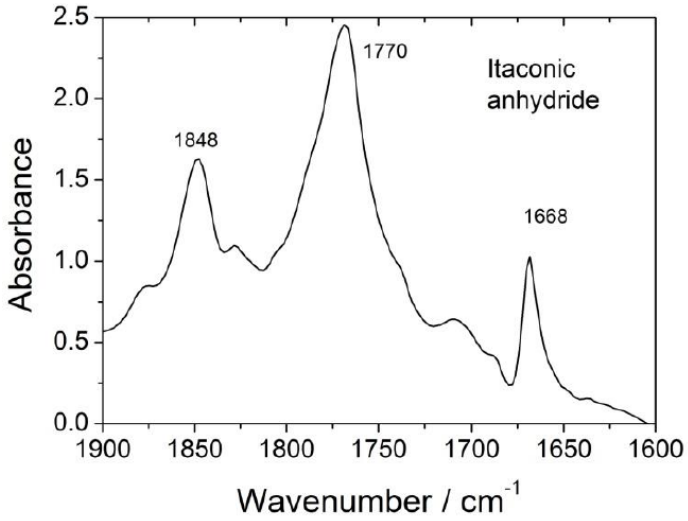

Figure 41.7. FTIR absorption spectrum of itaconic anhydride (1900 – 1600 cm^{-1}).

The FTIR spectra give a good overview of the CA thermal decomposition process. In the first stage, (0-60 min) dehydration of CAM takes place and intermediates start to form as itaconic acid and likely also citraconic acid and *trans*-aconitic acid. After 60 minutes, the formation of another intermediate is observed, namely the citraconic anhydride. The large band peaking at 1730 cm^{-1}, which is still observed after the end of the process, is attributed to the presence of C=O groups which are randomly distributed on the edges of the carbon dots.

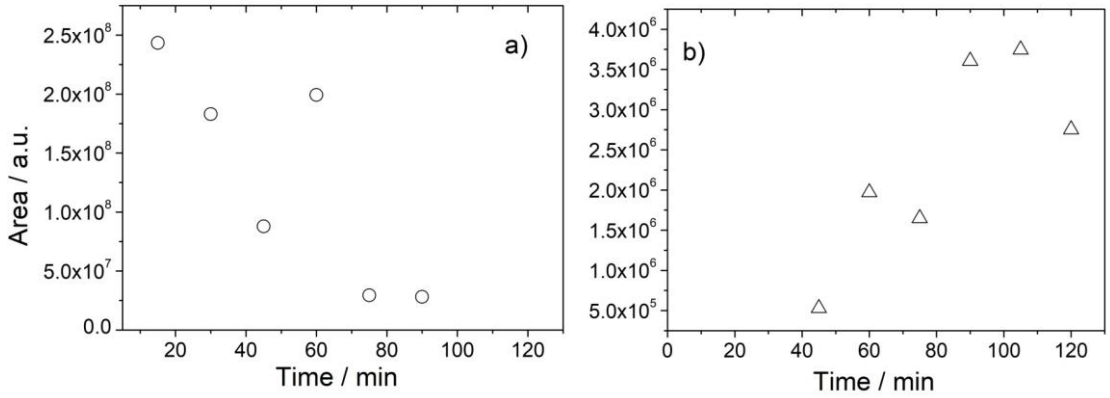

Figure 41.8. Change of citric acid (a) and citraconic anhydride (b) as a function of the reaction time detected by LC-MS.

To support the FTIR findings we have performed LC-MS experiments using the C-dots samples prepared at different reaction times (**figure 41.8**). The amount of citric acid gradually decreases with the time of reaction (**figure 41.8a**); after 90 minutes CA is no more detected. In turn, after 45 minutes, the citraconic anhydride begins to be observed (**figure 41.8b**); its content increases at expenses of citric acid with the progress of the reaction and is still detected after 120 min, in accordance to the FTIR findings. It was not possible by LC-MS to obtain a resolved measure of the intermediates, but the trend observed for citric acid and citraconic anhydride are well in accordance with FTIR.

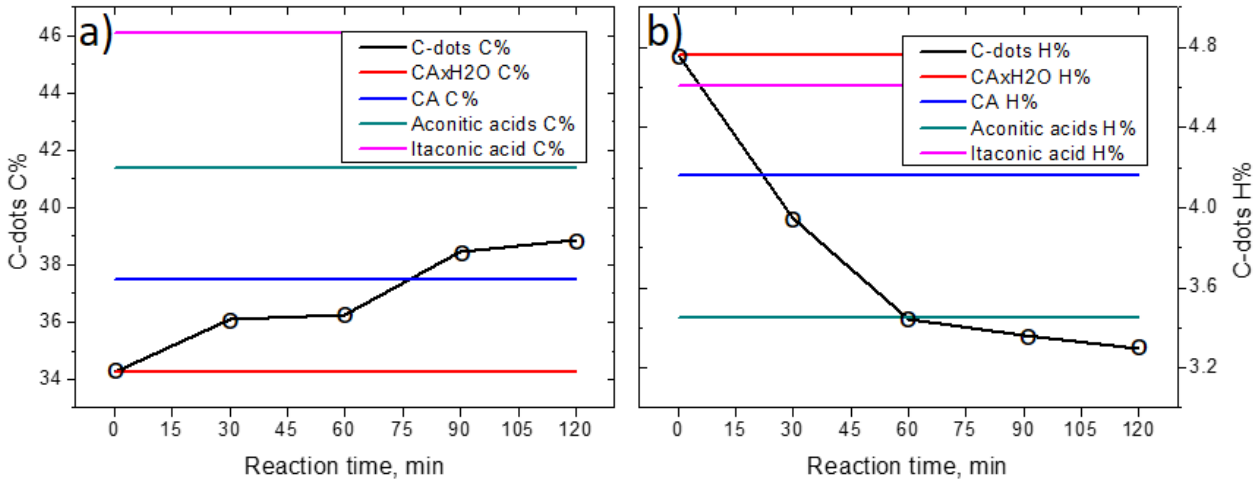

Figure 41.9. Elemental analysis results of C-dots at 30-60-90-120 min reaction time in C% (a) and H% (b) represented by black lines (guide for the eyes) and for comparison, the elemental composition of the expected intermediates: anhydrous citric acid, *cis/trans* aconitic acid and itaconic acid (citraconic acid has the same composition).

Elemental analysis (EA) results (**figure 41.9**) show a continuous increase in C% and decrease in H% due to dehydration and decarboxylation processes **(scheme 41.2**). In the case of H%, a breakpoint at around 60 minutes reaction time is observed, indicating the end of the intensive dehydration stage. The overall picture of thermal decomposition in respect of C% also reveals a breakpoint at around 60 minutes reaction time, which later found to be an important turning point for optical properties too (**figure 41.10**). The phenomena can be explained by considering that the pyrolytic process requires approximately 60 minutes before the luminescent species start to form in a dominating chemical process.

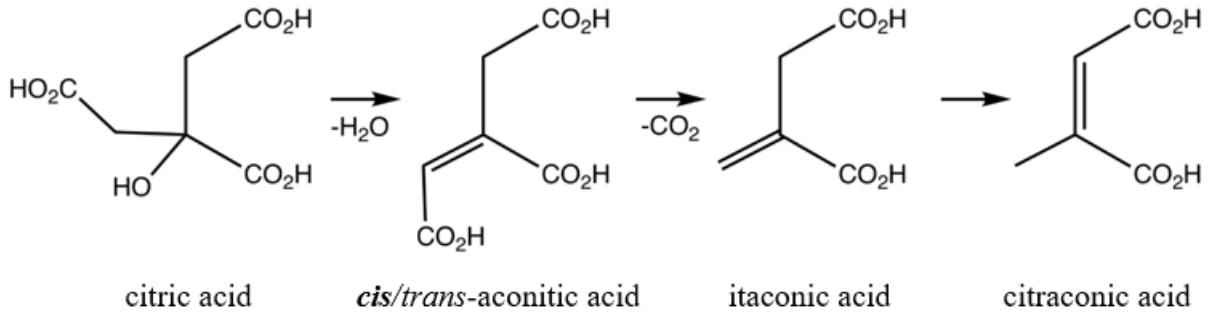

Scheme 41.2. Pyrolysis of citric acid (pyrocitric acids).[101,109] Their anhydrides are also possible intermediates and (by)products.

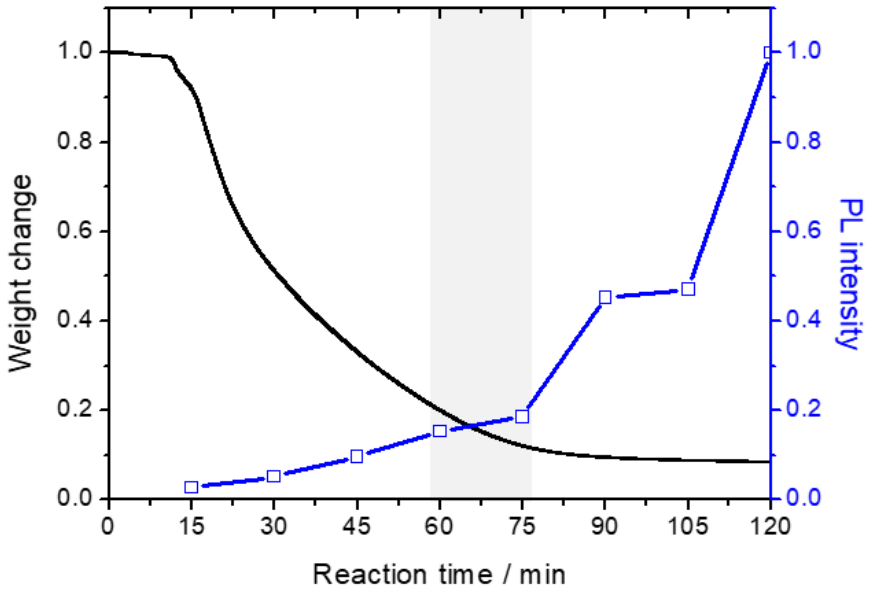

Figure 41.10. Opposite trends of weight loss and measured maximum PL intensities observed during the pyrolysis of CA. A change from exponential to linear decrease in weight (black) and a change from linear to exponential increase of PL intensity can be observed between 60-75 minutes. The lines are only guide for the eyes.

For the TGA analysis, 10 mg powdered CAM was heated to 180°C in 10 minutes and the weigh change was monitored up to 120 minutes. The analysis confirmed a change in the material's thermal response at around 60-75 minutes reaction time (**figure 41.10**). After an initial intensive weight loss, a thermally more stable intermediate mixture was formed, which also correlated to the findings of EA (**figure 41.9**). To emphasize the importance of this reaction stage, the maximum PL intensities of the intermediate products were also plotted and the details of the PL properties can be found in **figures 41.13-15.**

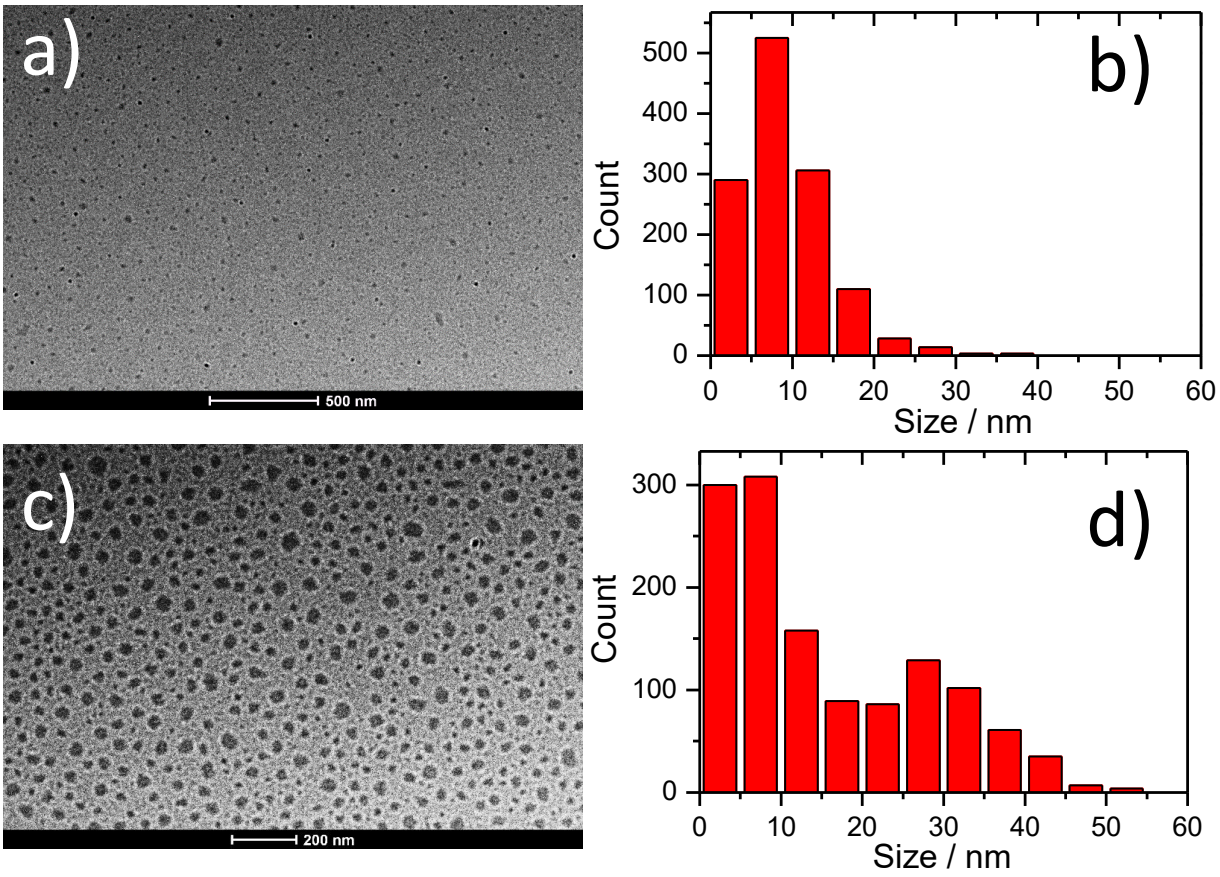

Figure 41.11. Representative TEM images of C-dots obtained from CAM after 30 (a) and 120 minutes (c) of thermal degradation at 180°C. b) and d) panels show the frequency count of the C-dots size obtained by the images a and c, respectively.

The average C-dots dimensions has been measured by TEM and image analysis (**figure 41.11**). After 30 minutes of reaction, the C-dots population is between 5 and 15 nm, while at 120 minutes, the particles show a wider distribution with the growth of C-dots of larger size up to around 30 nm.

We have then coupled the FTIR, EA and LC-MS data with the changes of optical properties of the samples taken at the different reaction times.

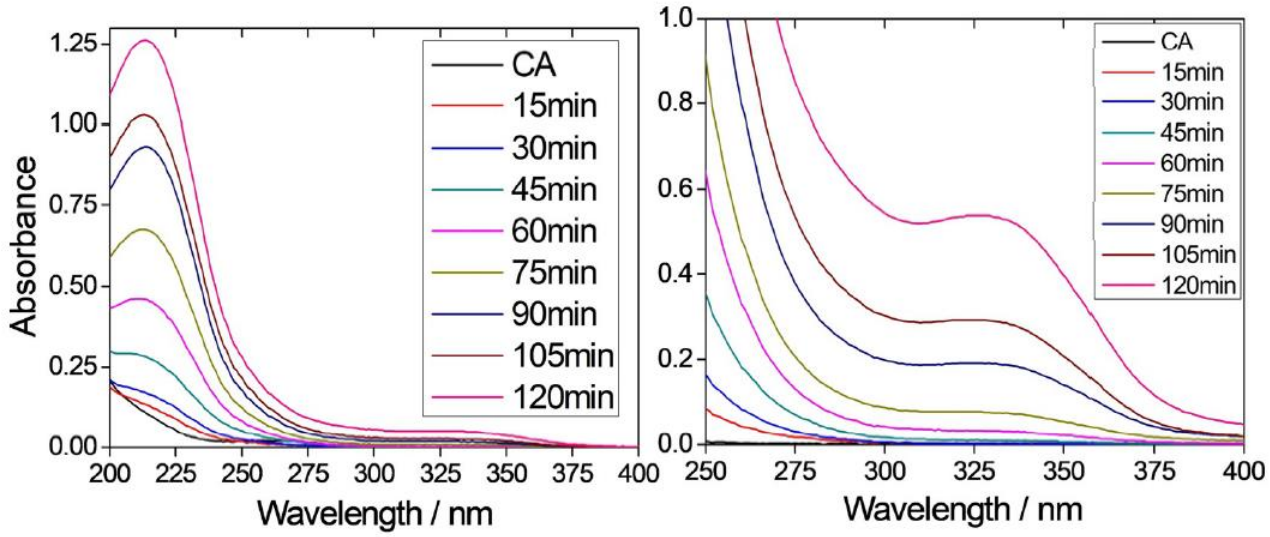

Figure 41.12. UV-Vis absorption spectra of the C-dots derived from thermal decomposition of citric acid at different reaction times and concentrations (left 50 mg L^{-1} and right 500 mg L^{-1}).

The UV-Vis absorption spectra (**figure 41.12**) are characterized in the 200 to 400 nm range by an absorption maximum around 220 nm that increases in intensity with the reaction time. The absorption band is due to the π - π* transition of aromatic sp^2 domains[110] and the enhancement in intensity is attributed to the increase in their number during thermal decomposition reactions. This is an indication of the progressive formation of aromatic π-conjugated structures. The spectra show a second absorption band of weaker intensity, which is detected around 335 nm and assigned to the n - π* transition of C=O bonds.[110] The UV-Vis spectra have been also recorded using a more concentrated solution (500 mg L^{-1}) to observe in detail the change of the 335 nm band as a function of thermal processing (**figure 41.12**). The absorbance increases in intensity with the thermal treatment time.

The CA C-dots PL emission as a function of the excitation wavelength and reaction times (60, 90, 105 and 120 min) is shown by 3D excitation (y-axis) - emission (x-axis) – intensity (false color scale) spectra (**figure 41.13**); the oblique lines are due to scattering effects. **Table 41.1** shows the maximum excitation/maximum emission wavelength pairs as listed in nm's and also displayed on **figure 41.14.** The samples reacted up to 75 minutes show only a very weak, but continuously red-shifting fluorescence: the emission peak shifts from 430 to 485 nm. From 90 to 120 minutes the emission intensity increases with a maximum in the green region, at 500 nm, when excited at 390 nm. The 3D spectra indicate also the presence of a second component in the blue region, whose fluorescence is peaking around 450 nm, upon excitation of 350 nm. This emission also increases in intensity with the reaction time and fits to the PL properties of *trans*-aconitic acid (**figure 41.16.** and

figure 41.18a) with maximum excitation at 350 nm and emission at 460 nm). The fluorescence maximum of the components emitting at 500 nm is independent from the excitation wavelength, indicating that the fluorescent C-dots have homogeneous and similar size of the sp^2 cluster domains.

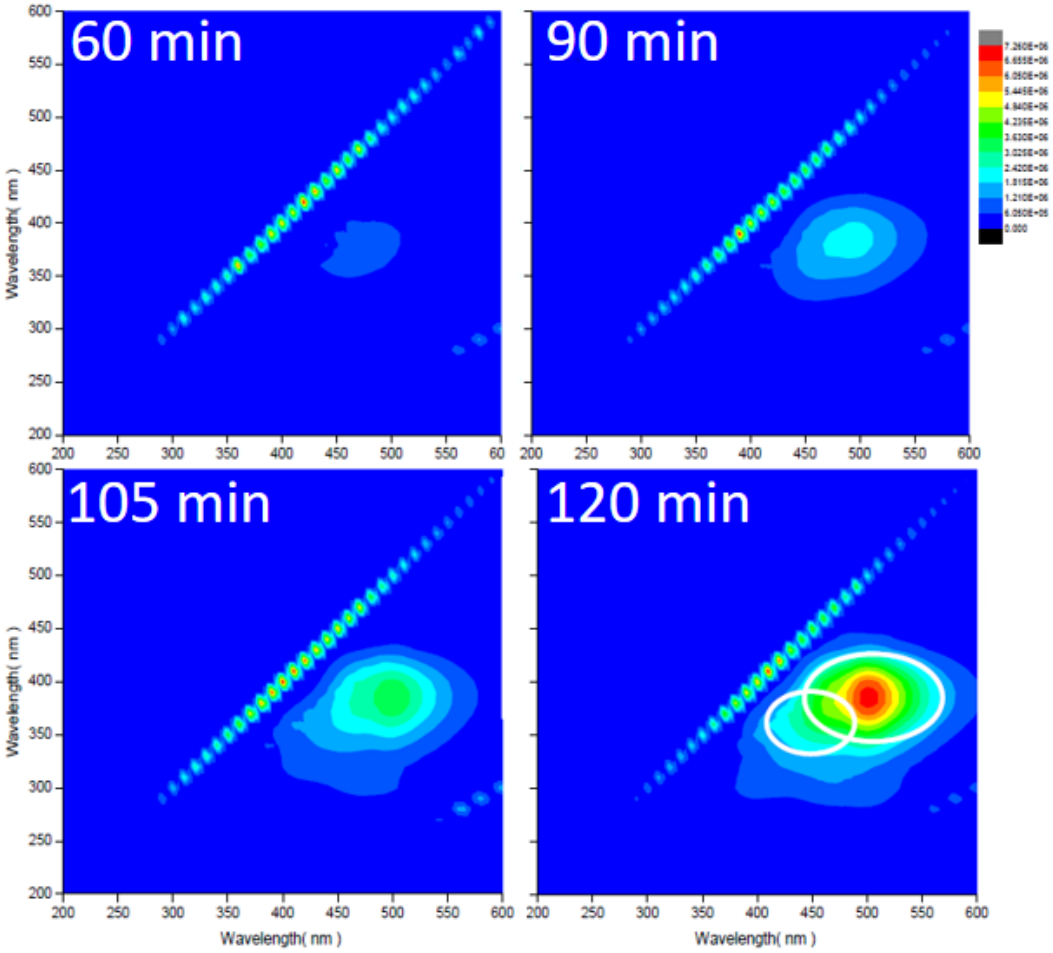

Figure 41.13. 3D excitation (y-axis)-emission (x-axis)-intensity (false colored) spectra of C-dots at different reaction times. The measures have been done at a concentration of 200 mg L^{-1} (aq).

Reaction time	Heating/T	Max. excitation / Max. emission (nm)	Max. PL-intensity (CPS/(mg/L))
15min	oil, 180°C	340/430 (200mg/L)	623
30min	oil, 180°C	360/455 (200mg/L)	1204
45min	oil, 180°C	370/470 (200mg/L)	2242
60min	oil, 180°C	360/465 (200mg/L)	3539
75min	oil, 180°C	380/485 (200mg/L)	4290
90min	oil, 180°C	380/495 (200mg/L)	10434
105min	oil, 180°C	380/500 (200mg/L)	10809
120min	oil, 180°C	390/500 (200mg/L)	23000

Table 41.1. Standardized PL-intensities of samples taken at different reaction times during the thermal treatment of CAM in a 180°C oil bath are calculated for 1 mg L^{-1} concentration (but measured at 200 mg L^{-1}) and the maximum excitation/maximum emission wavelength pairs are displayed in nm. The data extracted from the 3D excitation-emission-intensity spectra.

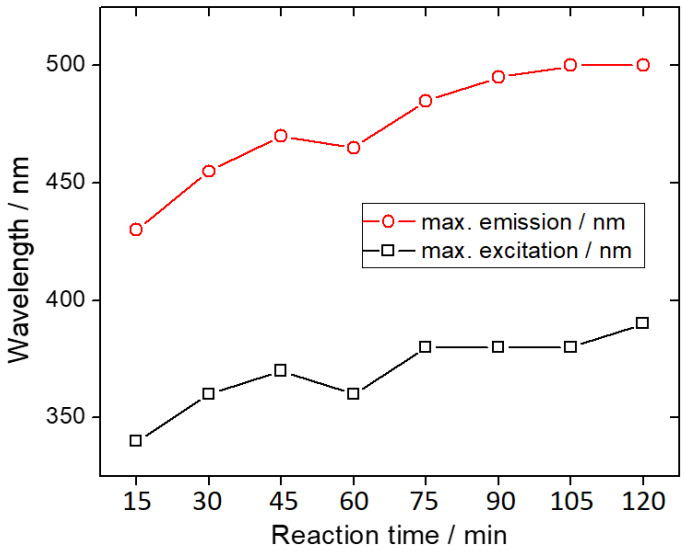

Figure 41.14. Maximum excitation/maximum emission wavelength pairs of CAM-based C-dots at different reaction times. The measures have been done at a concentration of 200 mg L^{-1} (aq). The lines are guide for the eyes.

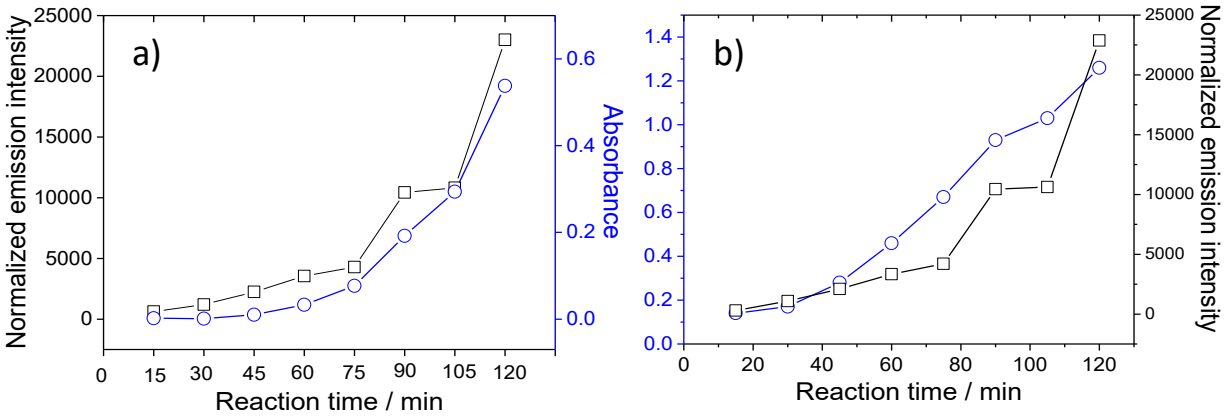

Figure 41.15. Parallel trends of the normalized maximum PL emission intensity (200 mg L^{-1} aqueous solution) and the UV-Vis absorbance intensity at 335 (a) and 220 nm (b) (500 and 50 mg L^{-1} aqueous solutions). The lines are guide for the eyes.

The fluorescence emission has been correlated with the absorbance of the π - π* and n- π* transitions at 220 and 335 nm, respectively (**figure 41.15**). The increase in absorbance of the 335 nm component shows the same trend of the standardized fluorescence emission (**figure 41.15a**), while the 220 nm band exhibits an almost linear change of absorbance as a function of the thermal treatment time (**figure 41.15b**).

The curves in **figure 41.15a** show that the process has two different reaction stages. In the first one, which ends after around 60 minutes, the reaction proceeds quite slowly and the increase of fluorescence and UV absorbance at 335 nm is low; after this time, a quick rise is instead observed.

The increase of fluorescence is faster after the first 75 minutes of reaction and is well correlated to the change of absorbance at 335 nm, which shows a similar trend. The first stage corresponds to the dehydration phase when the formation of fluorescent emitting species is still low. After this stage, which is well defined also in the FTIR spectra by the presence of the C=O vibrational modes due to the precursor CA (**figure 41.4**), the thermal decomposition takes place. The FTIR spectra are characterized by a wide absorption band peaking around 1730 cm^{-1} whose shape is due to the distribution of C=O bonds on different sites of the C-dots. The data show that there is a strict correlation between the increase of emission intensity of the maximum at 500 nm and the absorbance due to the carbonyl groups.

Synthesis of C-dots from intermediates

The thermal decomposition of citric acid has a complex reaction pathway with formation of several intermediates that decompose at different temperatures and can be present as residues of the process. On the other hand, these compounds can also give rise to the formation of C-dots with different fluorescent properties. Not all the intermediates are efficient precursors for C-dots, but at least the *trans*-aconitic acid [111,112] and itaconic acid [113] have been used to synthesize emissive species with a blue fluorescence by co-reaction with ethylenediamine.

We have therefore used the intermediates that we have identified during the thermal decomposition of citric acid, i.e. itaconic acid, citraconic acid, *trans*-aconitic acid and citraconic anhydride, to synthesize C-dots in similar conditions (120 min, 180°C).

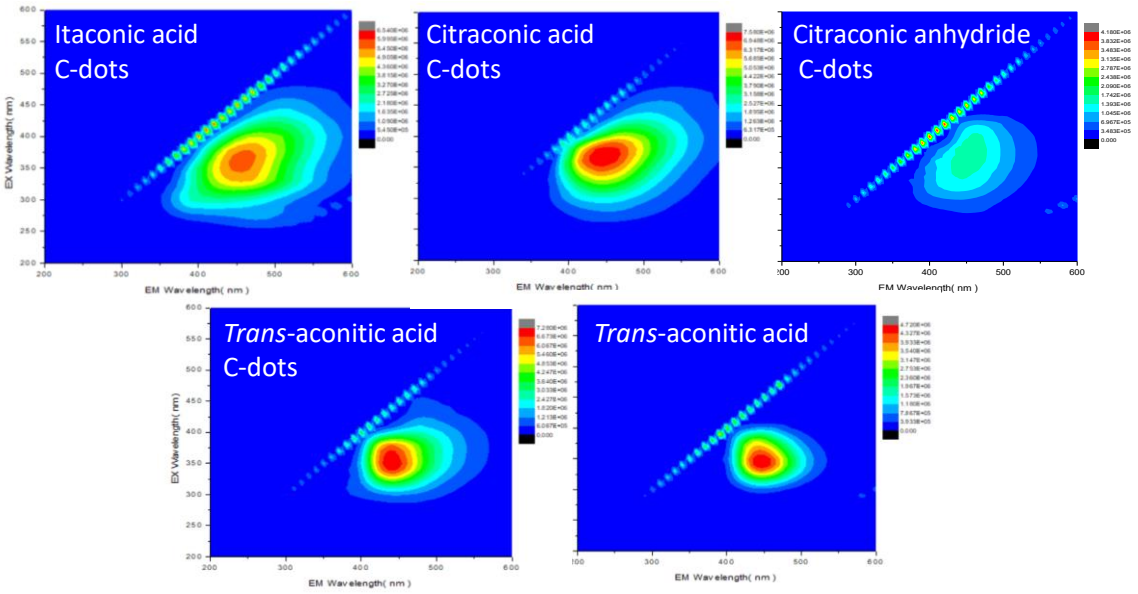

Figure 41.16. 3D excitation-emission-intensity spectra of the C-dots prepared from itaconic acid, citraconic acid, citraconic anhydride (first row) and C-dots from *trans*-aconitic acid and *trans*-aconitic acid itself as the only fluorescent precursor. The measures have been done at a concentration of 200 mg L^{-1} (aq).

The citraconic anhydride C-dots result only weak fluorescence (**figure 41.16**) with an emission maximum around 455 nm whose intensity is only 13% of the CA C-dots. The FTIR spectra show that the citraconic anhydride has almost not reacted, as confirmed by the comparison with the absorption spectrum of the precursor (**figures 41.5 and 41.17**), which is not surprising considering that it is the final pyrocitric acid in the decomposition process. The UV-Vis spectra show that no absorption bands are present beside the 220 nm UV band (**figure 41.17c**).

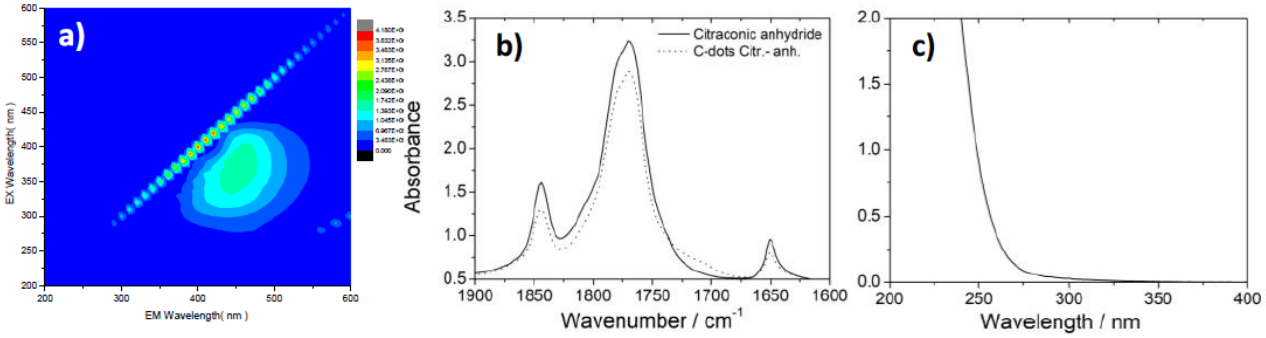

Figure 41.17. a) 3D excitation-emission-intensity spectra of the C-dots prepared from citraconic anhydride; b) FTIR absorption spectra (1900 – 1600 cm^{-1}range) of citraconic anhydride (continuous line) and C-dots from citraconic anhydride (dotted line); c) UV-Vis spectrum of the C-dots from citraconic anhydride (concentration of 50 mg L^{-1}).

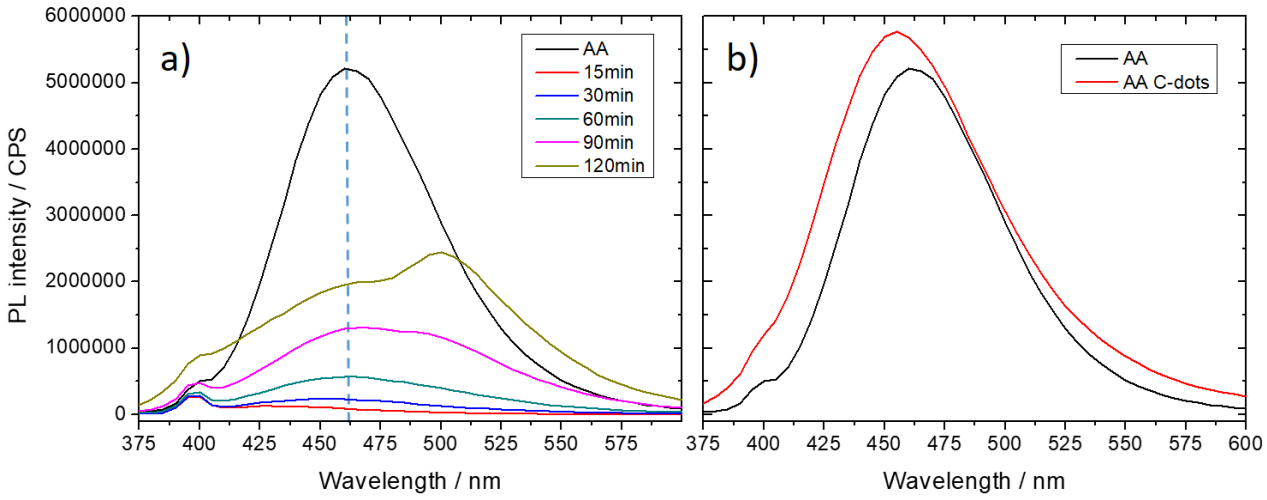

Figure 41.18. PL emission of *trans*-aconitic acid (AA) and CAM-based C-dots at different reaction times (a). The blue dotted line indicates the emission maximum of *trans*-aconitic acid around 460 nm, and the comparison of the PL spectra of AA and AA-derived C-dots (b). All samples measured in a 200 mg L^{-1} aqueous solution and excited at 350 nm.

The other precursors produce instead C-dots with a higher emission, in particular those from *trans*-aconitic acid, exhibiting the typical absorption bands at 220 and 350 nm. The emission maximum is centered for the different C-dots around 450 nm, while CA C-dots have a maximum around 500 nm. These spectra well explain the origin of the second (weaker) fluorescent component

in **figures 41.13** and **41.18a**. This is, in fact, due to the C-dots, which form upon thermal decomposition of the CA intermediates (e.g. AA). The final product of the synthesis via citric acid is therefore formed by two families of C-dots; one with a stronger emission in the green, around 500 nm, and a second one with lower, blue emission at 450 nm, due to the carbonization of the intermediates and molecular *trans*-aconitic acid. Therefore, a particular case is represented by *trans*-aconitic acid, which allows forming fluorescent C-dots, but is also highly emissive as precursor. *Trans*-aconitic acid shows, in fact, an intense fluorescence centered at 460 nm (**figure 41.16**) and the derived C-dots have a very similar slightly blue shifted emission (**figures 41.16 and 41.18b**). The emission fingerprint appears more centered around the maximum, suggesting the formation of C-dots with a homogeneous structure.

Stability of the C-dots

The stability of the C-dots has been studied by measuring the emission of aqueous samples as freshly prepared and after storing for several days (**figure 41.19**), which was compared to the PL properties of freshly prepared solutions of aged solid samples (**figure 41.20**). In the solid state, the emission remains very stable and after 4 days of the preparation, no changes in the 3D excitation-emission-intensity spectra have been observed. However, a fresh solution of a one year aged solid sample provided a 50 nm blue shifted and 45% weaker fluorescence upon the excitation at 340 nm.

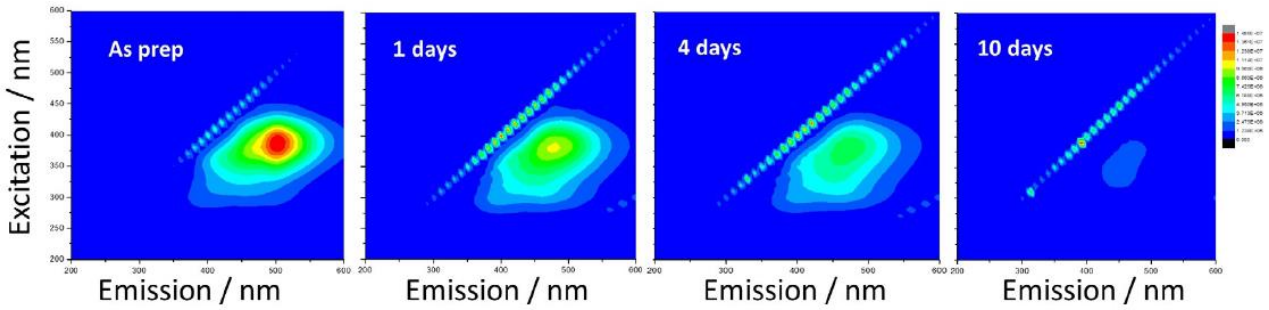

Figure 41.19. 3D excitation–emission–intensity spectra of C-dots in water directly after preparation and after 1, 4 or 10 days of aging. The concentration of C-dots in water was 200 mgL^{-1}.

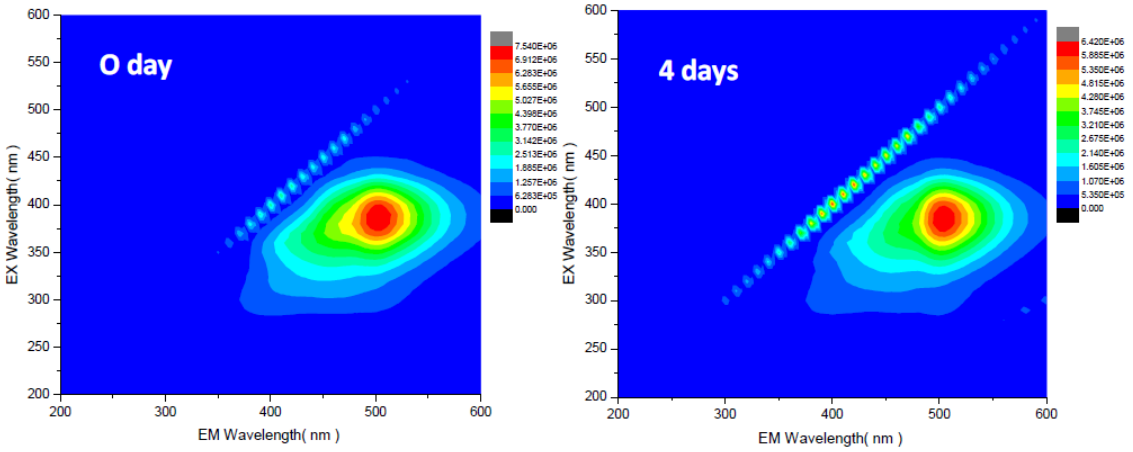

Figure 41.20. 3D excitation-emission-intensity spectra of aqueous solutions (200 mgL^{-1}) from fresh (left) and 4 days old (right) C-dots solid samples.

If the C-dots are instead dissolved in water, the samples show a low hydrolytic stability and a 70% decrease in intensity of the 500 nm emission band after 1 day of storage is observed (**figure 41.19**). After 4 days, the emission intensity decreases to 26% with respect to the as-prepared C-dots and at 10 days, it is almost completely quenched. The pH of the C-dots aqueous solution is 4.5.

The change of emission spectra when the C-dots are dissolved in water is due to the hydrolytic reactions of the surface groups. They are a source of the emission of C-dots at 500 nm and their reaction with water is reflected in the lowering intensity. Quenching effects due to the formation of hydrogen bonds with water on the surface also cannot be ruled out.

We have also tested the stability of the C-dots in basic aqueous solutions (**figure 41.21**) at pH 11, by using KOH (aq) and NH_3 (aq). In this case, the emission of the C-dots is not quenched with time and results more stable emission, which maximum slightly shifts to lower wavelengths, from around 500 to 480 nm.

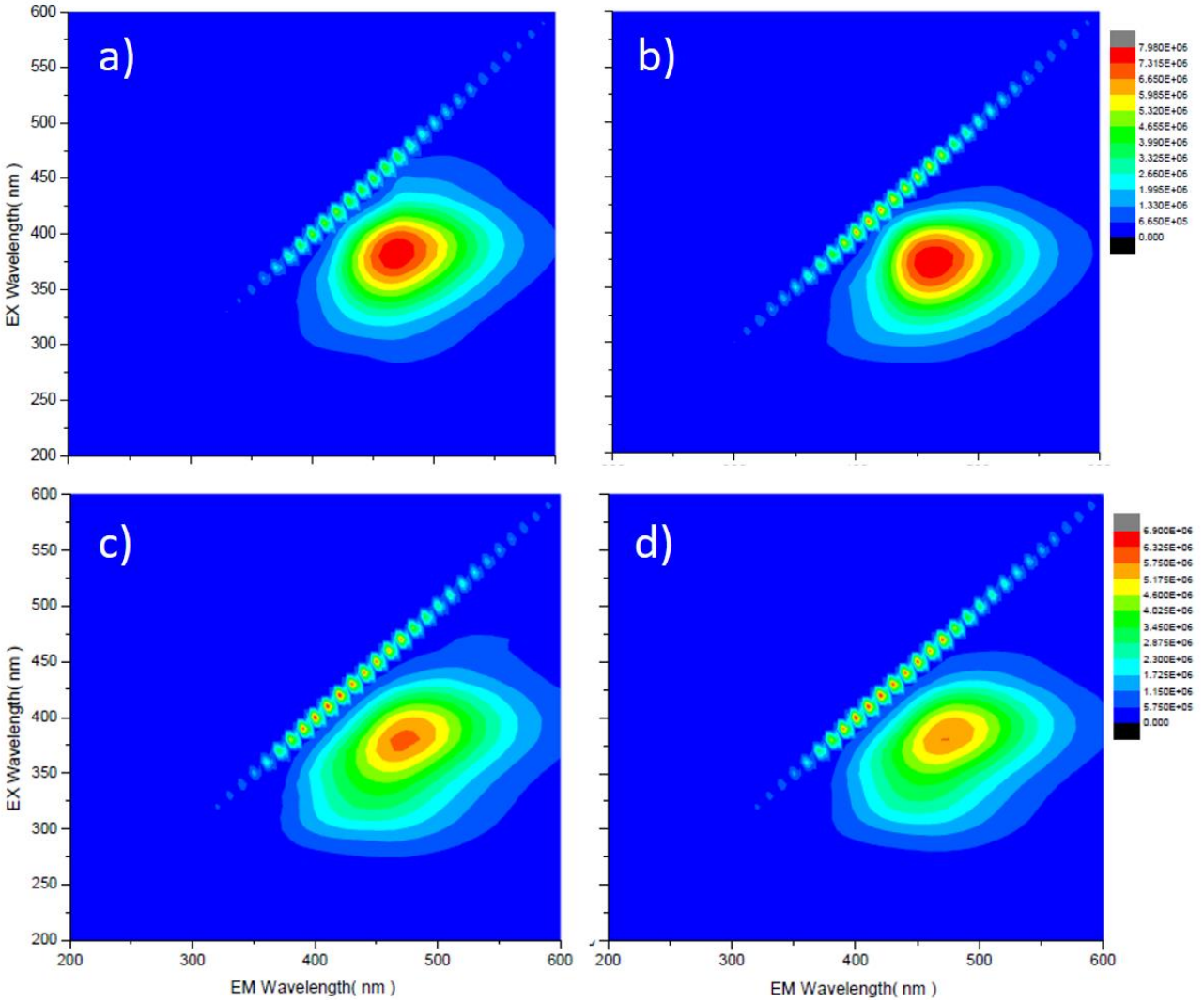

Figure 41.21. 3D excitation-emission-intensity spectra of C-dots in KOH aqueous solution, as prepared (a) and after 1 day of aging (b) and C-dots in NH_3 aqueous solution, as prepared (c) and after 1 day of aging (d).

Surface modification by APTES

The chemical modification of C-dots surface, which is of pivotal importance for building C-dot-based solid-state fluorescent materials,[114,115] is generally obtained by one-pot synthesis with specific organosilica precursors bearing amino groups. [116,117] This approach, however, changes both the inner and outer C-dots structure and it can not be used to really discriminate the influence of the surface passivation on the C-dots photoluminescence. On the other hand, the post-functionalization of the C-dots surface is rarely reported in the literature,[99] and, in some cases, the functionalization appears not fully characterized.[107]

We have used 3-(aminopropyl)triethoxysilane (APTES) as a surface-modification agent to unveil the role of the surface groups on C-dots emission (**figure 41.22**). The functionalization with

APTES produces a strong change in the emission spectra of the C-dots. A new intense violet emission band peaking around 410 nm is observed with a second fluorescent component with a maximum around 480 nm. It should also be noticed that the APTES functionalization changes the pH of the aqueous solution from acid, pH=4.5, to basic, pH=11. The change of the emission spectra is also reflected by the UV-Visible absorption (**figure 41.23**).

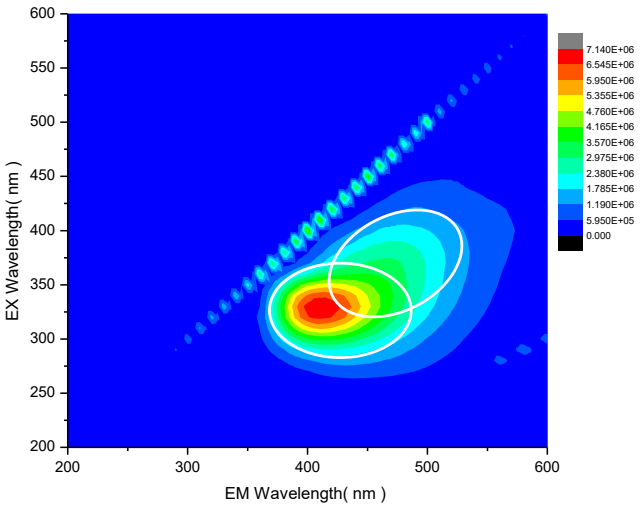

Figure 41.22. 3D excitation-emission-intensity spectra of C-dots after functionalization with APTES.

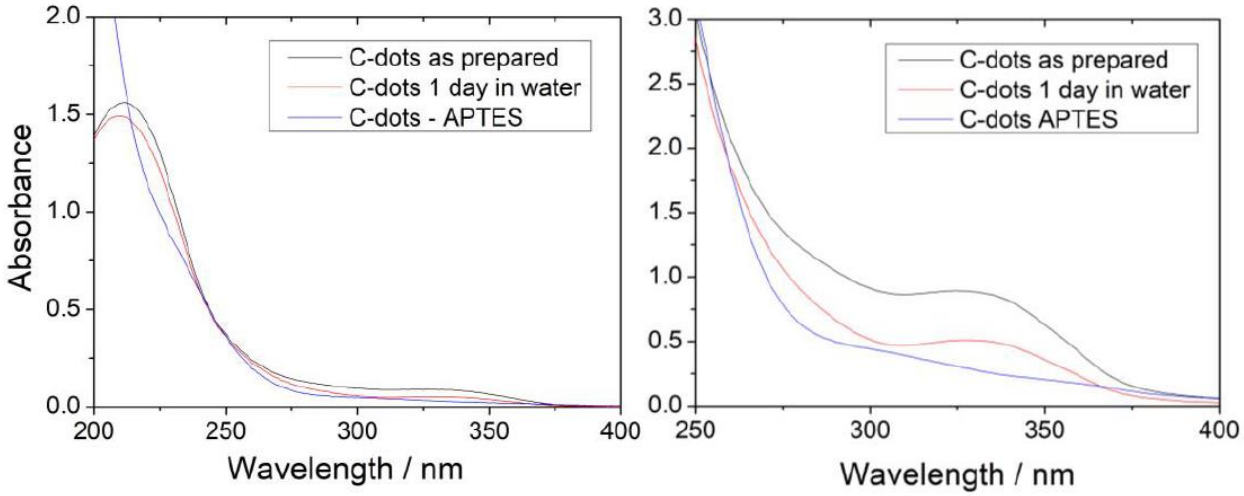

Figure 41.23. UV-Vis absorption spectra of C-dots after preparation (black line), after one day aging in water (red line) and after functionalization of as prepared samples (blue line) measured at a concentration of 50 mg L^{-1} (left) and 500 mg L^{-1} (right).

The absorption band around 335 nm decreases in intensity with aging and disappears after APTES functionalization, while the UV band at 220 increases in intensity.

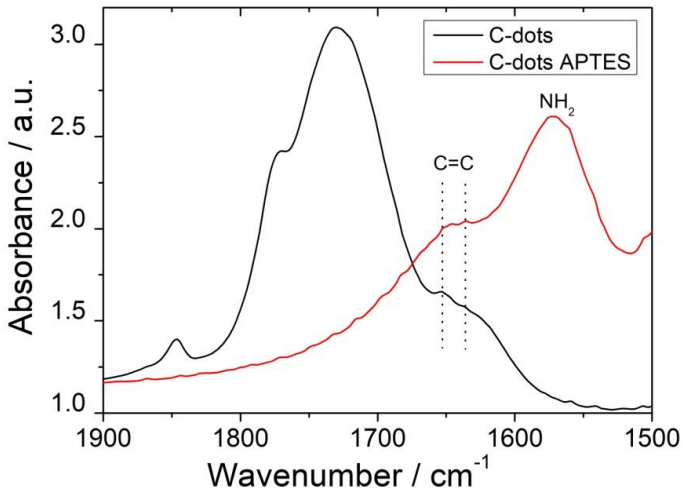

Figure 41.24. FTIR absorption spectra in the 1900 -1500 cm^{-1} range of as prepared C-dots (black line) and C-dots after functionalization with APTES (red line).

The FTIR absorption spectra in the 1900 – 1500 cm^{-1} range of the APTES functionalized C-dots (**figure 41.24**) show that the carbonyl signal (C=O stretching) in the C-dots disappears (red line). Besides a long tail at lower wavenumbers, which could be the signature of residual carbonyls, the intense absorption band peaking at 1730 cm^{-1} is no more detected. On the other hand, the detection of the band at 1570 cm^{-1}, due to the NH_2 scissoring mode of the amine in APTES, confirms that the C-dots have reacted with the organosilane. The absorption band at 1650 cm^{-1}, which is observed as an intense shoulder, is also in the same range of C=N modes and the relative increase in intensity of this band could be correlated to the reaction of primary amines of APTES with the carbonyls on the surface of the C-dots. The low emission of the CA C-dots is due to the presence of oxygen containing groups, such as C=O, COOH and C-O-C, that act as surface traps. The photoluminescence and optical absorption are therefore affected by the reaction of C-dots with APTES, which would be bonded to the surface as shown by the presence in the FTIR spectra of Si-O-Si and Si-O-C modes (not shown in figures). Silica bonds are also observed due to the reaction of Si-OR groups to form a Si-O-Si network. Silica may also form a small passivation layer on the surface of the C-dots, which is also a cause of the photoluminescence increase. Another interesting property of APTES functionalized C-dots is the stability in aqueous solutions; after 10 days (**figure 41.25**) and 2 months (not shown in figures) of storage in water the emission does not change. The formation of a silica shell around the C-dots is the most probable explanation, because the surface is no more directly affected by the surrounding chemical environment and the C-dots increase their durability in water.

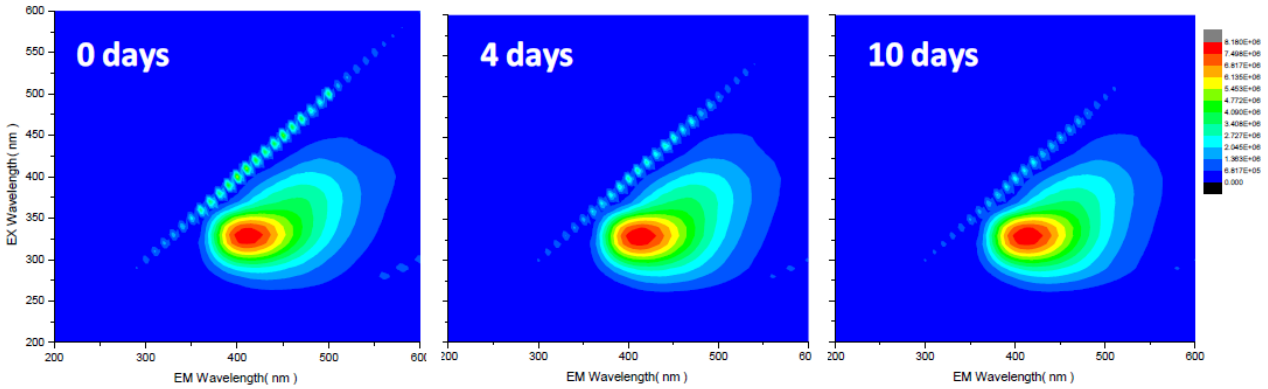

Figure 41.25. 3D excitation-emission-intensity spectra of C-dots functionalized with APTES and aged for different times: 4 and 10 days. The concentration of C-dots in water is 200 mg L^{-1}.

Lifetime measurements

Lifetime analysis has been performed on the C-dots prepared by CA (2 hours thermal treatment samples) and upon modification with APTES (**figure 41.26**). In the CA C-dots samples the fit has been accomplished using two exponential decays of 0.45 and 3.15 ns; the fast one is within the resolution limit of the system. We have analyzed the recorded streak image by extracting the spectrum over two different time windows in the 0 - 2.5 and 2.5 - 20 ns ranges (**figure 41.26b**). The curves show a spectral contribution at smaller wavelengths (at about 410 nm) which is characterized by a shorter decay. This difference is also pointed out by the decay times of two small spectral windows (20 nm in width) centered at 415 and 480 nm. The contribution of the fast decay is larger in the first case. The analysis of the two spectra in the energy space by Gaussian deconvolution has also confirmed the presence of two different emission bands, at 2.6 (416 nm) and 3.0 (480 nm) eV.

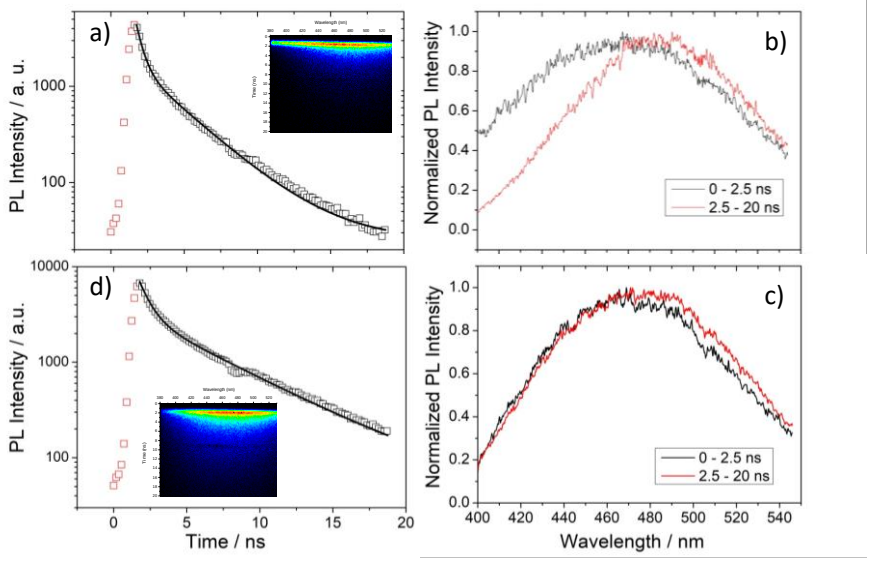

Figure 41.26. a) and d), decay time estimated through the integrated spectrum of CA C-dots and APTES C-dots, respectively (the spectrum has been recorded in the 400-515 nm range). b) and c) the fit of the two components.

The decay curves of CA-APTES samples have been also fit with two exponential decays of 0.77 and 5.48 ns. However, the analysis of the spectra at different time windows or the decays at a specific wavelength has not shown any faster spectral contribution whilst the deconvolution of the spectrum with two Gaussian components gives the same bands gathered before (at 2.95 and 2.62 eV). If we look at the fractional contribution of the two decays to the steady state emission we obtain that the CA-APTES fast decay weights for 59% whilst the slow one for 41% in. In the CA sample the fast component contributes for the 88% whilst the slow one for the 12%. This difference can explain why we have observed the decrease of the fast component only in the CA sample. We have also tried to associate the slow and fast decays to specific emission bands. To achieve such an attribution, we would need measurements with a larger time sensitivity, in the present case the fast component is less than two times the temporal resolution in the best case (CA-APTES sample). However, the presence of the fast decay even in the red tail of the spectrum in both samples, where any possible spectral contribution of the 3.0 eV band should be negligible, gives room to a different interpretation. The fast decay could be due to some non-radiative de-excitation pathway, which decreases the overall emission intensity. This non-radiative pathway could be accessible to any emitting centre within the nanoparticle, both to the 2.6 and 3.0 eV bands. This response can be correlated to some core-shell system, where the emitting centres are at the surface and the non-radiative channels may lead to de-excitation through the core of the nanoparticle.

The fact that the fractional contribution of the fast decay in CA-APTES is lower than in CA sample indicates that the functionalization somehow decreases the rate of these non-radiative channels. As for the decay times of these two bands can be supposed that they are of the same order of magnitude of the slow component in both the samples, thus making difficult any temporal discrimination, at least in the present experimental conditions.

4.1.4. Conclusions

Thermal degradation of citric acid is a complex process involving the formation of several intermediates during different dehydration and decarboxylation processes, which was not reportedly fitted to the synthesis process of C-dots before. The reaction needs to be carefully controlled to be reproducible and reliable as the intermediates, such as itaconic acid or *trans*-aconitic acid, can also form fluorescent C-dots, which emit at lower wavelengths with respect to the CA C-dots. The final product of the thermal degradation of citric acid can be, therefore, a combination of C-dots formed by citric acid and its intermediates with different emissions from violet to blue.

The C-dots obtained from *trans*-aconitic acid, in particular, show a narrower emission, which is less sensitive to the excitation wavelength and is correlated with the formation of emitting centers with similar structures. As molecular aconitic acid also exhibit fluorescence in the same region, it cannot be excluded, that this intermediate responsible (even alone) for the emission band around 450 nm, which usually present in the PL spectra of citric acid based C-dots. The identification of this intermediate in the process probably have a great significance, as its structure closely related to numerous reported blue emitters in N-doped C-dots (chapter 4.2 and 4.3).

The stability of the citric acid C-dots in water is very low, but the functionalization with 3-aminopropyltriethoxysilane, besides increasing the emission intensity, reduces also the C-dots quenching in aqueous solutions. Unveiling the synthesis details has shown to be a mandatory step to design a reproducible and reliable process for producing fluorescent C-dots.

4.1.5. Additional preliminary data

The 120 min CA C-dots' interaction with APTES resulted an unexpected 90 nm blue shift in PL emission (**figure 41.22**). To investigate the possible effects on PL by introducing an amino group (similar to the one of the APTES'), in a preliminary study, small organic amines were added to the CA C-dots aqueous samples under the same conditions: 10 mg C-dots / 10 ml water was stirred for 24h at room temperature with 0.33 mL of the indicated amine. The 3D spectra (**figure 41.27.**) revealed, that addition of only (water miscible) small amines do not result the same 90 nm blue shift in PL emission, however a smaller, 30 nm shift was detected in all the cases. This preliminary result also confirm the complex role of APTES in C-dots functionalization.

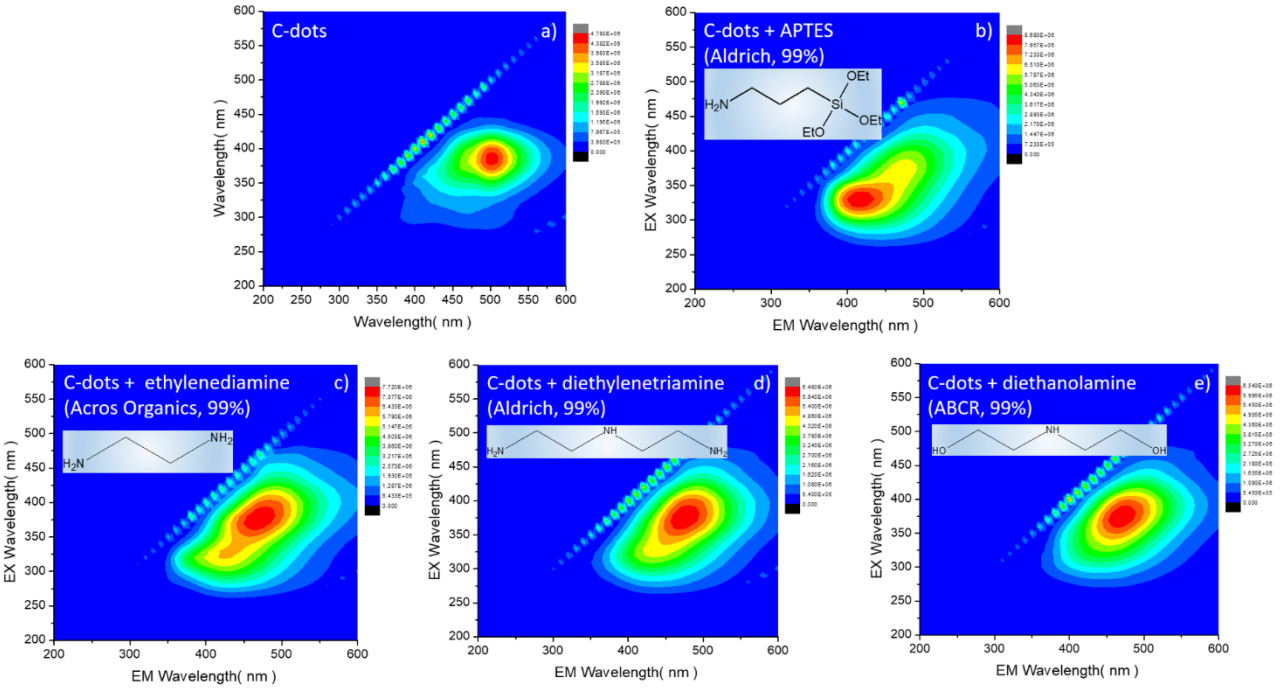

Figure 41.27. 3D excitation-emission-intensity spectra of C-dots formed in the 120 minutes reaction (a) and 3D PL spectra of its derivatives obtained by functionalization with APTES (b), ethylenediamine (c), diethylenetriamine (d) and diethanolamine (e). All samples measured at 200 mg C-dots L^{-1} concentration (by not counting the additional weight of the amines).

4.2. Citric acid – Tris based carbon dots

This chapter is an extended study of chapter 3, but the focus is not on the synthesis methods, but instead more on the formation of the very fluorescent citric acid-Tris based C-dots (**figure 42.1**). Parts of this chapter were recently submitted to *Carbon* and it is currently under review.

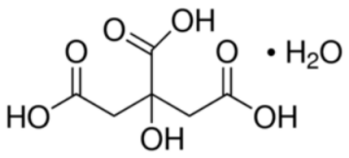

citric acid monohydrate (CAM),
2-hydroxypropane-1,2,3-tricarboxylic acid;hydrate
CAS: 5949-29-1
M_r: 210.14
mp: 135°C
decompose: >175°C

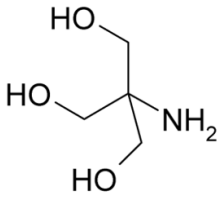

tris(hydroxymethyl)aminomethane (Tris),
2-amino-2-(hydroxymethyl)propane-1,3-diol
CAS: 77-86-1
M_r: 121.13
mp: 167-172°C

Figure 42.1. Structure and properties of citric acid monohydrate and Tris

4.2.1. Introduction

Among numerous possible precursors, citric acid (CA) can be used alone, [88,89] (chapter 4.1.) to obtain moderately fluorescent C-dots in their bottom-up syntheses, but for exceptionally high fluorescent quantum yields (QY) we must combine with other (very often amino group-bearing) chemicals (chapter 3).[65,91,102,104,118,119] The addition of other precursor(s) offer various combinations of chemical reactions, at first of course on the molecular level, which naturally evolve to macromolecular and even nanoparticle/particle degree, making it challenging to generalize formation types.

Since the discovery of C-dots in 2004,[1] three different categories have been identified: besides the widely used graphene quantum dots (GQDs) and carbon (nano)dots (C-dots, CDs, CNDs), the (partially) polymeric fluorescent dots are just recently defined as carbonized polymer dots (CPDs)[120,121] and joined the growing family of C-dots. This peculiar group, in the aspect of fluorescence, lies between the molecular fluorophores and the carbonized nanostructures as a natural transition stage in numerous cases. CPDs represents an emerging group of nano-sized and less-carbonized, aggregated or cross-linked polymers, prepared from simple monomers.[120-122]

The CPDs quantum yield is generally higher than the other (more carbonized) C-dots, justifying studies to reveal the origin of their photoluminescence. It is clear that there is not a general mechanism responsible for the emission, but rather an interplay of many physical phenomena. Surface state, subdomain state, molecular state, and crosslink enhanced emission (CEE) effect have been already identified as possible processes determining the photoluminescence. However, the molecular states of specific fluorophores formed during the synthesis, and the amplification of their emission, induced by the more cross-linked environment around emitting centres, i.e. CEE, appear dominant factors in the overall optical properties.[91,95,123-125]

Some authors have reported that fluorescent molecules, such as IPCA (5-oxo-1,2,3,5-tetrahydroimidazo[1,2-a]pyridine-7-carboxylic acid) and related 2-pyridone derivatives are the main source for the C-dots (CPDs) emission if citric acid and various amines applied as precursors. (**figure 42.3**.)[125] The quantum yield often decreases as the carbonization increases, which indicates that carbon-core transitions are less efficient than molecular transitions to produce photoluminescence.[123] Although different works confirm these findings, it is also clear that the confinement of fluorescent molecules in a constrained environment is a key factor for achieving those high QY values, which are typical of C-dots.[126]

One of the highest reported quantum yield of C-dots (99%)[17] was obtained by the very fast microwave-assisted reaction of CA and 2-amino-2-(hydroxymethyl)propane-1,3-diol (Tris) but its formation was not thoroughly studied. The reported enchantingly intensive PL emission in the violet range turned our attention to this system (chapter 3).

Citric acid bears three carboxyl and one hydroxyl groups and it is capable of copolymerization without any catalyst with appropriate hydroxyl functionalized precursors[127,128] to form environmentally friendly, biodegradable polyesters (**figure 42.2**).

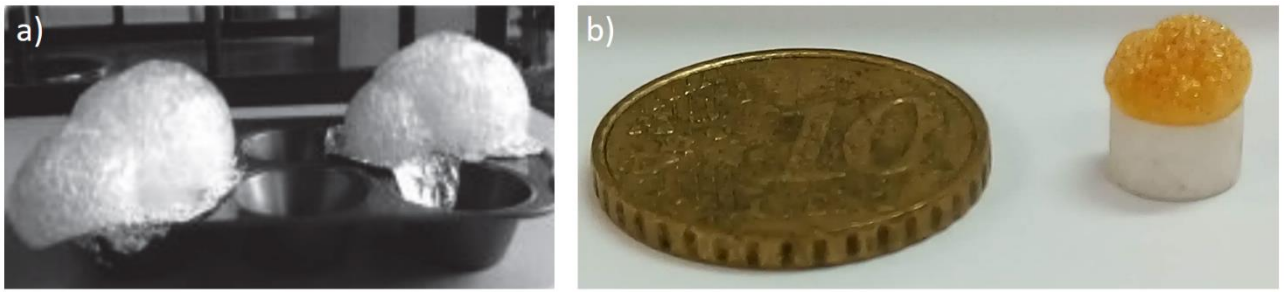

Figure 42.2. a) Foamy polymer made by the reaction of citric acid and glycerol at 170ºC for 1h. Reproduced from reference[128] (open source). b) The product of the reaction of citric acid and Tris at 180ºC for 2 h have similar appearance.

Tris, as an alkanolamine, bearing multiple hydroxyl and an amine functional groups, is similarly able to form the aforementioned (glycerol-like) polymer structure obtained by condensation with CA. The formation of OPCA (3,5-dihydro-3,3-bis(hydroxymethyl)-5-oxo-*2H*-oxazolo[3,2-a]pyridine-7-carboxylic acid), a molecular fluorophore in CA-Tris C-dots has been already reported (**figure 42.3c**),[129] therefore we turned our attention to the possible effects on the fluorophore during polymerization.

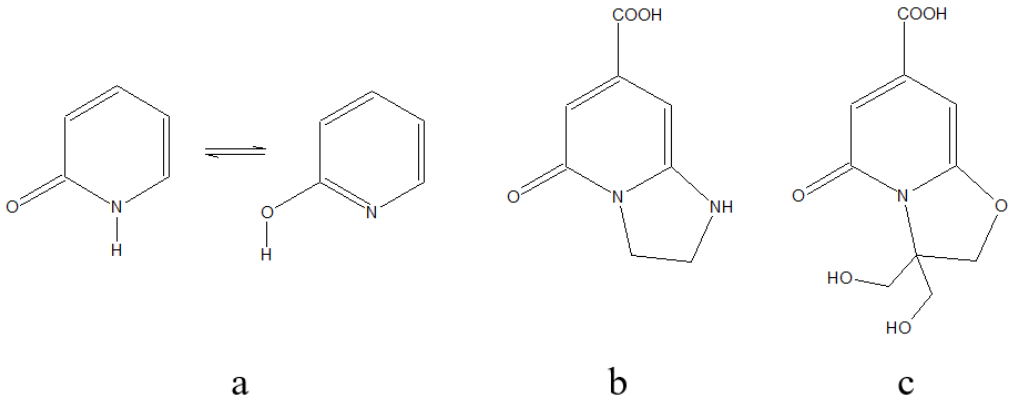

Figure 42.3. Tautomer forms: 2-pyridone and 2-hydroxypyridine (a), IPCA (b) and OPCA [129] as the suspected fluorophore in the CA-Tris-based C-dots (c)

In this chapter, we examine the evolution of carbon dots and their photophysical properties from the molecular precursors of CA and Tris in a simple pyrolysis process by focusing mainly on the early stage of the carbonization process. Based on a few preliminary experiments we selected the optimal 3:1 molar ratio of CA and Tris (chapter 3) due to the achieved very intense fluorescence and still satisfying water solubility. The reaction was carried out under open air in a simple solvent free pyrolysis process at mild temperature (180°C). Samples were taken at defined reaction times for physical and optical examination.

4.2.2. Experimental

Chemicals and Reagents

Citric acid monohydrate (CAM)	Fluka, >99.5%
2-amino-2-(hydroxymethyl)propane-1,3-diol (Tris)	Carlo Erba, >99.5%
3-(aminopropyl)triethoxysilane (APTES)	Aldrich, 99%
FTIR grade potassium bromide	Aldrich >99%

All chemicals were utilized without further purification.

In-site produced Milli-Q water was used for the analysis.

None of the precursors showed observable fluorescence under our measurement conditions.

Synthesis

1261 mg (6.0 mmol) of citric acid monohydrate (CAM) and 242 mg of Tris (2.0 mmol) were placed in a 50 ml round bottomed flask in their crystalline form and immersed into a preheated 180°C oil bath (100 rpm stirring rate was applied with a Teflon coated stirring bar). Reaction times were measured from the moment of complete melting of the precursor crystalline material. During the course of the reaction, the transparent liquid bubbled, foamed and slowly turned yellowish than light brown. Samples were taken at defined reaction times for analysis.

Functionalization of CPDs with APTES

The CAM/Tris-based CPDs (from 15-60 min reaction) were functionalized by addition of 0.33 mL APTES to 10 mL aqueous solutions with a concentration of 1 mg mL^{-1} of the CPDs and stirred at room temperature for 24 h at 500 rpm.[107]

4.2.3. Results and discussion

The purpose of using the different routes to synthesise C-dots is the control of the PL emission properties in terms of range and intensity. It is also important to correlate the optical response with the chemical species responsible for the emission even if this represents a very challenging task. Therefore, we have studied the products of the synthesis as a function of the reaction time, coupling different optical and spectroscopic techniques.

Figure 42.4a shows the UV-Vis absorption spectra of the CPDs after different reaction times, from 5 to 45 min. The spectra are characterized by two main absorption bands peaking at 338 nm and at 230 nm. They are assigned to n – π* and π – π * transitions, respectively.[130]

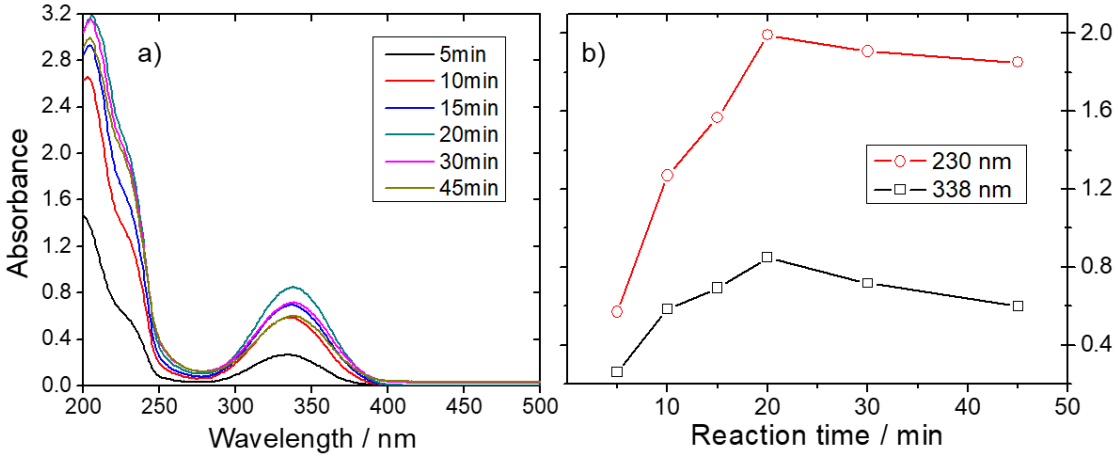

Figure 42.4. a) UV-Vis absorption spectra of CPDs at different reactions times. b) Change of the maximum in absorbance of the 230 and 338 nm bands. The concentration of CPDs in aqueous solution was 100 mg L^{-1}.

The absorbance of the two bands changes as the reaction proceeds (**figure 42.4b**); it increases up to 20 minutes, which appears to be a breakpoint of the process. At longer reaction times, up to 45 minutes, a 25% decrease in the absorbance is observed.

Transmission electron microscopy images show that during the synthesis of CPDs, a well-defined, spherically shaped particles formed. **Figure 42.5** is a representative image of round-shaped carbon nanoparticle with an average size of 8.4 ± 1.5 nm which formed upon the thermal degradation process at 180°C for 15 min. The size of the CPDs appears monodispersed in the 10 nm range, although larger impurities also formed during the synthesis (**figure 42.6**). DLS analysis further confirms the dimension of C-dots. Their hydrodynamic diameter is centering around or just below 10 nm from 5 to 20 minutes reaction time (**figure 42.7**). Shorter reaction time results an asymmetric distribution in favor of smaller particles as they are building up in the reaction, while after 10 minutes

it is symmetrically distributed. At 20 minutes, the size-distribution widens, indicating, that after maximum PL emission at 20 minutes, the system start to degrade.

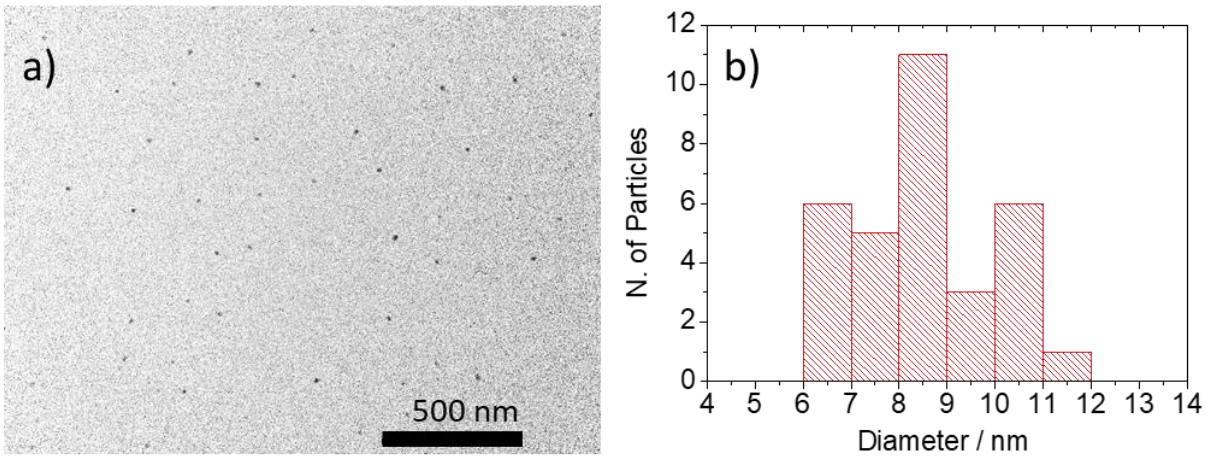

Figure 42.5. a) Representative TEM image of CPDs synthesized from CA/Tris after 15 minutes at 180°C. b) Distribution of CPDs size calculated from image a).

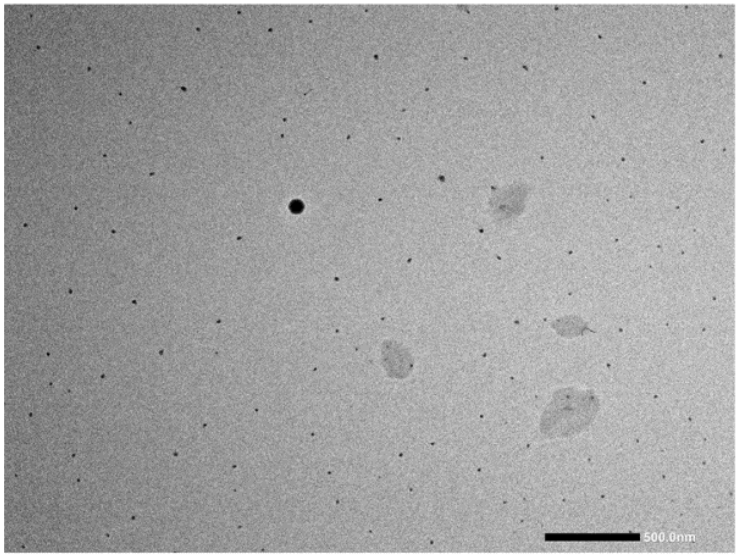

Figure 42.6. TEM image showing the presence of larger impurities among the monodisperse carbonized polymer dots (15 min)

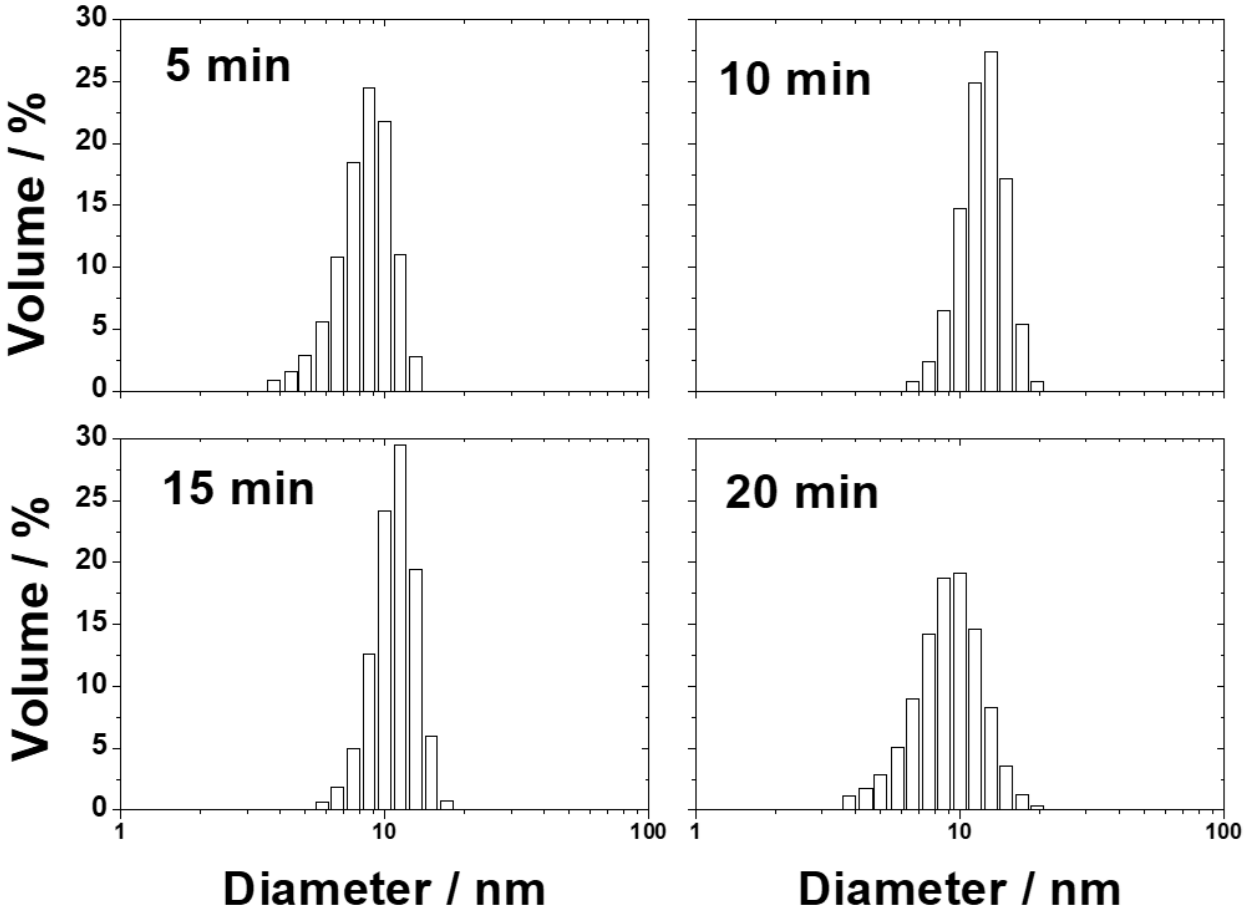

Figure 42.7. Particle size distribution of the C-dots (aq) at different reaction times, obtained by DLS method.

Figure 42.8. shows the 3D fluorescence spectra (excitation (y-scale), emission (x-scale), intensity (false colour scale)) of the samples after 5, 15 and 30 minutes of synthesis. The spectra exhibit an increase in the emission intensity in the first minutes of reaction, while after 30 minutes, the 3D-maps reveal a significant reduction of fluorescence intensity, which continues at higher reaction times. The emission band is asymmetric with a long tail extended up to around 500 nm, at the edge of the green region. The photoluminescence spectra follow a trend similar to the UV-Vis data (**figure 42.4**). Upon excitation at 330 nm, the CPDs show an intense emission peaking at 410 nm in the violet range. The fluorescence is excitation independent.

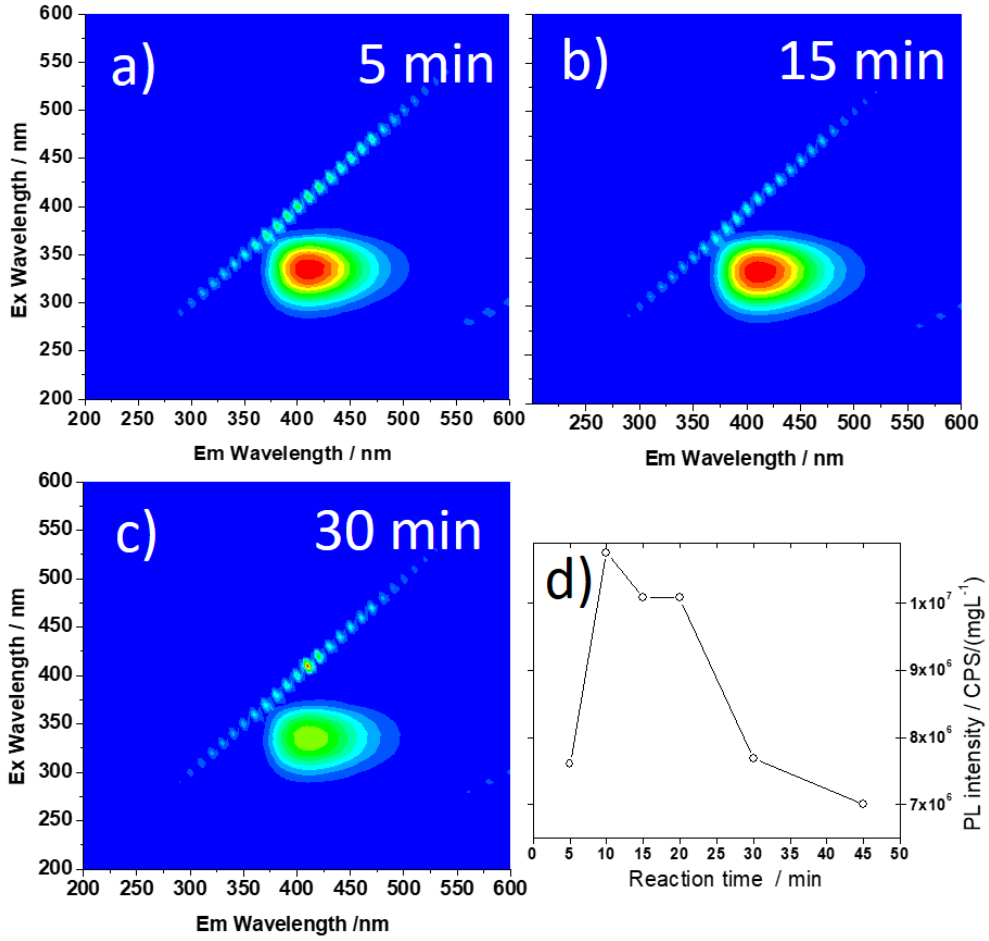

Figure 42.8. 3D fluorescence spectra (excitation (y-scale), emission (x-scale), intensity (false colour scale)) at 5 (a), 15 (b) and 30 minutes (c) of reaction time. d) Change in intensity of the emission maxima at 410 nm as a function of the reaction time. The line is a guide for eyes. The concentration of CPDs in aqueous solution was 1 mg L^{-1}.

FTIR absorption spectroscopy has been employed to investigate the change in the structure induced by the thermal treatment. **Figure 42.9a** shows the spectra in the 1850 - 1600 cm^{-1} region. The full spectra are reported in **figure 42.10c**. Two new absorption bands are detected in the product of CAM and Tris reaction. One band, peaking at 1733 cm^{-1}, is assigned to the stretching mode of C=O in esters (-C(=O)O-C-)[131] and the second one at 1668 cm^{-1} is attributed to C=O stretching in amides (-C(=O)NH-C-).[95,128] These bands are well preserved up to 60 minutes of reaction, showing an intensity increase in the first 20 minutes (**figure 42.9b**).

The FTIR spectra further confirm the formation of amides (**figure 42.10**), upon reaction between CA and Tris, which are characterized by other vibrational modes, N-H bending around 1550 cm^{-1} (**figure 42.10b**) and N-H stretching at high wavenumbers, around 3500 cm^{-1} (**figure 42.10a**). All the absorption bands follow a similar trend well supporting the attribution to the amide bond.[95,132]

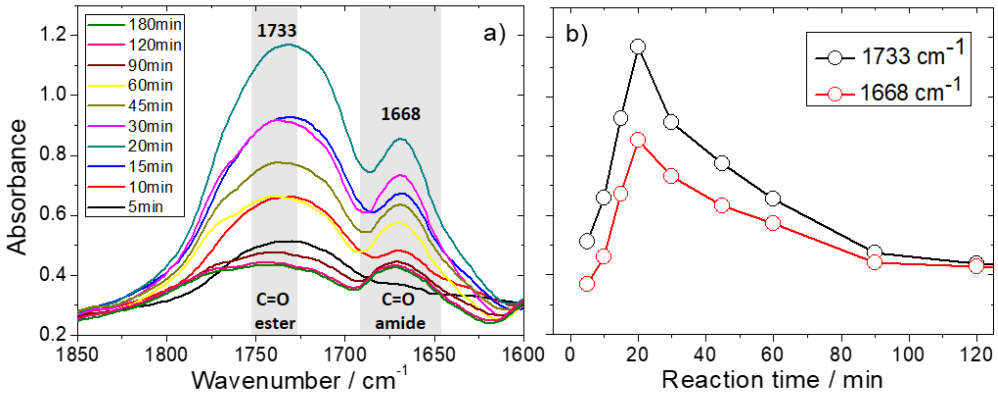

Figure 42.9. a) FTIR absorption spectra in the 1850 – 1600 cm^{-1} range as a function of the reaction times. b) Change of the 1733 (black line) and 1668 cm^{-1} (red line) absorbance intensities. The lines are a guide for eyes.

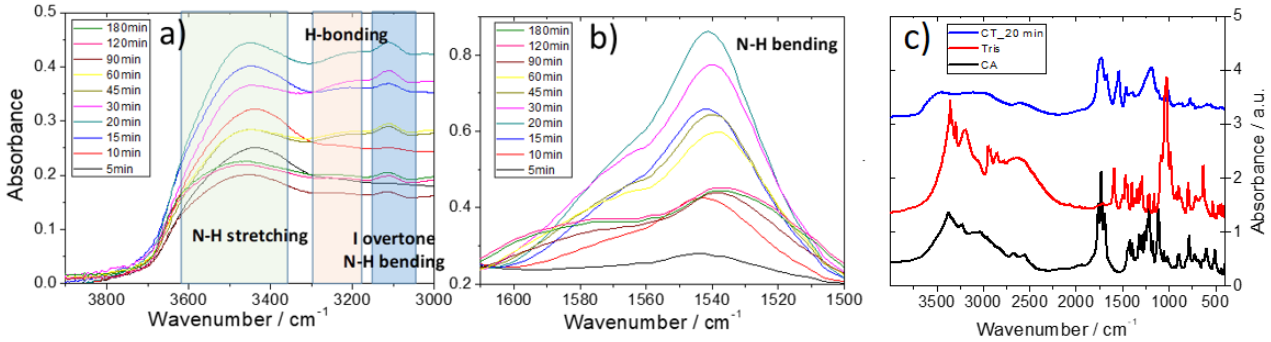

Figure 42.10. FTIR absorption spectra of the CPDs in the a) 3900 – 3000 cm^{-1} and b) 1650 – 1500 cm^{-1} range as a function of the reaction times. Full FTIR spectra of citric acid (CA), Tris and citric acid/Tris product after 20 minutes of reaction (c) in the range of 4000 – 400 cm^{-1}.

In the higher wavenumber region (**figure 42.10a),** besides intense N-H stretching[95] band around 3500 cm^{-1} and the overtone assigned to N-H bending at 3100 cm^{-1},[132] is characterized by the rise of an overlapped absorption band around 3200 cm^{-1}, which is assigned to the formation of H-bond of amides.[133] The band forms after 10 minutes of reaction and disappears after 60 minutes. The formation of H-bonds can be correlated with the formation of amides. The amides appear after 10 minutes, when also secondary bonds form. When the amide structures are degraded by thermal reaction, secondary bonds are no longer detected. The formation of esters follow a similar trend (**figure 42.9**) and the attribution is also supported by the disappearance of the Tris' C-OH, and detection of ester' C-OC signals at 1037 and 1186 cm^{-1}, respectively (full spectrum: **figure 42.10c**).[127,131]

These trends are well in agreement with the photoluminescence spectra (**figure 42.8**), whose emission intensity displays a maximum around the same reaction time. Therefore, a direct correlation

between the formation of polymeric species containing amide and ester bonds, and the photoluminescence properties can be established.

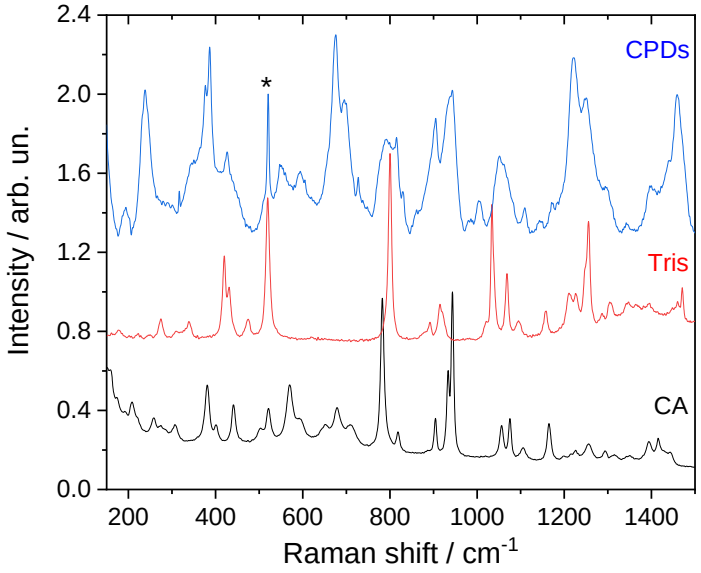

Figure 42.11. Raman spectra of citric acid (black curve), Tris (red curve) and the CPDs (blue curve). The reported CPDs Raman spectrum corresponds to the sample after 5 minutes of reaction.*The vibrational mode at about 521 cm^{-1} corresponds to Si substrate.

Figure 42.11 shows the Raman spectra of citric acid, Tris and CPDs (after 5 minutes of reaction) in the range of 150-1500 cm^{-1}. Citric acid presents two characteristic vibrational modes at 783 cm^{-1} and 943 cm^{-1}. The first is attributed to C-C stretching and OH bending in carboxylic groups and the second corresponds to -C-C-C- bending and OH bending. The modes at lower wavenumbers originate from the twisting and rocking of CH_2 group (570 cm^{-1}) and the rocking of -COOH group (380 cm^{-1}).[108]

Tris displays two main bands at about 800 cm^{-1} and 520 cm^{-1} due to C-C stretching and C-C(N)-C bending, respectively. Moreover, the C-NH_2 bending is detectable at 419 cm^{-1}. The main vibrations at 1034 cm^{-1} and 1254 cm^{-1} are attributed to NH_2 twisting and OH bending, respectively.[134]

The thermal treatment of citric acid and Tris mixture promotes the formation of new bands and a reinforcement of the characteristic precursor's vibrations. A new mode arises at 240 cm^{-1}, only a few minutes after melting. Low wavenumbers modes (< 300 cm^{-1}) are tentatively assigned to skeletal motions of long -C-C- chains arising from the condensation of citric acid and Tris.[135,136] Furthermore, the strong vibration at 1223 cm^{-1} is assigned to amide groups.[137] It is worth to underline that further vibrational fingerprints of amide group in Raman spectra are in the region between 1550 and 1650 cm^{-1}, not accessible in our experimental conditions.

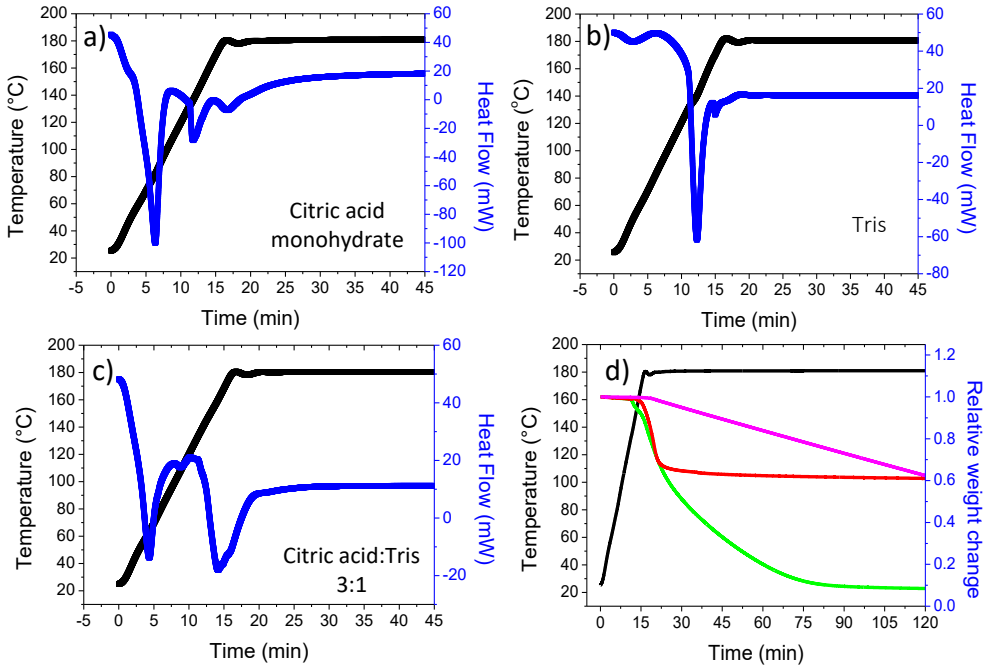

Figure 42.12. Calorimetric analysis of samples at the reaction temperature (180°C, black line): (a) citric acid monohydrate; (b) Tris; (c) citric acid:Tris (n:n) 3:1. d) Relative weight change under synthesis conditions (TGA): citric acid (green), Tris (magenta) and citric acid:Tris (n:n) 3:1 (red).

The DSC results of the reference samples**:** citric acid monohydrate, Tris, and the combination of CAM and Tris and their relative weight changes at 180ºC (our reaction temperature) have been analyzed (**figure 42.12**). The endothermic events of melting of CAM (m.p. 135ºC, Fluka) and Tris (m.p. 167-172ºC, Carlo Erba) appeared on the DSC curves (**figure 42.12a-b**). Weight change (**figure 42.12d**) was not observed under ~140ºC (for CAM), ~160ºC (for CAM/Tris mixture) and ~180ºC (for Tris) indicating that there was no reaction resulting elimination of materials (H_2O or CO_2 due to dehydration, condensation or decarboxylation) and every DSC signals under these values should be assigned to morphological changes. While afterwards, all the samples suffered significant weight loss. Tris alone shows a monotonous loss of weight probably due to a slow dehydration process and also CAM undergoes an intensive weight loss in the first 75 minutes of the reaction (see chapter 4.1) through dehydration and decarboxylation steps, starting at the temperature of 160 ºC, while the reaction mixture mainly suffers weight loss in the first 10 minutes after reaching the 180ºC reaction temperature and forms a thermally more stable material (**figure 42.12d**), however, a slow decomposition can be still detected afterwards. The intense weight loss is due to the condensation process of the precursors, forming a polymeric structure, while water (and probably some CO_2 from the decomposition of CAM) eliminates from the system. The end of the intense weight loss also well correlates to the maximum PL-intensity observed at 10-15 minutes reaction time (**figure 42.8d**).

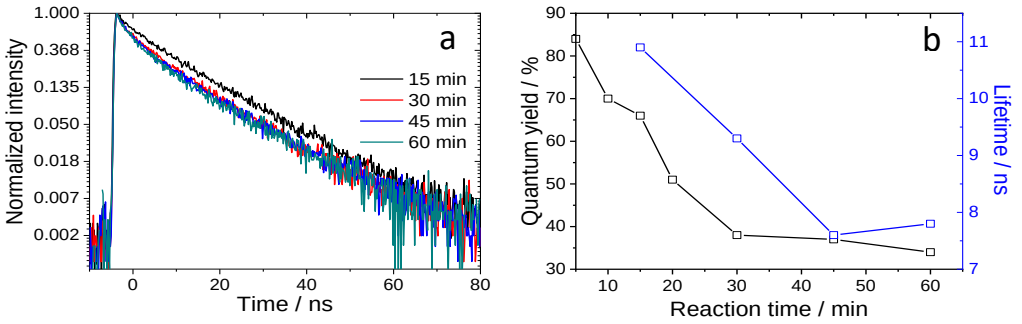

Figure 42.13. a) PL decay curves of the samples reacted for 15, 30, 45 and 60 minutes. b) Quantum yields and lifetimes calculated at the different reaction times. The lines are only guide for the eyes.

The fluorescence lifetime of the samples after different reaction times and the corresponding QY are shown in **figure 42.13**. The decay profile of photoluminescence was analyzed by a two-exponential law and the average lifetime is calculated as:

$$\tau^* = (I_1\tau_1^2 + I_2\tau_2^2)/(I_1\tau_1 + I_2\tau_2)$$

After the first five minutes of reaction, the QY exceeds 80%, and an average lifetime of 11 ns is measured. With the proceed of the reaction, both the values decrease. In particular, the QY drops from 84 to 38% after 30 minutes of reaction; in agreement with the PL intensity (**figure 42.8d**). After 45 minutes, τ* falls below 8 ns. This trend is in good accordance with the efficiency loss, which is most likely due to the progressive degradation of the system with the reaction time.

The reaction time is, therefore, a very critical parameter, which controls the emission properties. The FTIR and Raman spectra well agree with the optical data to point out that at the first stage a fluorescent polymeric species is formed. The copolymerization reaction of the precursors involves the formation of amide and ester bonds as shown in **figure 42.14**. When the fluorescent polymers are thermally degrading due to the pyrolysis, a significant decrease in the emission is observed.

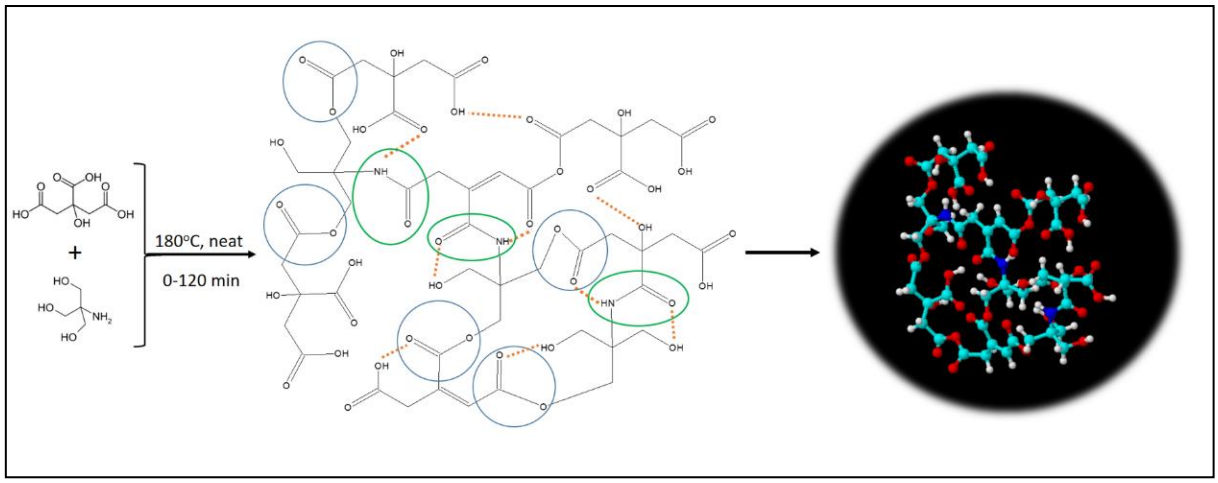

Figure 42.14. Formation of CPDs by reaction of CA and Tris. The green and blue circles show the amide and ester bonds, respectively. Possible intramolecular H-bonds indicated by orange dotted lines.

Surface modification by APTES

In parallel with the citric acid based C-dots, where we found that post functionalization with APTES greatly influence the PL properties (chapter 4.1), we also examined, but less detailed, the CAM/Tris 3/1 based CPDs under the same reaction conditions (1 mg mL^{-1} aqueous CPDs were mixed with 0.33 mL of APTES and stirred for 24h at ambient temperature). We selected the samples obtained from the 15, 30, 45 and 60 minutes reactions due to their sufficient solubility for preparation of 1 mg mL^{-1} aqueous solutions prior to addition of APTES. Examination of the obtained PL emission spectra upon excitation at the optimal 340 nm wavelength (**figure 42.15)** revealed that the emission maximum did not shift, in contrast to the citric acid C-dots' emission (chapter 4.1), while great enhancement in intensity were observed (**figure 42.15 and 14.16)**. PL originating from APTES was excluded, since it was stirred without any additional CPDs in water (as reference) under the same reaction conditions and resulted only negligible fluorescence, peaking at 440 nm upon excitation by 350 nm light. The observed emission is at least 10^6 times weaker than the fluorescence coming from the analyzed CPDs.

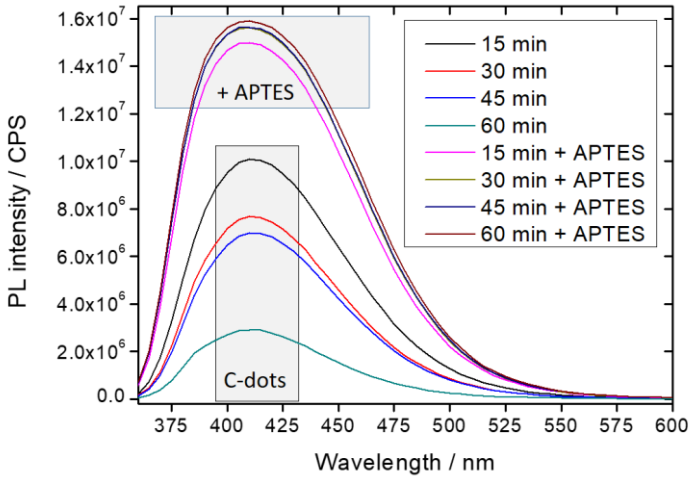

Figure 42.15 shows the obtained PL emission spectra of the CAM/Tris 3/1 based CPDs at different reaction times and the spectra of their APTES functionalized derivatives. All samples measured at 1 mg L^{-1} (aq). The concentration was calculated only by the weight of CPDs (without the APTES).

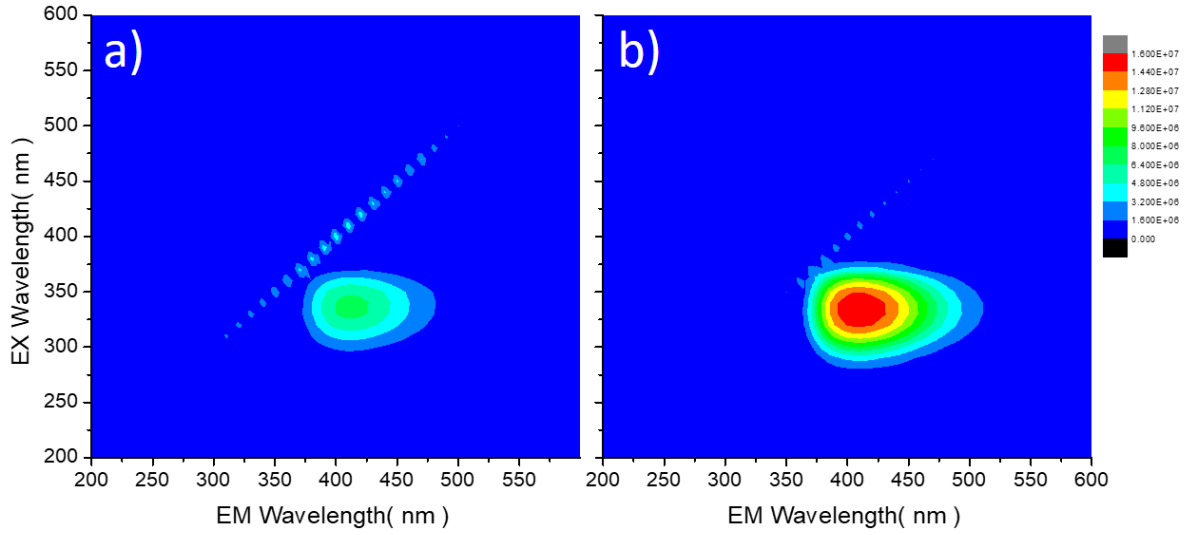

Figure 42.16. 3D fluorescence spectra (excitation (y-scale), emission (x-scale), intensity (false colour scale)) of CAM/Tris 3/1 CPDs obtained after 45 minutes reaction time (a) and its APTES functionalized derivative. The same colour scaling and the concentration of 1 mgL^{-1} (for CPDs) were applied for both samples.

Particularly interesting, that despite of the different emission intensities of the CPDs, their modified derivatives all exhibited a similarly powerful luminescence. The emission was so intense that it might have caused (near) saturation in the light detection device (while every measurement settings were identical to the CPDs' conditions), and therefore might have caused less differentiated results among APTES modified specimens.

Further studies were conducted by using UV-Vis spectrometry. Even though the most interesting sample is the functionalized CPDs from the 60 minutes reaction, for its five fold

enhancement factor in PL, we selected the CPDs from the 45 minutes reaction for comparison, due to the still sufficient solubility in water (**figure 42.17**).

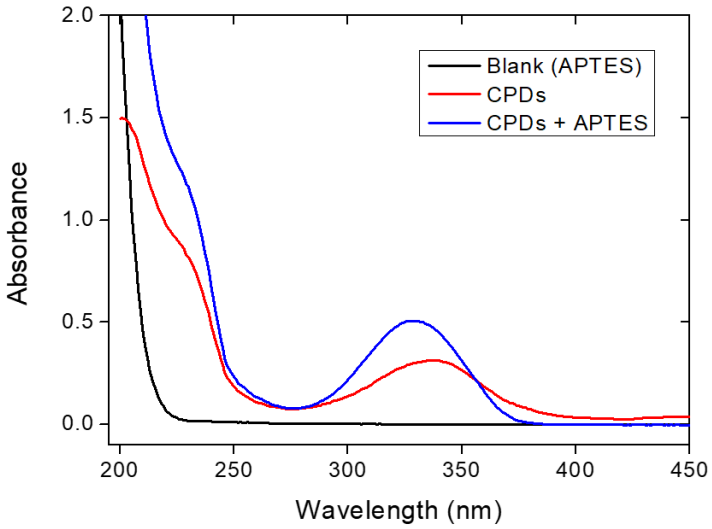

Figure 42.17. UV-Vis spectra of CPDs (45 min) and CPDs/APTES mixture compared to the spectra of APTES. All samples measured after the same dilution (10x) from their reaction mixtures/solution and stirred for 24h prior to measurement.

The UV-Vis absorption spectra revealed a 10 nm blue shift and an increase in the absorbance maximum in the 325-340 nm range, which region is associated to the n-π* transition.[130] As this absorption range is strictly connected to the observed PL emission intensity (**figures 42.4 and 42.8**) in the examined CPDs, we further established that this link also applies to their functionalized derivatives, however the connection is not linear anymore: 60% increase of the UV-absorption and 120% growth in the PL were observed by samples of 45 min CPDs.

The collected data of APTES modified CPDs in the present paragraph and in chapter 4.1. let us assume, that formation of silica shell around the carbon derived particles plays an important role in enhancement of fluorescence and similarly causes blue shift, although at a different degree, in the absorbance and the PL emission. The possible effect of the additional amino functional groups cannot excluded too and further studies needed to clarify the whole mechanism.

4.2.4. Effects of the precursor ratio

CA/Tris 3/1 molar ratio was selected as model system in this chapter based on the optimal properties of the synthesized C-dots found in chapter 3. Although the product exhibited intense PL emission, additional reactions were conducted under the same reaction conditions (solvent free, 180°C), but varying the molar ratio of the precursors. Samples were taken at different reaction times and the obtained PL and UV-Vis data are reported in the following tables and figures.

a) Precursor: only Tris

Tris gives only very weak and random PL in the aspect of intensity through the reaction, while the weak emission always centers at 415-420 nm (**table 42.1**), which are 10-15 nm higher than CAM/Tris C-dots emission. Based on their UV spectra (**figure 42.18**), Tris apparently resists to thermal treatment: all the reacted samples show low and identical UV absorption, which can be explained with a moderate and reversible dehydration process. Therefore, the reaction samples may be considered as "concentrated Tris" which can rehydrate as dissolved in water. The obtained products also does not show any color change as an indication of carbonization (**figure 42.17**). This result is partially in accordance with the TGA data (**figure 42.12d**), which plots a continuous, but moderate weight loss during the thermal treatment and can be interpreted as the aforementioned slow dehydration, but since weight change observed through the whole reaction, therefore Tris should gradually "concentrate" and should give increasing UV absorption. Thus another, yet unidentified process(es) should also be involved, which does not generate additional UV absorbance, but gives rise of weak (and random) PL. The apparent thermal stability of Tris makes it an inadequate precursor for synthesis of C-dots under our reaction conditions.

	Heating/T	Max. excitation / Max. emission (nm)	Max. intensity (CPS/(mg/L))
15min	oil, 180°C	340/420 (100mg/L)	1444
30min	oil, 180°C	340/420 (100mg/L)	18519
45min	oil, 180°C	340/420 (100mg/L)	6185
60min	oil, 180°C	340/415 (100mg/L)	1002
90min	oil, 180°C	320/415 (100mg/L)	915
120min	oil, 180°C	340/415 (100mg/L)	18676
180min	oil, 180°C	340/415 (100mg/L)	4359

Table 42.1. Maximum excitation / maximum emission wavelengths in nm's and the obtained PL-emission intensities calculated for 1 mgL^{-1} concentration of pyrolysed Tris. Measured at different reaction times at 100 mgL^{-1} (aq) concentration.

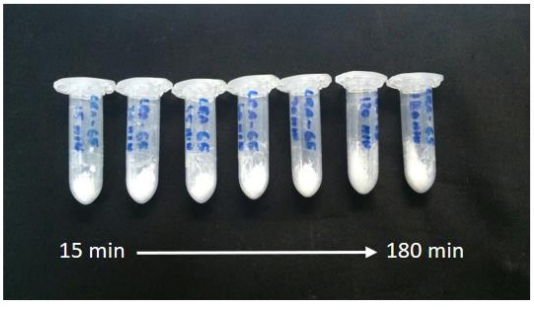

Figure 42.17. Appearance of the samples from 15 to 180 min reaction of Tris.

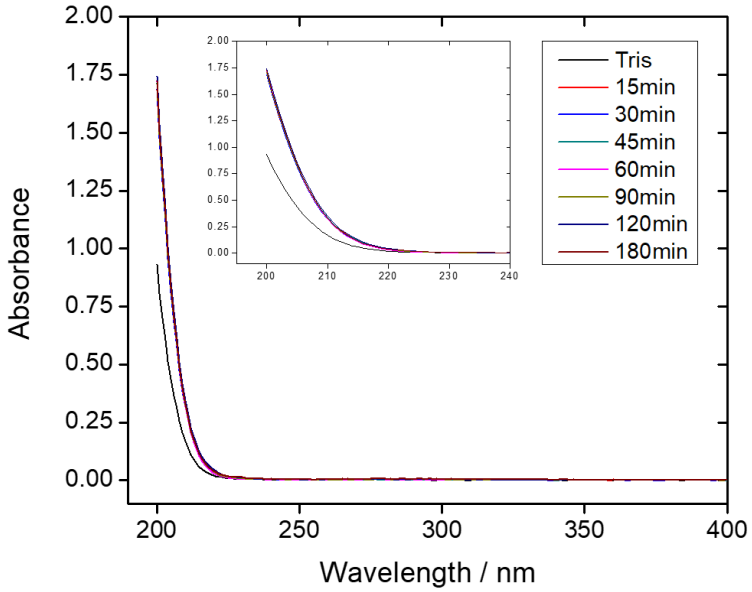

Figure 42.18. UV-Vis spectrum of Tris-based products at different reaction times, plotted from 200 to 400 nm and 200-240 nm (inner box). Samples measured at 500 mgL^{-1} (aq) and all reacted materials exhibit slightly increased and identical UV spectra, in contrast to the UV absorption of Tris.

b) Precursor: CAM / Tris 1/1

Reacting Tris and CAM in 1/1 ratio under our reaction conditions results at least 575x increase in PL intensity compared to the only Tris-based products, and minimum 470x growth compared to CAM-based C-dots (**table 42.1 and table 41.1**) in very short reaction times (10-15 min). It must be noted that due to different formation mechanisms and fluorophores, the emission wavelengths differ. Although this mixture gives very intense PL response in the same violet range (**table 42.2** and **figure 42.20a**) as our well examined CAM / Tris 3/1 sample (**figure 42.8abc**), its water solubility falls below 100 mgL^{-1} after only 10 minutes, and under 1 mgL^{-1} after 20 minutes of reaction (**table 42.2**), which makes impossible to further analyze by our spectrometers in aqueous solutions. This finding also supports this chapter's main idea of formation of polymeric dots in the reaction of CAM and Tris. We observed, that moderately increasing the ratio of CAM in the reaction mixture, while does not corrupt significantly the final PL intensity, gradually increases the products water solubility as leaves space for unreacted hydrophilic –OH and –COOH groups after the polymerization reaction. The color of the product turns dark even in short (10 minutes) reaction time (**figure 42.19**).

	Heating/T	Max. excitation / Max. emission (nm)	Max. intensity (CPS/(mg/L))	Absorbance at 333nm
5min	oil, 180°C	330/410 (1mg/L)	7771000	0.204
10min	oil, 180°C	340/410 (1mg/L)	10246000	0.479
15min	oil, 180°C	340/410 (1mg/L)	10774000	n.a.
20min	oil, 180°C	340/415 (1mg/L)	10378000	n.a.
30min	oil, 180°C	solubility: < 1mg/L	n.a.	n.a.
45min	oil, 180°C	solubility: < 1mg/L	n.a.	n.a.
60min	oil, 180°C	solubility: < 1mg/L	n.a.	n.a.
90min	oil, 180°C	solubility: < 1mg/L	n.a.	n.a.
120min	oil, 180°C	solubility: < 1mg/L	n.a.	n.a.
180min	oil, 180°C	solubility: < 1mg/L	n.a.	n.a.

Table 42.2. Maximum excitation / maximum emission wavelengths in nm's and the obtained PL-emission intensities at 1 mgL^{-1} (aq) concentration and characteristic UV-absorbance at 333nm of CAM/Tris 1/1 samples measured at different reaction times at 100 mgL^{-1} (aq) concentration.

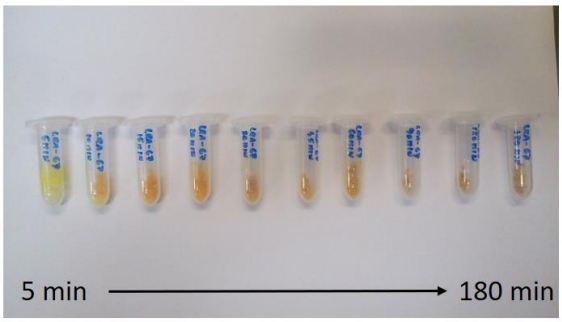

Figure 42.19. Appearance of the CAM/Tris 1/1 samples from 5 to 180 min reaction time.

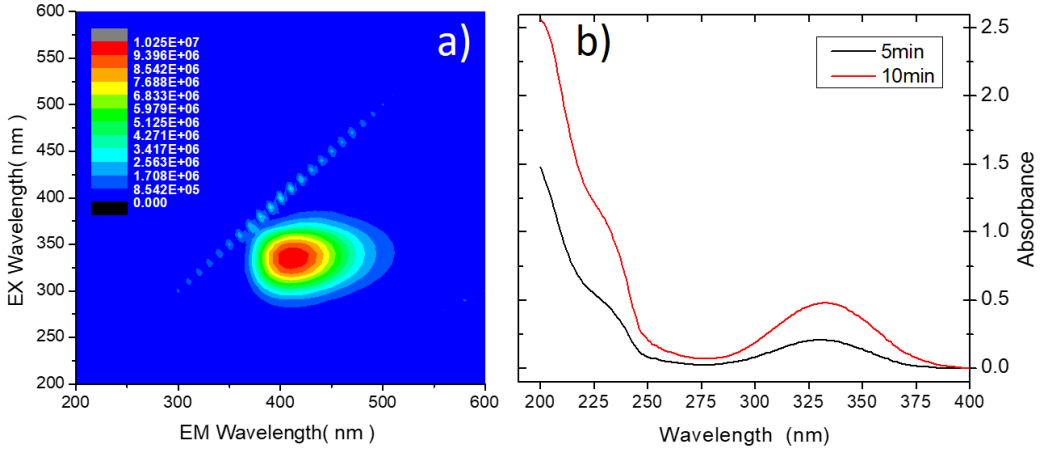

Figure 42.20. a) shows the 3D fluorescence spectra (excitation (y-scale), emission (x-scale), intensity (false colour scale)) at 10 minutes reaction time (1 mgL^{-1} aq) and b) the UV-Vis spectra of the samples obtained after 5 and 10 minutes of the reaction of CAM / Tris 1/1 (100 mgL^{-1} aq). The other samples were not measured due to their poor solubility.

c) Precursor: CAM / Tris 3/1

This composition is well analyzed and relevant data can be found in the present chapter: **figure 42.4** (UV-Vis) and **figure 42.8** (PL). This ratio of precursors allows the formation of products with good water solubility of >100 mgL^{-1} up to 45 minutes and >1 mgL^{-1} until 90 minutes reaction, while the product's color turns darker only at around 60 minutes (**figure 42.21**) in contrast to the observed 10 minutes in the case of CAM / Tris 1/1.

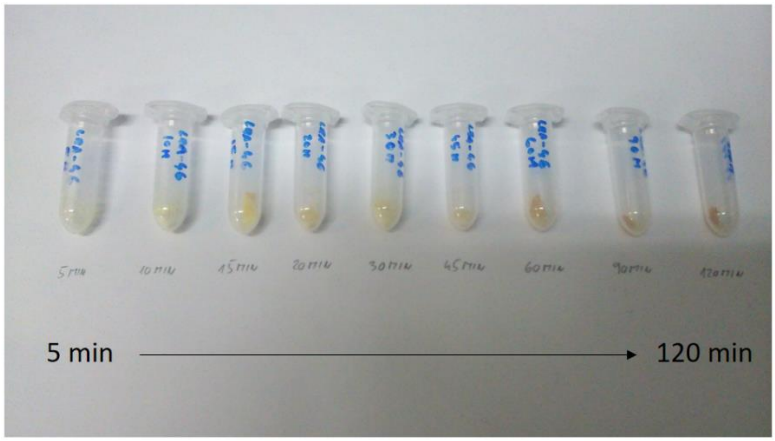

Figure 42.21. Appearance of the CAM / Tris 3/1 derived samples from 5 to 120 min reaction time.

d) Precursor: CAM / Tris 5/1

The obtained products' UV absorption at 338 nm and PL emission intensity trends (**table 42.3** and **figure 42.23ab)** at 410 nm are in good correlation, while PL intensity remains as high as in the case of CAM / Tris 3/1. The water solubility is >100 mgL^{-1} up to 60 minutes and >1 mgL^{-1} until at least 180 minutes reaction time (**table 42.3**). Color change of the crude product can be observed on **figure 42.22.**

	Heating/T	Max. excitation / Max. emission (nm)	Max. intensity (CPS/(mg/L))	Absorbance at 338nm
5min	oil, 180°C	330/410 (1mg/L)	6272000	0.183
10min	oil, 180°C	340/410 (1mg/L)	9300000	0.468
15min	oil, 180°C	340/410 (1mg/L)	10128000	0.561
20min	oil, 180°C	340/410 (1mg/L)	9505000	0.600
30min	oil, 180°C	340/410 (1mg/L)	10071000	0.704
45min	oil, 180°C	340/415 (1mg/L)	7795000	0.852
60min	oil, 180°C	340/410 (1mg/L)	4824000	0.617
90min	oil, 180°C	340/410 (1mg/L)	2731000	n.a.
120min	oil, 180°C	340/410 (1mg/L)	4380000	n.a.
180min	oil, 180°C	340/410 (1mg/L)	777000	n.a.

Table 42.3. Maximum excitation / maximum emission wavelengths in nm's and the obtained PL-emission intensities at 1 mgL^{-1} (aq) concentration and characteristic UV-absorbance at 338 nm of CAM/Tris 5/1 samples measured at different reaction times at 100 mgL^{-1} (aq) concentration.

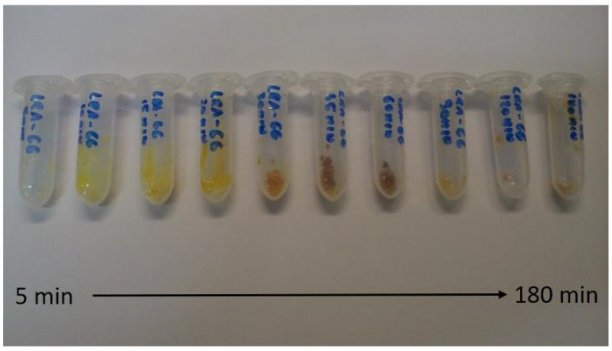

Figure 42.22. Appearance of the CAM/Tris 5/1 samples from 5 to 180 min reaction time.

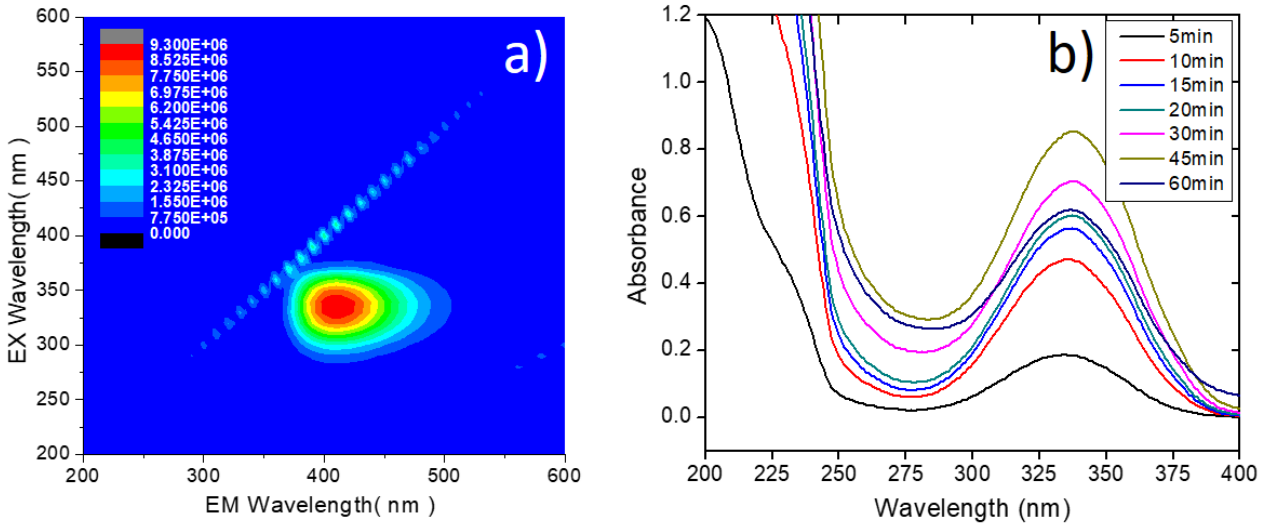

Figure 42.23. a) 3D fluorescence spectra (excitation (y-scale), emission (x-scale), intensity (false colour scale)) at 10 minutes reaction time (1 mgL^{-1} aq) and b) the UV-Vis spectra of the samples obtained after 5 to 60 minutes of the reaction of CAM / Tris 5/1 (100 mgL^{-1})

e) Precursor: CAM / Tris 10/1

Our most CAM-rich mixture (**figure 42.24**) exhibits excellent water solubility through the reaction, in accordance with our previous findings of increasing solvability of such materials as initial CAM ratio increases (**table 42.4**). The observed PL emission intensity falls by 35% compared to the best result from CAM/Tris 3/1 samples as the number of intra- and intermolecular interactions and the number of formed fluorophores decreases, while the intensity peak remains at 410 nm and in the range of 10-20 minutes reaction time (**figure 42.25**).

	Heating/T	Max. excitation / Max. emission (nm)	Max. intensity (CPS/(mg/L))	Absorbance at 337nm
5min	oil, 180°C	330/410 (1mg/L)	2062000	0.046
10min	oil, 180°C	340/410 (1mg/L)	6203000	0.187
15min	oil, 180°C	340/410 (1mg/L)	6365000	0.247
20min	oil, 180°C	340/410 (1mg/L)	6812000	0.286
30min	oil, 180°C	340/410 (1mg/L)	6287000	0.329
45min	oil, 180°C	340/420 (1mg/L)	4997000	0.517
60min	oil, 180°C	340/415 (1mg/L)	4812000	0.547
90min	oil, 180°C	340/415 (1mg/L)	5403000	0.692
120min	oil, 180°C	340/415 (1mg/L)	4343000	0.299
180min	oil, 180°C	340/410 (1mg/L)	5367000	n.a.

Table 42.4. Maximum excitation / maximum emission wavelengths in nm's and the obtained PL-emission intensities at 1 mgL^{-1} (aq) concentration and characteristic UV-absorbance at 337nm of CAM/Tris 10/1 samples measured at different reaction times at 100 mgL^{-1} (aq) concentration.

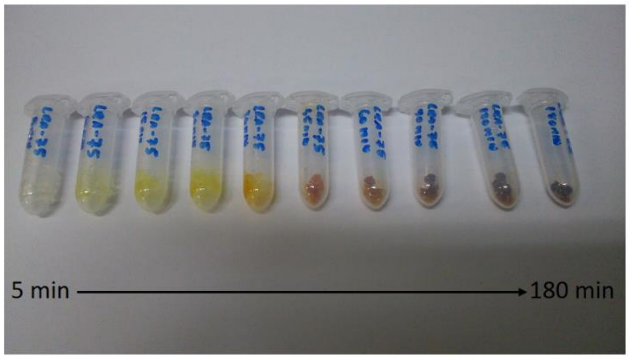

Figure 42.24. Appearance of the CAM/Tris 10/1 samples from 5 to 180 min reaction time.

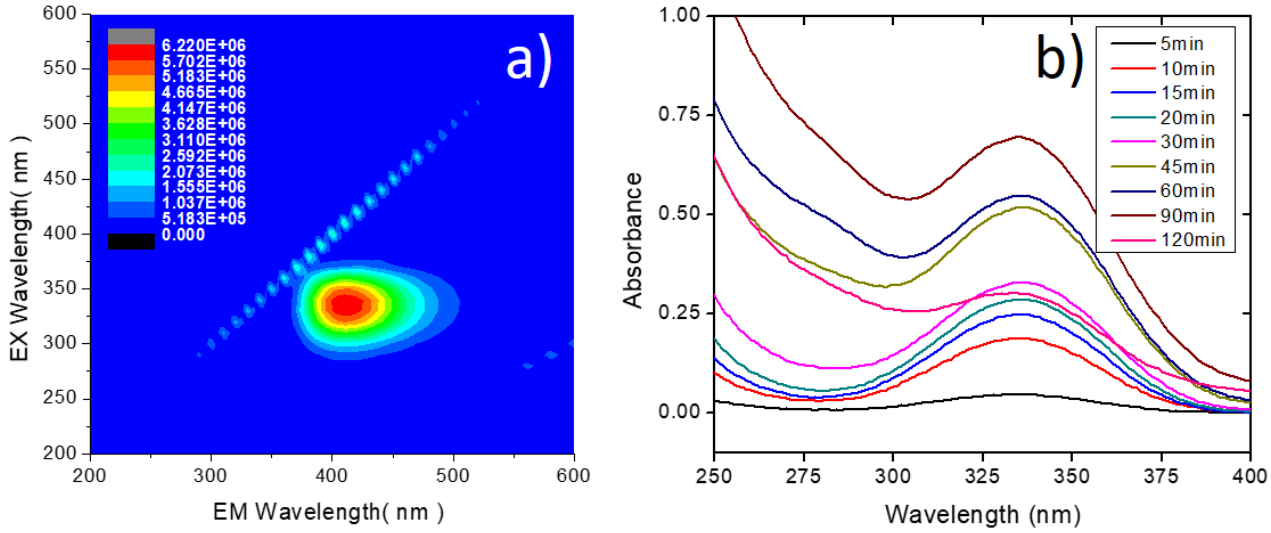

Figure 42.25. a) 3D fluorescence spectra (excitation (y-scale), emission (x-scale), intensity (false colour scale)) at 10 minutes reaction time (1 mgL^{-1} aq) and b) the UV-Vis spectra of the samples obtained after 5 to 120 minutes of the reaction of CAM / Tris 10/1 (100 mgL^{-1}aq)

f) Precursor: only CAM

This precursor is also well analyzed and relevant data can be found in chapter 4.1: **figure 41.12** (UV-Vis) and **figure 41.13** (PL). The products exhibit a good water solubility up to 120 minutes of reaction, while continuously growing but weak PL is observed, revealing a very different mechanism of fluorophore centers in the absence of Tris.

After comparing the standardized PL emission intensities of the various CAM/Tris based samples at 410 nm, we can observe that varying the initial molar ratio of the precursors by increasing amount of the CAM, we can influence the emission properties, especially the intensity through the reaction. CAM/Tris 1/1 - 3/1 - 5/1 samples exhibit similar highly intense PL, but as more CAM is present, the decomposition rate of the fluorophores decreases, therefore a thermally more stable material forms, which can be advantageous in numerous applications. The CAM/Tris 10/1 reaction mixture gives the thermally most stable, but less fluorescent products, as its maximum PL intensity is only 2/3 of the other mixtures' while remains almost constant up to 120 minutes reaction time (**figure 42.26**).

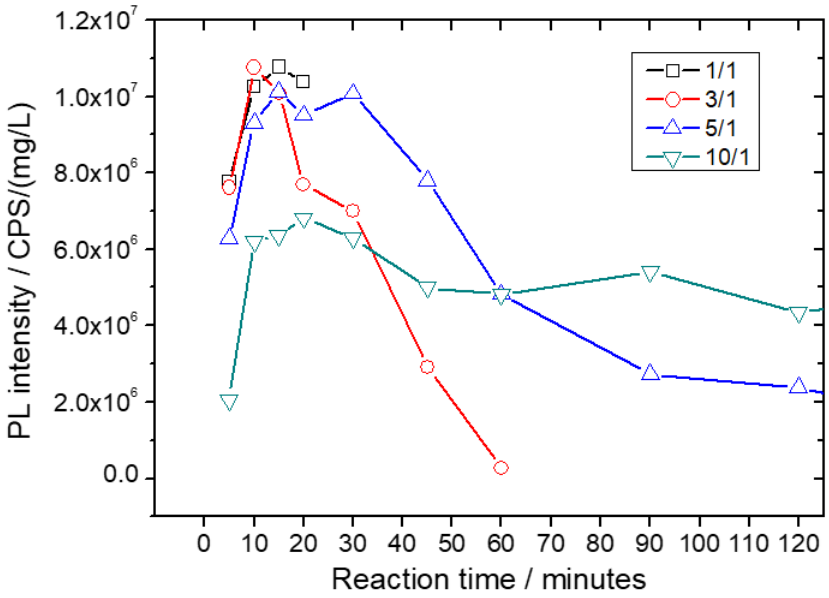

Figure 42.26. Comparison of PL intensities through the reaction of CAM and Tris at different reaction times and ratios: 1/1 (black square), 3/1 (red circle), 5/1 (blue triangle) and 10/1 (green triangle). Samples measured at 1 mgL^{-1} (aq) concentration.

4.2.5. Conclusions

Thermal reaction of citric acid and 2-amino-2-(hydroxymethyl)propane-1,3-diol, as reported earlier, produces highly fluorescent materials, but the formation mechanism was not thoroughly investigated. Under our pyrolysis synthetic approach, the obtained particles have been identified as spherical and monodispersed CPDs with an average dimension of 10 nm. The reaction time at 180°C was found to be a crucial parameter, as we monitored the reaction progress up to 1h. Highly fluorescent CPDs, with a QY as high as 80%, have been obtained using a very short reaction times. The formation of polymeric species with amide and ester bonds is correlated with the fluorescence response. These compounds are sensitive to the synthesis conditions and at longer reaction times, when they are degraded, a decrease in their emission intensity is observed. Experimental data well agree that the formation of fluorescent polymeric species are responsible of the C-dots photoluminescence, which can be further enhanced by surface functionalization with APTES. The effect of precursors' ratio was also investigated and revealed that thermally more stable and water soluble products can be obtained by increasing the CAM/Tris ratio in the reaction. These findings can help to optimize the obtained C-dots properties for future applications, while functionalization with APTES gives a way to obtain even more fluorescent species with a view to embed them in silica matrices.

4.3. Citric acid – urea based carbon dots

Parts of this chapter were published in, or related to the following articles: [119,138]

Carbonaro C.M, Thakkar SV, **Ludmerczki R**, Olla C, Pinna A, Loche D, Malfatti L, Marincola F.C, Casula MF, How porosity affects the emission of fluorescent carbon dot-silica porous composites, *Microporous and Mesoporous Materials,* **2020**, 305, *110302*
DOI: 10.1016/j.micromeso.2020.110302

Mura S, **Ludmerczki R**, Stagi L, Garroni S, Carbonaro C.M, Ricci P.C, Casula M.F, Malfatti L, Innocenzi P, Integrating sol-gel and carbon dots chemistry for the fabrication of fluorescent hybrid organic-inorganic films, *Scientific Reports*, **2020**, 10, *4770*
DOI: 10.1038/s41598-020-61517-x

4.3.1. Introduction

To further study the family of citric acid based C-dots and to cover another part of the visible range with our synthesized C-dots (chapters 4.1 – 4.2 – 5.1), we adapted a reported method[139] of reacting citric acid and urea (**figure 43.1**) in our solvent free reaction approach and equipment. As citric acid usually give highly fluorescent C-dots with nitrogen-containing precursors[17,125] (chapter 4.2), typically in the blue range, it was highly unexpected, that the obtained C-dots from the citric acid-urea[140] (CU) reaction, reportedly exhibited a unique excitation dependent dual PL emission at 450 nm (blue) and 520 nm (green). The variation of precursor ratios also revealed, that using more urea results more dominant green PL, on the cost of decreasing partition of the blue. It was theorized, that the well-known citrazinic acid, a blue light emitting fluorophore, forms during the reaction of citric acid and urea, and it was responsible for the emission at 450 nm. Furthermore, it was later found, that the green emission cannot be observed if the reaction is performed in water.[91]

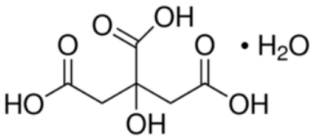

citric acid monohydrate (CAM),
2-hydroxypropane-1,2,3-tricarboxylic acid;hydrate
CAS: 5949-29-1
M_r: 210.14
mp: 135°C
decompose: >175°C

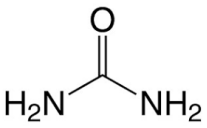

urea
CAS: 57-13-6
M_r: 60.06
mp: 133-135°C

Figure 43.1. Structure and properties of citric acid monohydrate and urea

Further tests revealed that citrazinic acid alone or in combination with ammonia did not result green emission, but on the contrary a bright green PL was observed if citrazinic acid reacted under solvent free conditions with urea.[139] The researchers could not give a fully satisfying explanation for the source of the green PL, therefore we set up a series of experiments to further investigate the C-dots formation and the source(s) of the green emission.

During our investigations, a Polish research group gave an elegant explanation for the phenomena, and reported the missing fluorophore: 4-hydroxy-1H-pyrrolo[3,4-c]pyridine-1,3,6(2H,5H)-trione (HPPT, **figure 43.2**)[91]. A reaction pathway was also proposed for the formation of HPPT: citrazinic acid reacts with the ammonia and isocyanic acid (H-N=C=O) released during the thermal decomposition of urea.[91,141] Our findings also support this explanation.

These C-dots, as all of our synthesized particles were subjected to surface functionalization with an organosilane (APTES) to integrate them into sol-gel systems.[119] The synthesized C-dots were also embedded in xero-, cryo- and aerogels.[138] (These applications are not part of this thesis.)

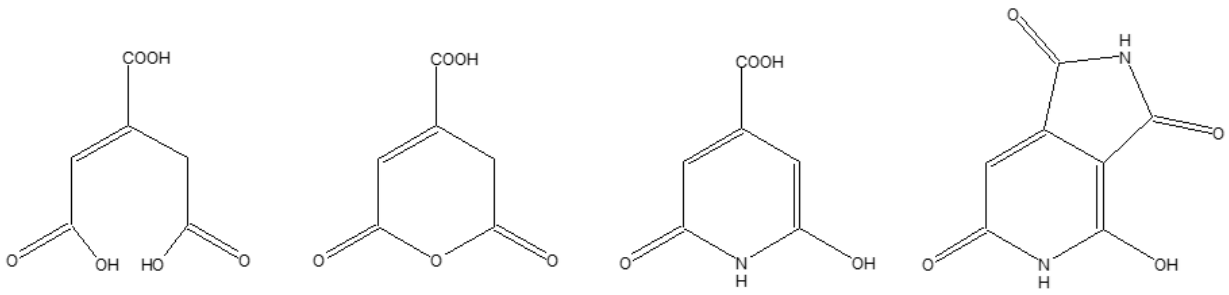

trans-aconitic acid *trans*-aconitic anhydride citrazinic acid HPPT

Figure 43.2. Structures of *trans*-aconitic acid and anhydride, citrazinic acid and HPPT.

The core structure of citrazinic acid and HPPT are very similar to the *trans*-aconitic acid and its anhydride (**figure 43.2**), which are molecular fluorophores in the citric acid based C-dots (chapter 4.1), therefore we suspect that the key intermediate in the formation of both the CA C-dots and the CU C-dots are these components, however, it is still subject of future experiments.

4.3.2. Experimental

Chemicals and reagents

Citric acid monohydrate (CAM)	Fluka, >99.5%
Urea	Aldrich, 98%
Citrazinic acid	Aldrich, 97%
3-(aminopropyl)triethoxysilane (APTES)	Aldrich, 99%
FTIR grade potassium bromide	Aldrich >99%

All chemicals were utilized without further purification.

In-site produced Milli-Q water was used for the analysis.

Synthesis

350 mg (1.67 mmol) of citric acid monohydrate (CAM) and 50 mg (for CU 2/1) or 100 mg (for CU 1/1) or 200 mg (for CU 1/2) or 300 mg (for CU 1/3) or 800 mg (for CU 1/8) urea were placed in a 50 ml round bottomed flask in their crystalline form and immersed into a preheated 180°C oil bath (100 rpm stirring rate was applied with a Teflon coated stirring bar). Reaction times were measured from the moment of complete melting of the precursor crystalline material. During the course of the reaction, the transparent liquid bubbled, and turned brown typically in less than 10 minutes. Samples were taken at 15-30-45-60 minutes reaction times (**figure 43.3.**)

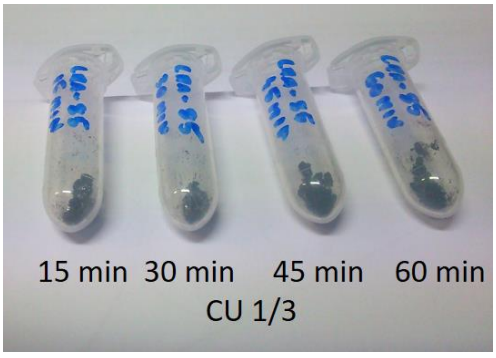

Figure 43.3. Appearance of citric acid – urea based C-dots at different reaction times

Functionalization of C-dots with APTES

The CU-based C-dots (from 15-60 min reaction) were functionalized by addition of 0.33 mL APTES to 10 mL aqueous solutions with a concentration of 1 mg mL^{-1} of the C-dots and stirred at room temperature for 24 h at 500 rpm.[107]

4.3.3. Results and discussion

The obtained dark brown solids have excellent water solubility, usually colors the water to yellow and exhibit strong fluorescence in just 1 mg L^{-1} concentrations. The collected 3D-spectra confirm the samples dual emission. Upon increasing the urea content, while keeping the reaction times constant (**rows on figure 43.4**), the rise of the green emission band can be observed at 520 nm. Analyzing data from the same reaction (**columns on figure 43.4)**, but at different reaction times, also confirms that green emission follows the formation of the blue emitting centers. Optimized composition for strong blue emission at 450 nm upon excitation at 360 nm is at CU 1/2 ratio, while strongest green PL was observed in the CU 1/3 samples, but always in pairs with an equally strong blue signal. The two signals are excitation independent and no shifts in emission wavelengths were observed by varying the reaction parameters. The characteristics excitation and emission bands are most recognizable in the CU 1/3 sample and highlighted by white dashed lines on **figure 43.4.**

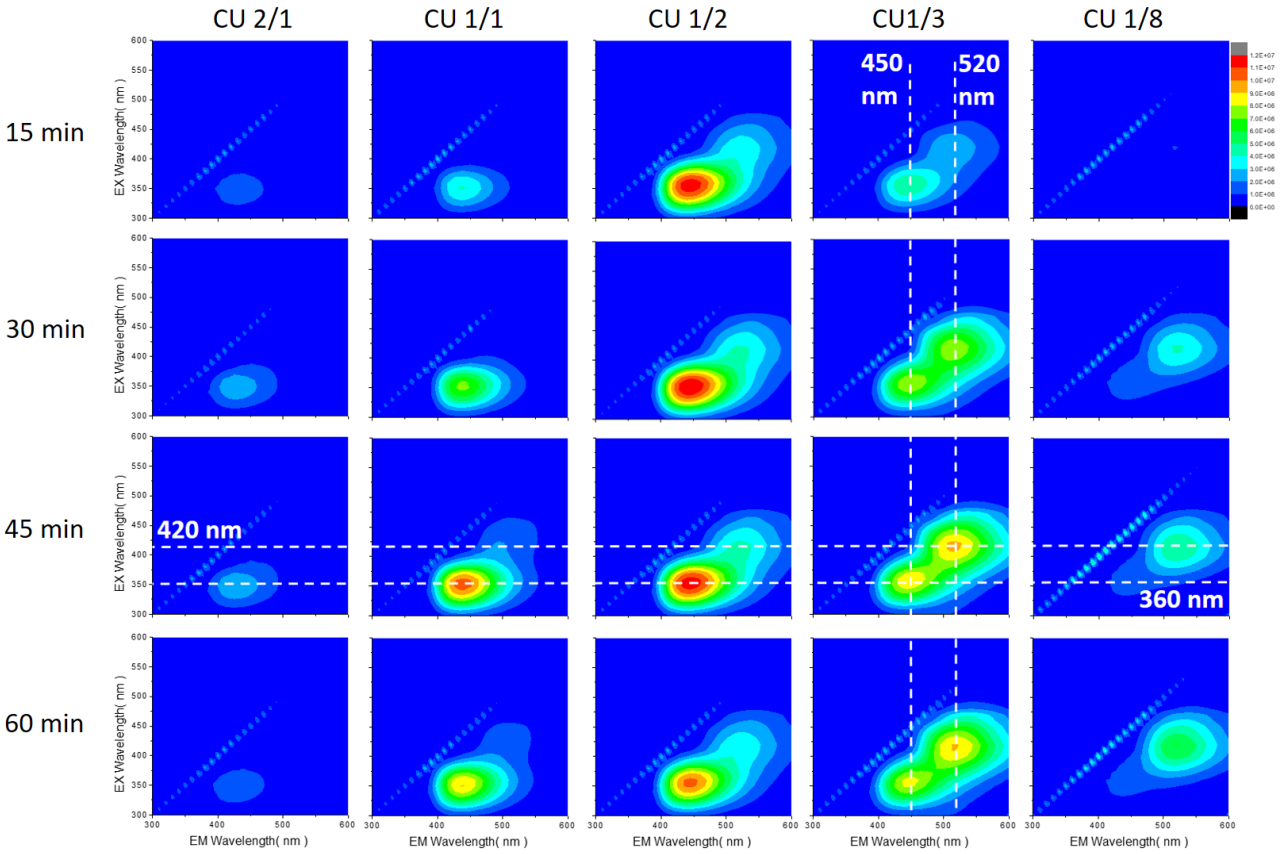

Figure 43.4. 3D fluorescence spectra (excitation (y-scale), emission (x-scale), intensity (false color scale)) of crude C-dots synthesized from citric acid and urea. Starting compositions indicated on top of the column and reaction times at the left side of the rows. All samples measured at 1 mg L^{-1} concentration and the same color scaling is applied for all the 3D maps. Characteristic excitation and emission wavelengths are indicated with white dashed lines.

Analysis of the emission intensity data of the samples obtained by varying the precursor ratio and plotted as a function time at the two emission peaks at 450 nm and 520 nm (upon excitation at 360 nm and 420 nm) reveals that the blue band's intensity usually peaks at 30-45 min, while the 520 nm band usually shows a constant emission intensity at longer reaction times, or even exhibit a continuous growth as the urea content increases (**figure 43.5**). The most fluorescent samples are the CU 1/2 for blue, and the CU 1/3 for green emission.

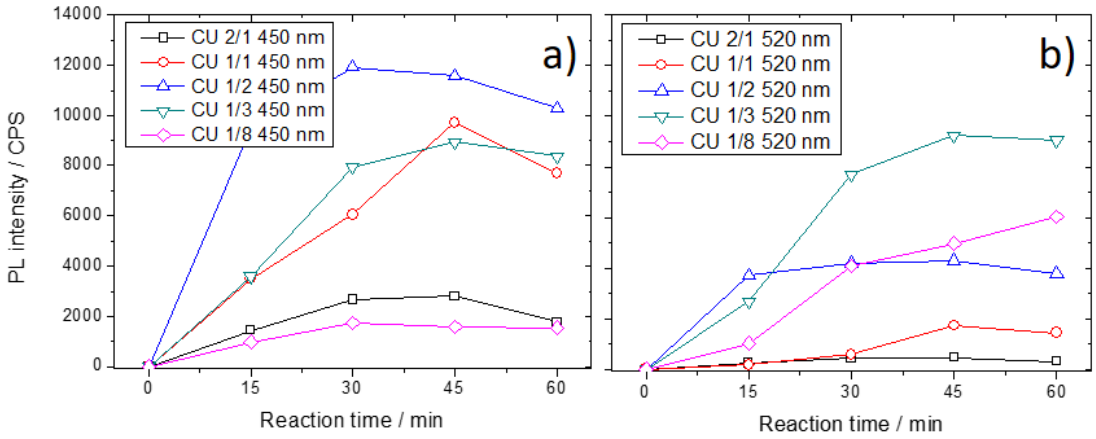

Figure 43.5. PL emission intensity change at 450 nm (a) and at 520 nm (b) upon 360 nm and 420 nm excitation, respectively, through the reaction course while different precursor ratios were used. All samples measured at 1 mg L^{-1} (aq) concentration.

The ratio of the two emission bands from the CU 2/1, 1/3 and 1/8 samples can be found in **figure 43.6**. The CU 2/1 emit almost exquisitely in the blue, while the CU 1/8 sample gives the "cleanest" green emission, especially at 60 minutes reaction time, and the CU 1/3 gives equal emissions in the blue range during the whole reaction, which makes this sample particularly interesting.

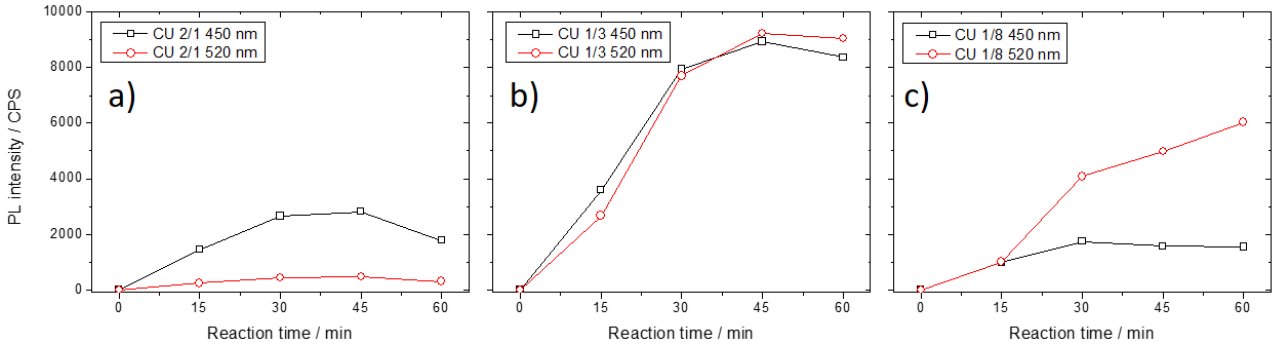

Figure 43.6. PL emission intensity changes at 450 nm (black) and 520 nm (red) upon 360 nm and 420 nm excitation, respectively, of the samples of CU 2/1 (a), CU 1/3 (b) and CU 1/8 (c) at different reaction times. The same scaling applies. All samples measured at 1 mg L^{-1} concentration.

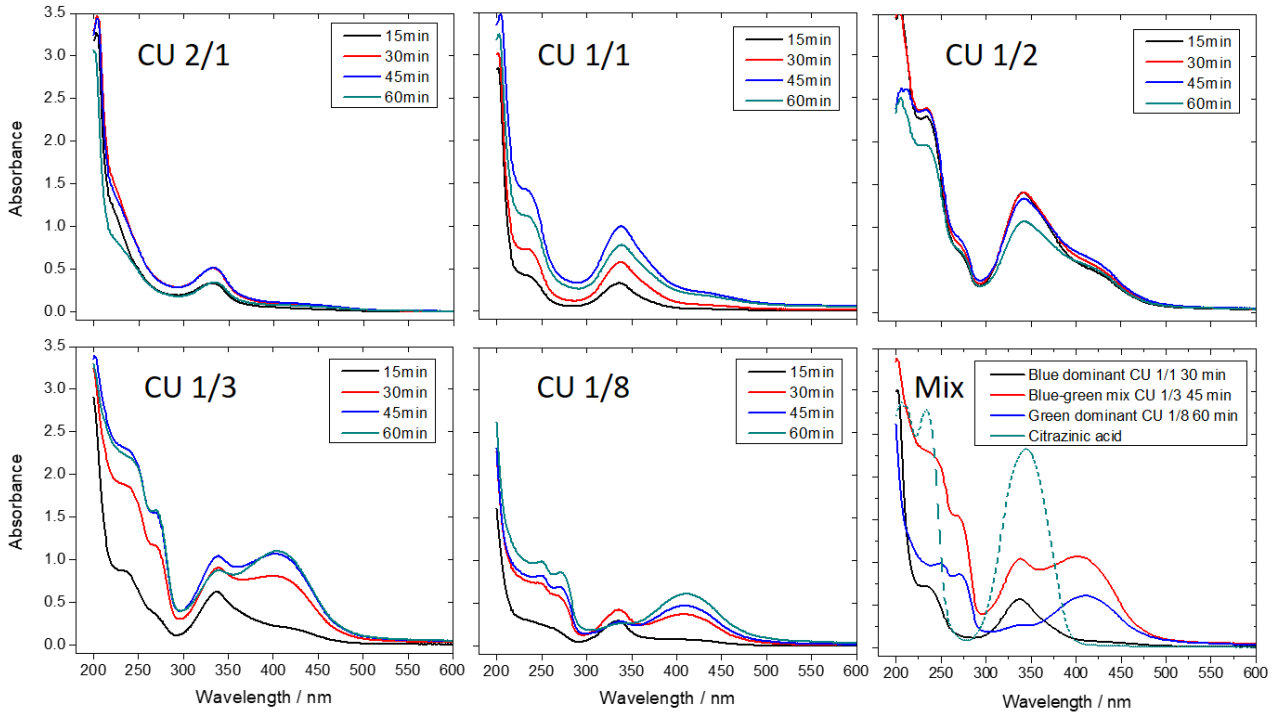

Figure 43.7. UV-Vis spectra obtained from aqueous samples of crude products at different reaction times from the reactions of different citric acid / urea ratios. The diagram "mix" shows a blue- and a green- PL emission dominant C-dots' spectra with a sample exhibiting dual emission. Dashed line shows the spectrum of the pure blue fluorophore: citrazinic acid. All samples were measured at 50 mg L^{-1} concentration.

UV-Vis spectra of the samples from different reaction times and precursor ratios are plotted in **figure 43.7**. CU 2/1 and 1/1 samples give absorbance bands around 230 and 340 nm assigned to π–π* and n-π* transitions (of citrazinic acid), while increasing initial urea content results a more complex spectrum as an emerge of another peaks at 250 and 265 nm (for π–π*) and at 405 nm (for n-π* of the pyridone ring of the HPPT) observed.[91] Displaying the UV-Vis absorbance spectra of blue- and green emission dominated C-dots together with the spectrum of C-dots with strong mixed emission (CU 1/3) clearly shows (**figure 43.7Mix**) that it is the sum of the two spectra. Additionally the spectrum of citrazinic acid was also plotted to highlight the similarity of its absorption band positions with the blue emitting C-dots' spectrum.

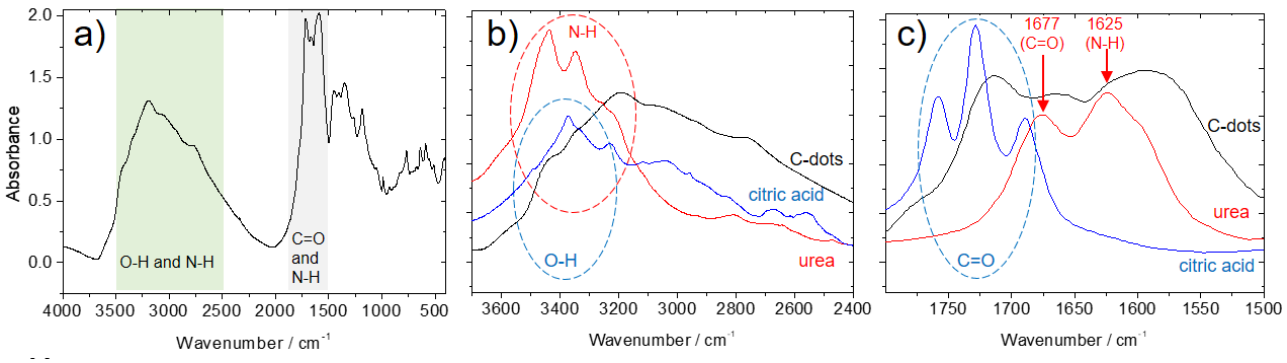

Figure 43.8. (a) FTIR spectra of the obtained CU 1/2 C-dots (black line) and its detailed comparison (b, c) with the reaction precursors (citric acid monohydrate-blue line, urea-red line) in the regions associated to O-H, N-H and C=O signals.

The carbon dots were highly hydrophilic due to the abundance of COOH and NH_2 surface functional groups as detected by FTIR spectroscopy (**figure 43.8**). Further analysis of the C-dots samples (**figure 43.8bc**) indicates the absence of the characteristic signals of citric acid monohydrate and urea in the highlighted regions, confirming a reaction of the chemical species. The dominant signals of precursors in the region of 3500-2500 cm^{-1} are mainly due to the O-H stretching of the carboxyl groups of citric acid, peaking[89] at 3360 cm^{-1} and the N-H stretching of urea (two peaks and a shoulder[142] between 3600-3200 cm^{-1}. The three C=O signals of citric acid monohydrate peak[88] between 1800-1600 cm^{-1} and the C=O (1677 cm^{-1}) and N-H (1625 cm^{-1}) signals of urea[143] dominate the region of 1800-1500 cm^{-1}. Thermal decomposition of urea alone[144] revealed that the formation of ammonia and isocyanic acid at the early stages of decomposition, firstly leading to biuret, cyanuric acid and ammelide formation at our reaction temperature and their characteristic infrared signals at 1324 (biuret), 1058 (cyanuric acid) and 977 cm^{-1} (ammelide) were also described. In our sample, the signal of biuret was missing (probably due to the long reaction time), but a bit shifted signals of the other two species were identified at 1053 and 988 cm^{-1}. The pyrolysis of citric acid (carbon dots formation) was followed by FTIR method[88] and the emerge of the signals of pyrocitric acids were monitored. However, in our case the signals of the expected first derivatives (aconitic acid and itaconic acid) were not obviously present, which is possible after considering the obvious possibility of reaction between the two precursors (citric acid and urea) and/or their pyrolysed byproducts (ammonia, isocyanic acid etc). Since urea applied in excess, it is more probable to find some products of urea pyrolysis than the ones from citric acid pyrolysis. The synthesis of carbon dots from citric acid and urea[91] already confirmed a source of fluorescence as citrazinic acid (and its amide).

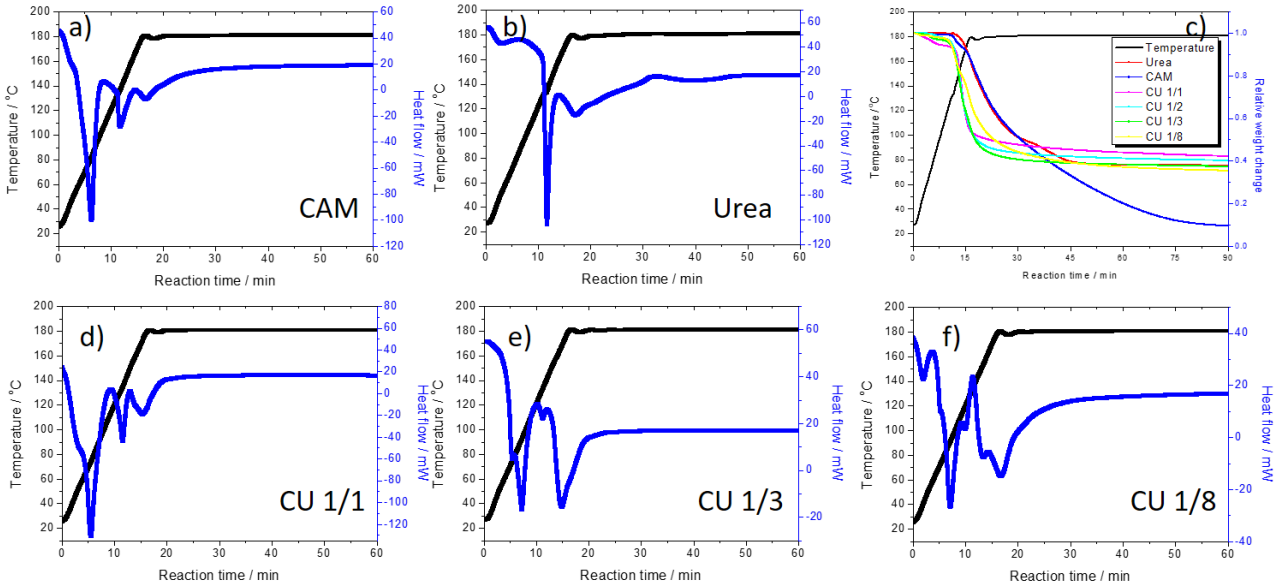

Figure 43.9. Calorimetric analysis of samples at the reaction temperature (180°C, black line): (a) citric acid monohydrate; (b) Urea; (d) citric acid/urea (n/n) 1/1, (e) citric acid/urea (n/n) 1/3, (f) citric acid/urea (n/n) 1/8. c) Relative weight change under synthesis conditions (TGA): citric acid (blue), urea (red) and citric acid/urea reactions (magenta turquoise, green, yellow).

The DSC results of the reference samples**:** citric acid monohydrate, urea, and the combination of CAM and urea and their relative weight changes at 180ºC (our reaction temperature) have been analyzed (**figure 43.9**). The endothermic events of melting of CAM (m.p. 135ºC, Fluka) and urea (m.p. 133-135ºC, Aldrich) appeared on the DSC curves (**figure 43.9ab**). The peaks observed after the melting points of reactants show an increasing complexity as the partition of urea grows, serving as an indicator of the additional reaction step of the formation of citrazinic acid and HPPT (**figure 43.9def**). Weight change (**figure 43.9c**) was not observed under ~160ºC (for CAM and urea) and ~135ºC (for CU mixtures) suggesting that there was no reaction resulting elimination of materials (H_2O, NH_3, HNCO or CO_2 due to decomposition, dehydration, condensation or decarboxylation), while weight loss appeared simultaneously with the melting of the components, therefore, DSC signals under those values should be assigned to morphological changes. Urea alone shows a 60% weight loss in 30 minutes due to decomposition and also CAM undergoes an intensive weight loss in the first 75 minutes of the reaction (see chapter 4.1) through dehydration and decarboxylation steps, starting at the temperature of 160ºC, while the reaction mixture suffers a 55-65% weight loss mainly in the first 10 minutes after reaching the 180ºC reaction temperature and forms a thermally more stable material (**figure 43.9c**) than CAM, however, a slow decomposition can be still detected afterwards.

Functionalization of C-dots with APTES

We have used, similarly to the previous chapters the 3-(aminopropyl)triethoxysilane (APTES) as a surface-modification agent to inspect the role of the surface groups on C-dots emission (**figures 43.10-13**) on four selected samples, exhibiting different optical properties. The functionalization with APTES greatly influence the emission spectra of the C-dots. While the blue emission remains unshifted, and its intensity decrease by 10-50% upon addition of APTES (**figures 43.10-12**), in contrast, the green emission switches off. The CU 1/8 sample, as emitting dominantly in the green region, shows a different response to APTES. Even though the green emission decreased, an intense blue emission formed instead. The changes of the PL emission also reflected on the UV-Vis spectra (**figures 43.10-13**) by decreased absorbance in the 400-420 nm range (responsible for green PL) and decrease in the range of 330-350 nm (responsible for blue PL), with the exception of the CU 1/8 sample which exhibited a great enhancement in light absorption at 330 nm (**figure 43.13c**) correlating to the change in the PL. The UV-Vis spectra of the blank solutions were also plotted, and obtained by mixing APTES in water at the same concentration and for the same reaction time as for the C-dots-APTES mixtures and measuring it after the same dilution.

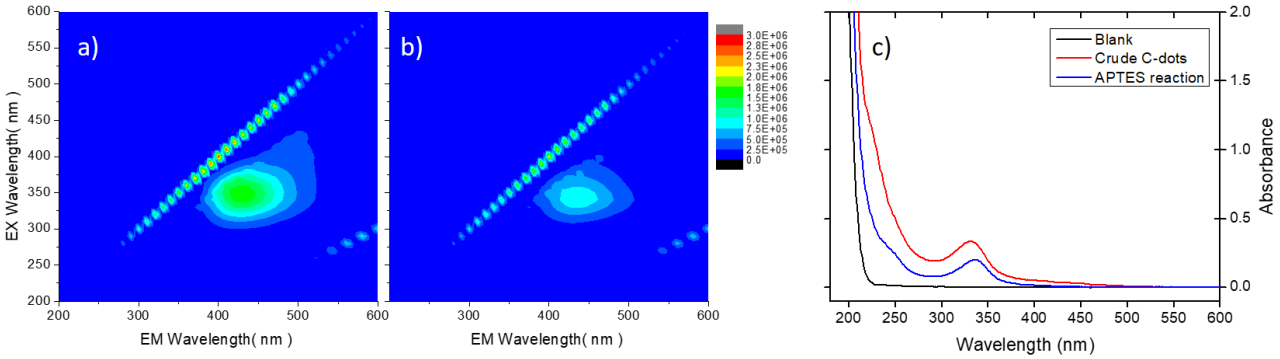

Figure 43.10. shows the 3D PL map (excitation/y-axis and emission/x-axis, false color scale) of the CU 2/1 (15min) C-dots dissolved in water (a) and after functionalization with APTES (b). Concentration of the C-dots are 1 mg L^{-1}. UV-Vis spectra (c) of the CU 2/1 (15 min) C-dots, the C-dots/APTES mixture and APTES aged in water (blank). Measured at 50 mg L^{-1}.

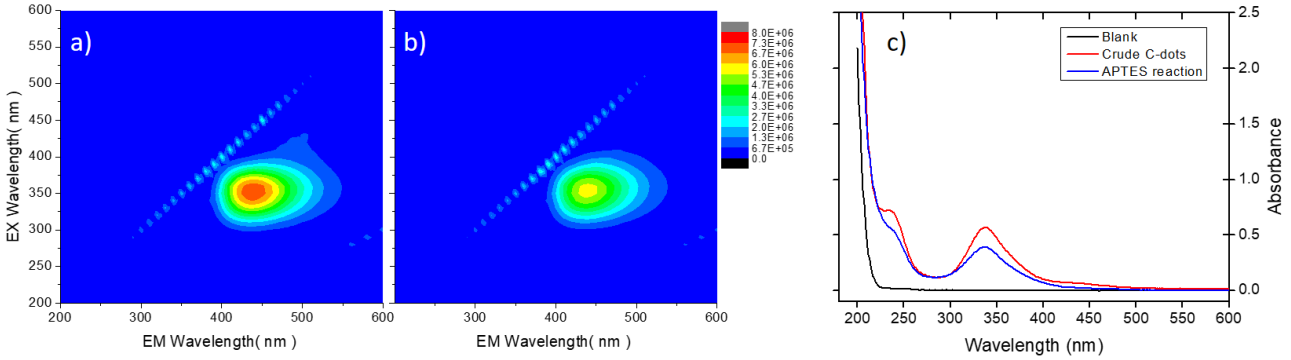

Figure 43.11. shows the 3D PL map (excitation/y-axis and emission/x-axis, false color scale) of the CU 1/1 (30min) C-dots dissolved in water (a) and after functionalization with APTES (b). Concentration of the C-dots are 1 mg L^{-1}. UV-Vis spectra (c) of the CU 1/1 (30 min) C-dots, the C-dots/APTES mixture and APTES aged in water (blank). Measured at 50 mg L^{-1}.

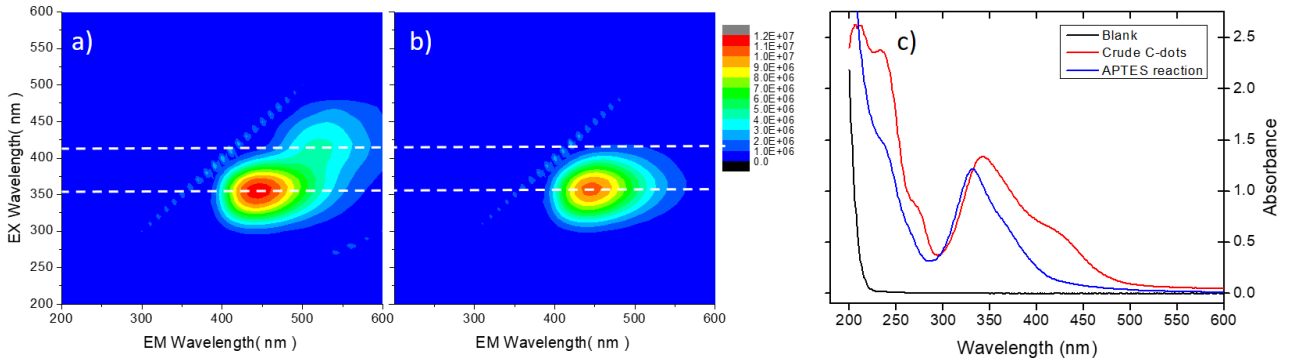

Figure 43.12. shows the 3D PL map (excitation/y-axis and emission/x-axis, false color scale) of the CU 1/2 (45min) C-dots dissolved in water (a) and after functionalization with APTES (b). Characteristic absorption bands are highlighted by white dashed lines. Concentration of the C-dots are 1 mg L^{-1}. UV-Vis spectra (c) of the CU 1/4 (45 min) C-dots, the C-dots/APTES mixture and APTES aged in water (blank). Measured at 50 mg L^{-1}.

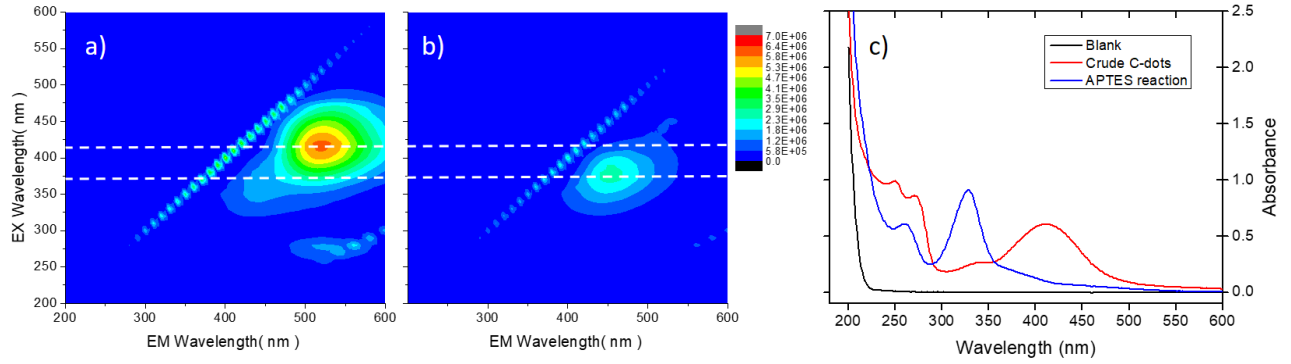

Figure 43.13. shows the 3D PL map (excitation/y-axis and emission/x-axis, false color scale) of the CU 1/8 (60min) C-dots dissolved in water (a) and after functionalization with APTES (b). Characteristic absorption bands are highlighted by white dashed lines. Concentration of the C-dots are 1 mg L^{-1}. UV-Vis spectra (c) of the CU 1/8 (60 min) C-dots, the C-dots/APTES mixture and APTES aged in water (blank). Measured at 50 mg L^{-1}.

4.3.4. Conclusions

Thermal reaction of citric acid and urea, as reported in the literature, under defined circumstances, produces fluorescent materials with dual PL emission at 450 nm and 520 nm. The reaction time and the precursor ratio are crucial parameters. Highly fluorescent C-dots have been obtained using short reaction times (15-60 min) by our pyrolysis method and fine tuning of the obtained optical properties were achieved. The formation of citrazinic acid and HPPT as molecular fluorophores responsible for the blue and green PL have been followed by PL spectroscopy and the data correlated to the UV-Vis and FTIR spectra and DSC/TGA data. Reaction parameters for the maximized emissions for both bands has been optimized and the water soluble, highly fluorescent crude C-dots have been surface functionalized by APTES, resulting characteristic changes in the optical properties. The addition of APTES switches off the green emission, while most of the cases, a simultaneous decrease in the blue emission occurs. These effect prove the interaction of the C-dots and APTES, however the findings partially in contrast to our previous results: in chapter 4.1 and 4.2, APTES functionalization yielded a silica protective layer on the C-dots, resulting an increased fluorescence in the blue or violet range (CA-Tris C-dots) or a decreased emission at higher wavelengths (CA C-dots). These CU C-dots, even though respond similarly to APTES, by decreasing PL intensity at higher wavelengths, the blue emission usually also decreases. We assume, that the explanation, just as the origin of fluorescence, is on the molecular level and addition of APTES might cleave the imide bond of HPPT and form a more citrazinic acid like molecule, exhibiting a weaker, but similarly blue emission. However to prove this theory, extended study on the topic is required.

4.4. Carbon dots for light-sensitized titania

4.4.1. Introduction

Titania (TiO_2) is a common photocatalyst, used for applications from food coloring to sun creams and often used for purification of air and water, deodorization, sterilization etc.[145-147] Titania is synthesized by several approaches like hydrothermal,[148] sol-gel,[149,150] sonochemical[151] and wet-chemical methods[152] and those products can be used for the removal[153,154] of industrial wastes (e.g. dye waste) from the environment. Numerous dyes are in everyday use, for example Rhodamine B (**figure 44.1**) as a fluorescent dye applied as a tracer in water to determine the flow rate and flow directions to trace other pollutants (like herbicides) transport in natural waters,[155] moreover it is used in biology as a staining fluorescent dye.

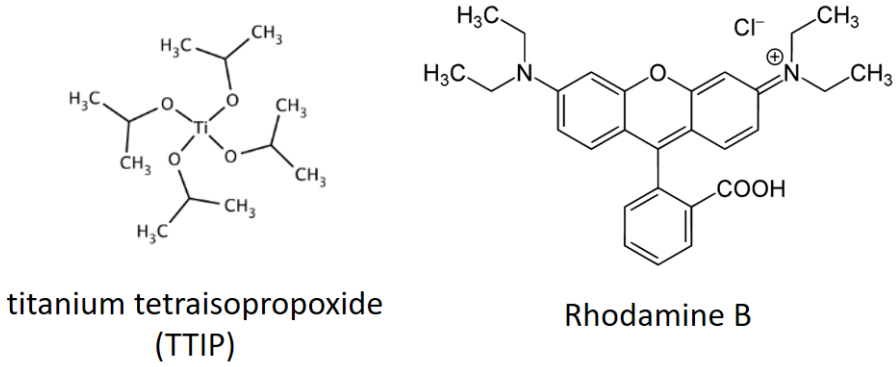

Figure 44.1 Structures of titanium tetraisopropoxide and Rhodamine B

TiO_2 is a paramount photocatalyst, which was explored by Fujusima et al. in 1972.[156] It appears as a white solid and belongs to the family of transition metal oxides. It mainly occurs in three polymorphs which are rutile, anatase and brookite. Rutile has a tetragonal structure and it is stable at most temperatures and pressures, but shows only low activity as a photocatalyst. Anatase TiO_2 also has a tetragonal structure and good stability. Among the three polymorphs, anatase TiO_2 is preferred for photocatalytic studies due to its high electron mobility, low dielectric constant and lower density, while brookite is rarely used for experimental purpose. TiO_2 has large band gaps with 3.02 eV for rutile, 3.2 eV for anatase and 2.96 eV for brookite.[157]

In TiO_2 when exposed to near UV light, the electrons in valence band move to conduction band, creating holes,[158] which contribute in the formation of radicals, the reactive species to degrade organic pollutants. The photocatalytic activity of TiO_2 largely determined by the crystalline phase,

size and specific surface area.[159] To further enhance the photocatalytic activity of TiO_2, various methods, like dye sensitization, doping, coupling and capping of TiO_2 have been explored.[157,158,160]

A recent study[161] reported a simple method to prepare an efficient photocatalyst against methylene blue, by a simple precipitating method, using titanium tetraisopropoxide (TTIP, **figure 44.1**) as precursor in a low temperature (120°C) calcination process. This synthesis method is apparently optimal for embedding heat sensitive C-dots into the precipitating TiO_2 for forming organic-inorganic hybrid particles and test if some sensitization[80,162] towards natural sunlight occurs, resulting an enhanced photocatalytic activity against Rh B, which used as a model molecular pollutant in our study.[163]

Therefore we used citric acid, tris(hydroxymethyl)aminomethane (Tris) and urea based C-dots and their more stable and often more fluorescent (3-aminopropyl)-triethoxysilane (APTES) functionalized derivatives in ethanol (adapted from chapters 4.1-4.2-5.1). Embedding these stabilized and protected C-dots (0.3% loading) into a low temperature titania matrix was expected to increase its overall photocatalytic efficiency against Rh B under direct sunlight.

4.4.2. Experimental

Chemicals and reagents

citric acid/Tris 3/1 (10 min) C-dots (CT)	from chapter 4.2.
citric acid/urea 1/2 (45 min) C-dots (CU12)	from chapter 4.3.
citric acid/urea 1/8 (60 min) C-dots (CU18)	from chapter 4.3.
titanium tetraisopropoxide (TTIP)	Aldrich, 97%
3-(aminopropyl)triethoxysilane (APTES)	Aldrich, 99%
Rhodamine B (RhB)	Aldrich, >95%
P25 (TiO_2, nanopowder, <21nm) – commercial photocatalyst	Aldrich, >99.5%
ethanol (EtOH)	Carlo Erba, 99.9%

In-site produced Milli-Q water was used for the analysis.
All chemicals were utilized without further purification.

Synthesis

C-dots were prepared by reproduction of synthesis methods described in chapters 4.2 and 4.3. Three fluorescent C-dots were prepared (**figure 44.2**):

1. CT: citric acid/Tris 3/1 (10 min reaction, 180°C) C-dots
   PL (CT): max excitation/max emission: 340/410 nm
2. CU12: citric acid/urea 1/2 (45 min reaction, 180°C) C-dots
   PL (CU12): max excitation/max emission: 360/445 nm
3. CU18: citric acid/urea 1/8 (60 min reaction, 180°C) C-dots, max excitation/max emission:
   PL (CU18): max excitation/max emission: 420/520 nm

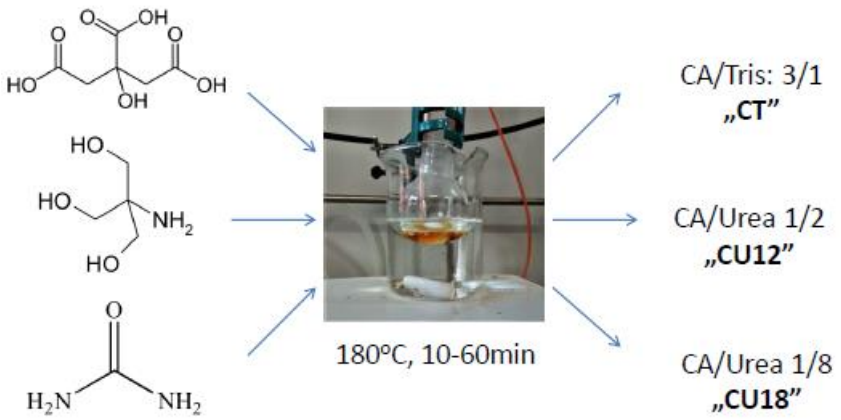

Figure 44.2. Representation of the C-dots syntheses.

The procedure of APTES functionalization of the C-dots adapted from chapters 4.2 and 4.3, but EtOH was used as a solvent in the mixture to satisfy the present method's requirements (dry conditions for mixing with TTIP). Briefly, the solution of 10 mg C-dots / 10 mL EtOH was stirred with 0.33 mL APTES at room temperature for 24h prior to use.

The titania reference sample was prepared[161] by mixing 2.50 mL TTIP in 7.50 mL EtOH and dropwise adding 7.50 mL of water to form a white precipitate, which was aged for 24h, filtered through a Whatman grade 6 filter paper (pore size 3 μm) and washed with 2x10 mL water and 2x10 mL EtOH. The white solid dried at 60°C for 1h and at 130°C for 24h.

The C-dots or C-dots/APTES loaded titania was prepared by following the steps of preparation of titania reference, but the 2.50 mL TTIP was mixed with 7.50 mL of the prepared ethanolic C-dots or C-dots/APTES mixtures.

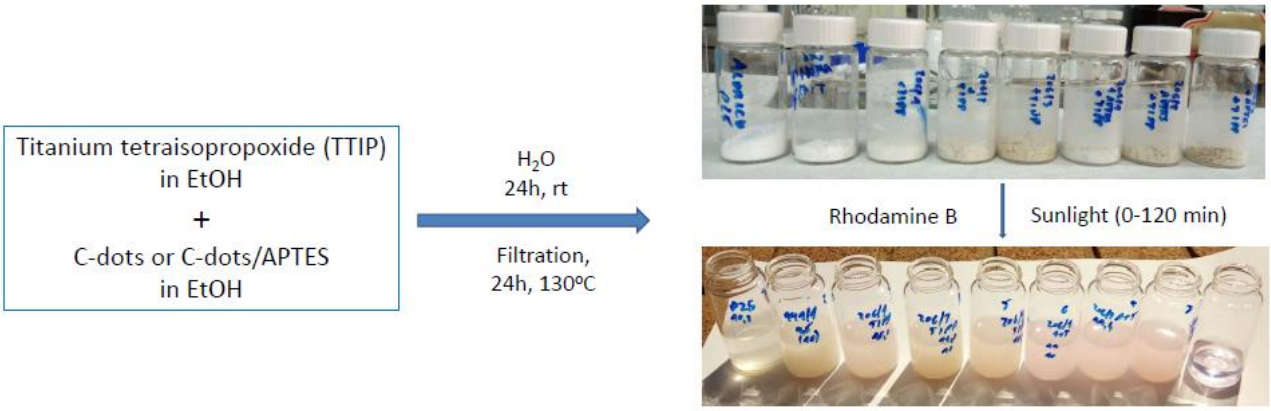

Figure 44.3. Preparation of C-dots or C-dots/APTES loaded titania, their appearance as solids, and under sunlight during the decomposition of Rh B.

Photocatalysis tests

5 mg of the dry titania precursor (P25, the reference precipitated titania and the six co-precipitated samples) were mixed with 5.0 mL of 10 μM Rh B (aq) and the eight mixtures were stored in the dark for 30 minutes, meanwhile the aliquot lost 35-44% of the measured PL intensity due to adsorption on the surface of the photocatalysts. These values were used as a reference for decomposition rates during the experiment, while irradiated by sunlight for 2h (**figure 44.3**). As another reference, 10 μM RhB (aq) was also stored in the dark for 30 minutes, without any loss of its PL. All the samples for photoluminescence were prepared by taking 0.10 mL of the mixed suspension and diluted to 3.00 mL by water.

4.4.3. Results and discussion

The samples irradiated by sunlight exhibited different oxidizing power against Rh B (**figure 44.4**). P25 gave the best result as decomposed 90% of the dye in 30 minutes. Surprisingly, the reference pure titania showed the second strongest photocatalytic effect, by decomposing 80% of the dye in 2h. While the C-dots "sensitized" catalysts performed differently, and all showed a weaker photocatalytic power than pure titania samples under the same conditions. Especially the APTES coated C-dots based hybrid titania performed very weakly, as they neutralized less Rh B than the reference Rh B natural decomposition under sunlight, practically acting as a protective/deactivating additive in the system.

One C-dots sample, the CU 1/8, which exhibits light absorbance and PL emission in the visible range, at some degree, outperformed the other "sensitizers", but still could not reach the efficiency of pure titania.

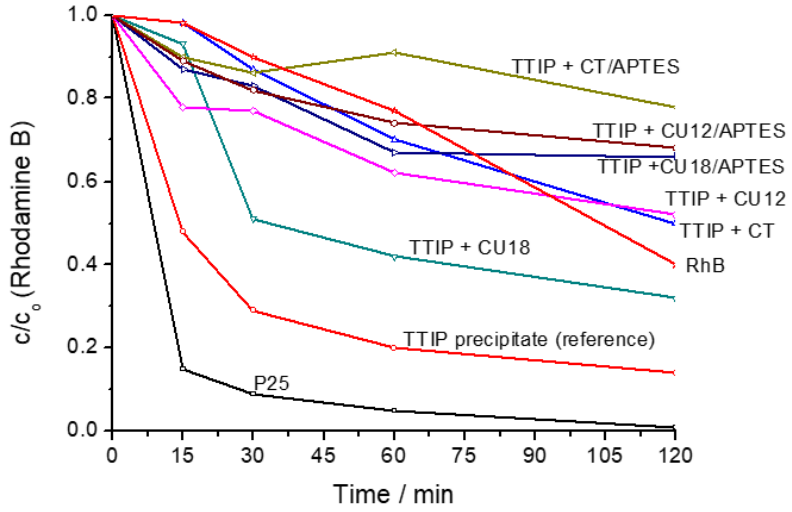

Figure 44.4. Decomposition rates of Rh B under sunlight, by applying different titania based photocatalysts.

4.4.4. Conclusions

Carbon dots with strong fluorescence at different wavelengths were embedded into precipitating titania to test their photosensitizing effect. Only low temperature (130°C) thermal treatment was applied to preserve the C-dots optical properties. These titania-carbon dots (and APTES) hybrid materials were tested by decomposing Rhodamine B under direct sunlight and showed lower activity than references (blank and P25), but the C-dots with highest excitation/emission wavelengths (TTIP+CU18) performed better than the others. One possible explanation of the low performance of the APTES-modified samples is a deactivating effect of the silica layer, as it separates the C-dots from the titania catalyst. On the other hand, the bare C-dots can be also considered as organic molecules (especially the ones from very short reactions) adsorbed on the surface of titania particles, which, even if plays a positive role in photosensitization, eventually autocatalyzes their own degradation, providing additional material competing with RhB in the decomposition process, The CU18 sample is different by two aspects: on one hand, it is the most carbonized sample (from the longest reaction), therefore it is probably the less molecule-like product, giving less of a target for photodegradation, while on the other hand, it absorbs light at the highest wavelengths, giving a way for a different, more efficient interaction with the titania photocatalyst. Further study is still needed to optimize C-dots and APTES loading for tuning their optical properties.

5. Syntheses and applications of p-phenylenediamine based carbon dots

5.1. Syntheses and stability

5.1.1. Introduction

The PL emission wavelengths for most reported C-dots are concentrated in the blue-light region, which limits their applications.[3] Important milestones in green[164], yellow[165], orange[166] and red[167] light emissions have been achieved, when the reported C-dots' quantum yields (QY) have surpassed 50%; however, longer wavelength emission still remained less effective.[168]

Some studies were dedicated to understanding the mechanism of red emission in C-dots, but it often occurs in combination with a dominant blue-emission, exhibiting excitation-dependent emission properties, thus high wavelength emission can be observed only when the excitation is in the longer, green, yellow or red region too, where the emission mechanism is usually attributed to the surface states transition.[169-171] However, truly labeled red-emission C-dots, which show a dominant emission around or over 600 nm, have also been reported[172-180] and can be divided into two main categories: one relates to C-dots prepared via phosphorous acid treatment, while the other associates the red-emission of C-dots to the used precursor: *p*-phenylenediamine (pPD, **figure 51.1**).

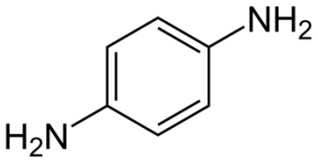

p-phenylenediamine (pPD)
benzene-1,4-diamine
CAS: 106-50-3
M_r: 108.14
mp: 138-143 °C
bp: 267 °C

Figure 51.1. Structure and properties of *p*-phenylenediamine

Treatment with phosphoric acid can be considered as a general strategy for preparation of longer-wavelength emitting C-dots.[172,181] Several bioprecursors have been also reported for red-emission C-dots through phosphorus acid treatment[182] and this method also makes possible the formation of C-dots with emissions covering the entire visible spectrum.[174] The mechanism is attributed to the dehydrogenation reactions occurring during carbonization, resulting the formation of the oxygen rich surface states. These C-dots always show excitation-dependent PL properties and their quantum yields (QYs) are typically less than 10%. Red-emitting C-dots based on pPD through solvothermal reactions were already reported in 2015, with a good QY of 25%.[183] Another C-dots covering the entire visible range by using only pPD and urea as precursors through a hydrothermal method has been reported,[184] while synthesis of C-dots from pPD by a microwave-assisted method[185] and solvent-tuned C-dots based on pPD through a hot injection synthesis method with QY of 34%[186] were also published.

C-dots based on pPD was thoroughly studied based on a series of solvothermal synthesis methods, by applying five differently polar solvents: water, ethanol, dimethylformamide, cyclohexane and toluene [86] and provided interesting PL emission at around 600 nm, correlating the PL maxima with the polarity of the solvent.

Since these C-dots dominantly (or even exclusively) bear amino functional groups on the surface, we selected this method to reproduce the synthesis of the toluene-based, then the EtOH-based C-dots[86] to further study the role of these surface functional groups in the red emission range. Application of various solvents (EtOH, water, diluted mineral acid) revealed different PL-response[187] and hydrodynamic stability of the particles, which gives an insight of the chemistry of the surface groups and related emitting transitions, while an organosilane agent acting as a surface passivator also greatly influenced the PL properties. These findings might serve well for optimization of synthesis conditions for applications such as embedding C-dots in sol-gel systems,[104] or PL responsive measurements of pollutants in aqueous samples.

5.1.2. Experimental

Chemicals and Reagents

p-phenylenediamine (pPD)	Aldrich, 98%
3-(triethoxysilyl)propyl isocyanate	Aldrich, 95%
sulfuric acid	Carlo Erba, 96%
ethanol (EtOH)	Carlo Erba, 99.9%
toluene	Aldrich, >99.9%
FTIR grade potassium bromide	Aldrich, >99%

All chemicals were utilized without further purification.

In-site produced Milli-Q water was used for the analysis.

Precursors did not show observable fluorescence under our measurement conditions.

Synthesis of C-dots

108 mg (1 mmol) *p*-phenylenediamine (pPD) was placed in an autoclave equipped with a 50 mL Teflon inlet and mixed for 5 minutes in 10 mL of toluene or ethanol (EtOH). The sealed reactor was placed into a preheated 140°C oven and gradually heated to 200°C in 1h and kept at that temperature for further 5h, afterwards the mixture was allowed to cool down to ambient temperature during the night.[86] The reaction in EtOH resulted a red solution, while the one in toluene yielded a red sticky solid with toluene as supernatant, which latter mixture was usually dissolved by addition of 10-100x volume of EtOH and sonication.

Functionalization of C-dots with 3-(triethoxysilyl)propyl isocyanate

The C-dots synthesized in toluene was sonicated in its supernatant for 20 min and then 0.50 mL of the suspension was diluted to 5.00 mL by EtOH and then stirred in a sealed vial. After 1h, 3-(triethoxysilyl)propyl isocyanate (0.10 mL) was added to the mixture[188] and samples were taken at different reaction times and further diluted by 10x in EtOH prior to optical measurements (altogether 100x dilution of the original C-dots sample). The expected reaction occurs between the amino and isocyanate functional groups at room temperature in a matter of hours/days to yield a substituted urea as **formula 51.1** describes. The used solvent (EtOH) could also act as a reactive agent to form an urethane with the alkyl isocyanate, but isocyanates are more reactive towards the amine functional groups.

Formula 51.1 Reaction of a primary amine with an alkyl isocyanate yielding a disubstituted urea.

5.1.3. Results and discussion

Two pPD-based solvothermal experiments were reproduced, one in toluene and one in EtOH. The two crude products, without any further purification, give very similar PL properties to the reported data.[86] The C-dots made in toluene and diluted 100x in EtOH (since it has low solubility in toluene) exhibit emission only in the red at 605 nm, while the one synthesized in EtOH has two emission bands, one in the violet (400 nm) and one in the red, at 605 nm (**figure 51.4**). The blue emission is due to the increased oxygen content (from EtOH) and related to the defect states of the C-dots N-rich graphitic structure, while this effect is absent in the toluene based C-dots, where additional oxygen is not present in the reaction system. The red PL emission is associated to the nitrogen-containing organic fluorophores present in both systems (**figure 51.2**).

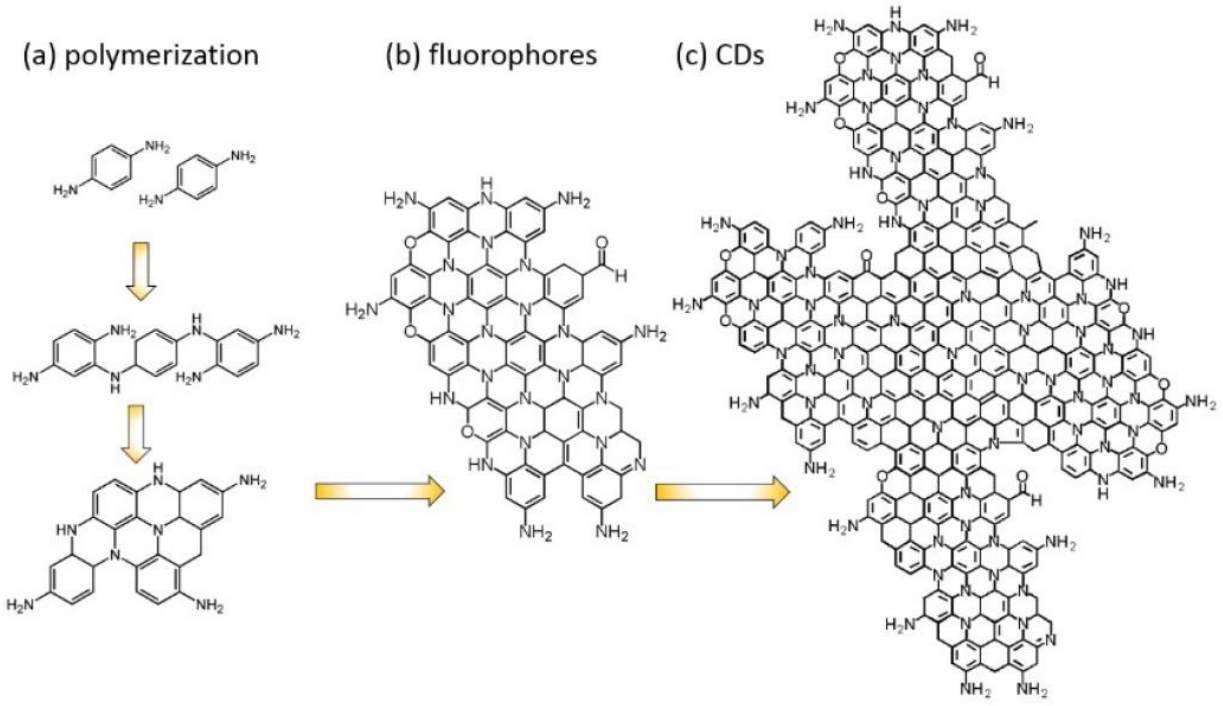

Figure 51.2. Illustration of the formation process of C-dots based on polymerization of pPD. (a) polymerization of pPD, (b) formation of nitrogen containing fluorophores and (c) possible structure of C-dots. Reproduced from reference[86] with permission from The Royal Society of Chemistry.

The UV-Vis data also revealed three characteristic absorbance bands (**figure 51.3a**): a shoulder around 220 nm (π-π* transition of the aromatic sp^2 domains, such as C=C and C=N), 270-350 nm (n-π* transition of oxygenous functional groups: C-O and C=O) and 400-620 nm (assigned to surface group transitions).[86] The FTIR spectra (**figure 51.3b)** also displayed the reported characteristic peaks of the C-dots: around 3300 cm^{-1} (primary and secondary amines as -NH_2 and -NH-), 1627 cm^{-1} (C=N), 1519 cm^{-1} (C=C), 1263 cm^{-1} (N-H), and 1163 cm^{-1} (C-O).[86] All data confirmed that same products as reported were obtained and further characterization was therefore unnecessary.

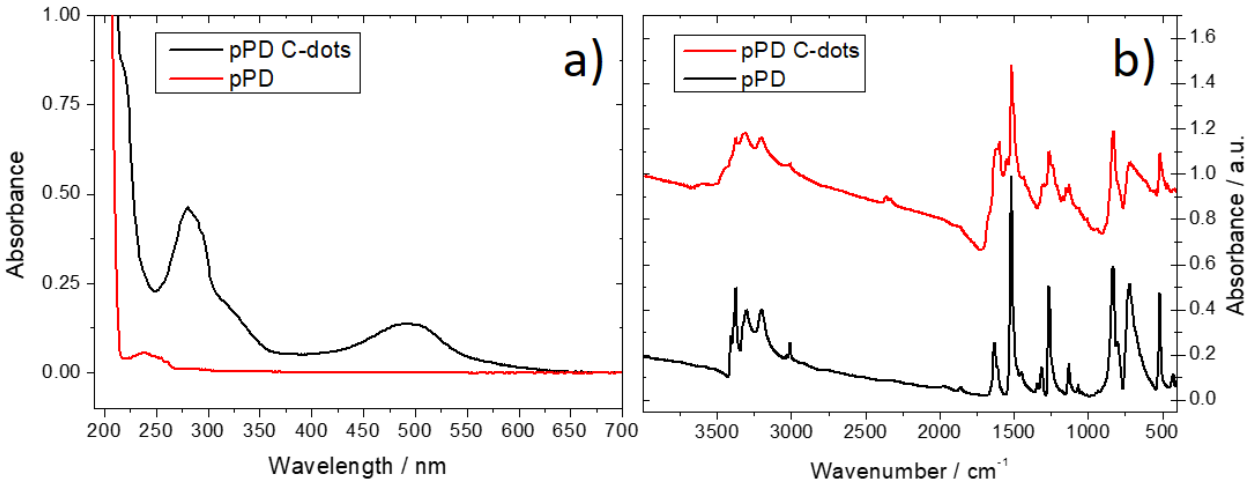

Figure 51.3. a)UV-Vis spectra of pPD and pPD C-dots by synthesis in EtOH and b) IR spectrum of the precursor and the C-dots.

Both C-dots were further analyzed: the C-dots synthesized in toluene was subject of surface functionalization by organosilane precursor, while the C-dots synthesized in ethanol was tested for solubility and stability for further use as nitrite ion probes (chapter 5.2).

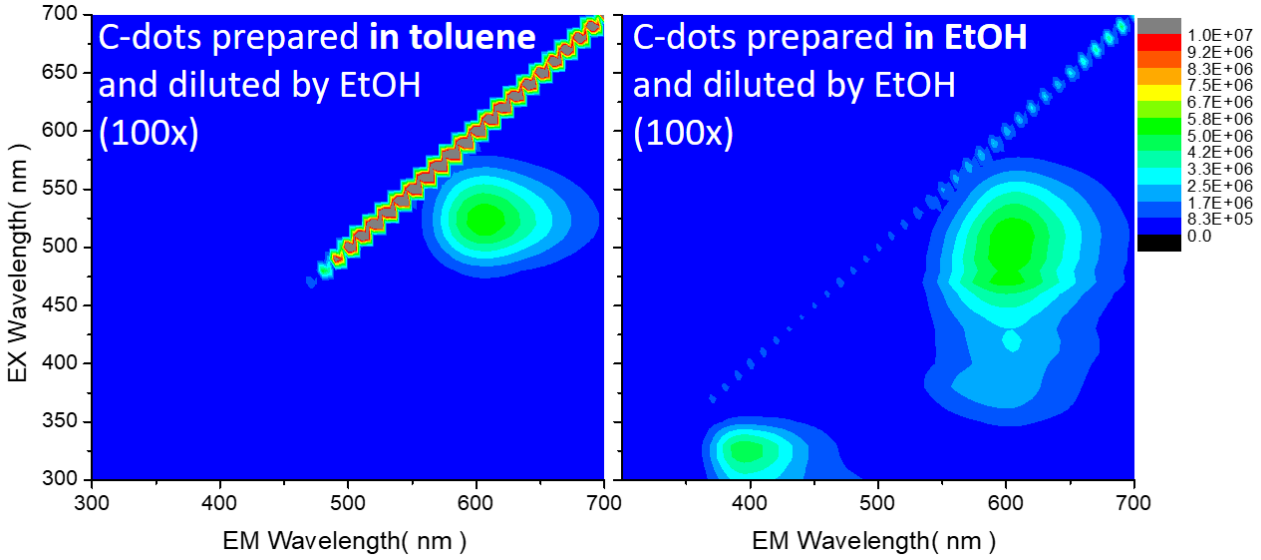

Figure 51.4. 3D fluorescence spectra (excitation (y-scale), emission (x-scale), intensity (false color scale)) of C-dots prepared in toluene (left) and in EtOH (right). Both samples were 100x diluted by EtOH, using the obtained (sonicated) reaction mixture. Same color scaling applies for both spectra.

The C-dots obtained by the toluene method was nearly impossible to dissolve in any solvent except EtOH, while the product synthesized in EtOH was homogenous and easy to handle, therefore, only that was subject of stability analysis. It was possible to dilute and obtain homogenous mixtures by using EtOH, water and 1% sulfuric acid (aq). 100x diluted solutions of the crude reaction mixture were prepared and subjected of stability analysis by monitoring their PL spectra (**figure 51.5**). The sample diluted in EtOH showed excellent, excitation independent emission at 605 nm upon the optimal excitation of 510 nm, but aging in solution at room temperature for 4 weeks resulted an unshifted, but 70% weakened emission intensity. The sample diluted in water exhibited a similar 605 nm emission, but upon excitation of 470 nm light and only 11% of the initial intensity of the C-dots dissolved in EtOH, which fluorescence was lost in only 4 days upon storing the sample at ambient temperature. Most interestingly, the sample diluted in 1% sulfuric acid (aq) resulted a characteristics change in the optical response. The PL emission became excitation dependent and observed in the range of 400-550 nm (excitation) and 475-650 nm (emission). Moreover, the C-dots in acidic solution showed an excellent stability up to 6 weeks, losing only 9% of the initial peak emission at 535 nm upon excitation at 470 nm. This must be the consequence of the protonation of the surface amine functional groups, which results better solubility in aqueous media and stability due to the repelling effect of the positively charged (protonated) particles. While in the case of water, as a less appropriate solvent, a slow aggregation occurs. This is due to, except some small derivatives, that amines have poor solubility in water in their unprotonated form. The theory is supported by the intensity of the scattered light observable on the 3D PL spectra of aqueous solutions (diagonal signals). The four days

aged sample showed a more intense scattering, which might be a result of aggregated particles. In the case of 1% sulfuric acid, the scattered light intensity apparently did not change, further proving the stability of the particles. In contrast, in ethanol, the scattered light intensity decreased, which allows us to theorize, that EtOH, as an excellent solvent for amines, might partially disassemble the particles, while inactivates some emission centers. Interestingly, this effect only appears in highly diluted samples (100x), while the original ethanolic reaction mixture apparently stable for months (in accordance to the source literature).

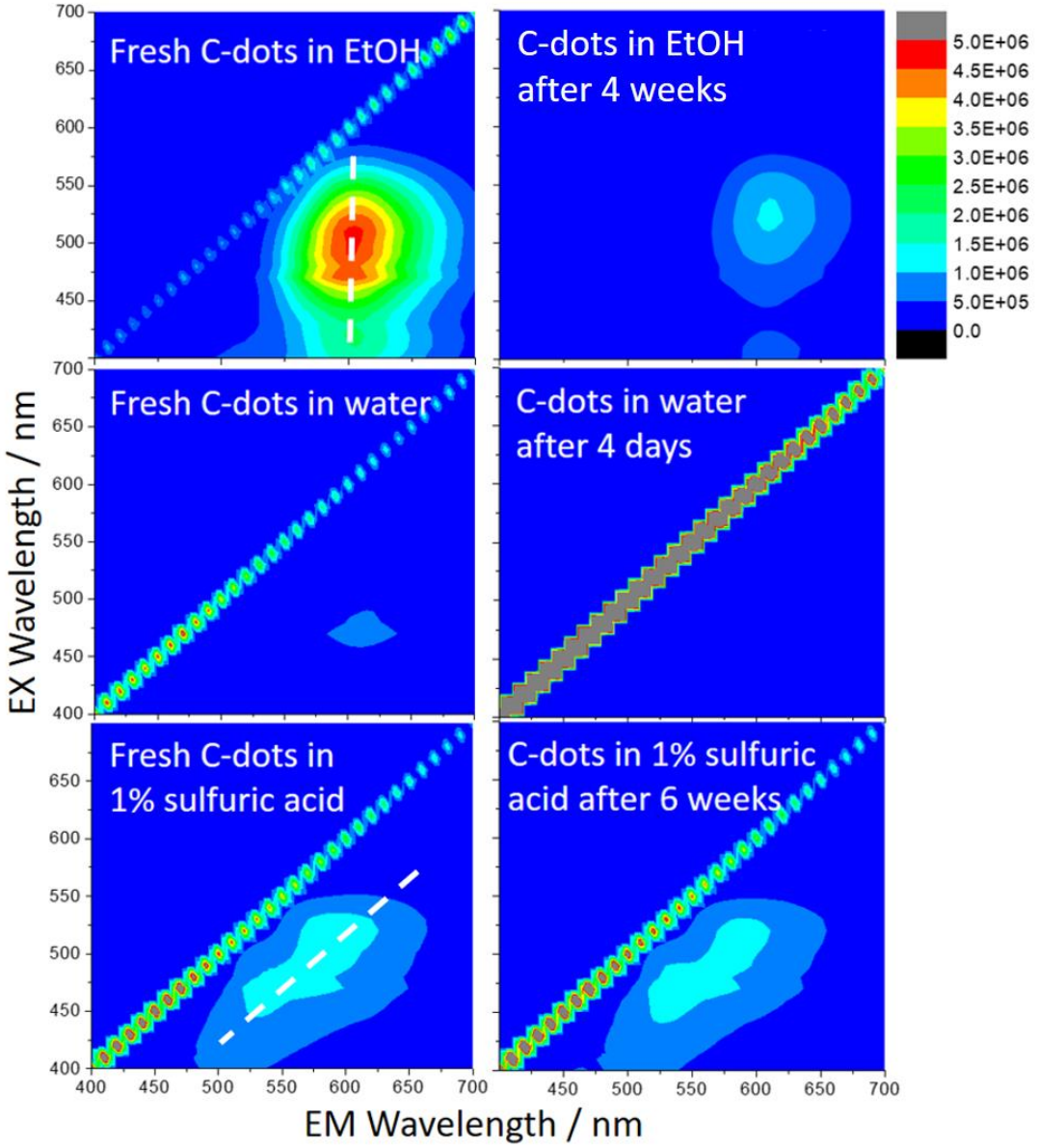

Figure 51.5. 3D fluorescence spectra (excitation (y-scale), emission (x-scale), intensity (false color scale)) of C-dots prepared and diluted in EtOH by 100x as preparead (upper left) and after aging for four weeks in solution (upper right). Same C-dots diluted by water (100x) as prepared (middle left) and after four days of aging in solution (middle right) and the C-dots diluted in 1% sulfuric acid (aq) as prepared (bottom left) and after six weeks of aging in solution (bottom right). All spectra applies the same color/intensity scale. White dashed lines indicate the PL emission dependency: emission is excitation independent in EtOH, while dependent in diluted sulfuric acid.

Functionalization by 3-(triethoxysilyl)propyl isocyanate

Similarly to the previously reported C-dots' surface decoration with an amino functionalized organosilane (chapter 4.1-4.3.) for possible further applications, we hereby tested the effects of an appropriate isocyanate derivative, which is able to covalently bond to the C-dots' surface amino groups by forming an urea derivative. This reaction runs at room temperature while influences the PL properties of the substance (**figure 51.6**) and reveals a gradual blue shift of 80 nm, which is very similar to the observed 90 nm shift of citric acid based C-dots upon functionalization with APTES, which let us assume, that a similar protective layer forms on the surface of C-dots in both cases.

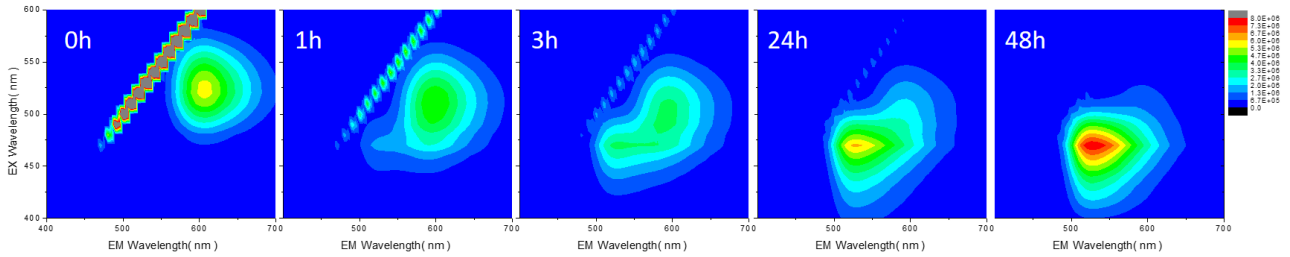

Figure 51.6. 3D fluorescence spectra (excitation (y-scale), emission (x-scale), intensity (false color scale)) of C-dots synthesized in toluene and reacted with 3-(triethoxysilyl)propyl isocyanate at different reaction times. Samples diluted in EtOH by 10x from the reaction mixture. Excitation maximum shifts from 520 to 470 nm and the emission maximum shifts from 605 to 525 nm, while the intensity increase by 42%, clearly indicating the reaction occurs on the particles surface.

5.1.4. Conclusions

Amine capped C-dots made from *p*-phenylenediamine were synthesized by a reported method using solvothermal reactions (toluene and ethanol). The particles show different PL properties. The one prepared in toluene exhibit only one emission band at 605 nm, while the other synthesized in EtOH has dual emission at 400 and 605 nm. Their optical responses were tested by using different solvents (EtOH, water and diluted sulfuric acid), which revealed that protonation of the particles' surface groups results a significant change from excitation independent to dependent PL emission, while the hydrolytic stability of the C-dots are greatly enhanced. This finding makes possible to use such particles for analysis of aqueous samples (chapter 5.2). Furthermore, the surface reaction with an organosilan was also investigated and the reaction progress was monitored by the gradual change of its PL-emission. A two days reaction at room temperature revealed that as the surface functionalization progressed, an 80 nm blue shift in the emission occurred. This finding is in accordance with the earlier (chapter 4.1.) reported blue shift upon APTES functionalization of citric acid based C-dots. This organosilane functionalization can help to embed C-dots with such high wavelength emission into silica matrices.

5.2. Nitrite ion sensing

5.2.1. Introduction

Nitrite and nitrate are naturally occurring anions and have great importance in the environmental samples like water, soil and agriculture products[189] simply as intermediates of the nitrogen cycle or as remains of commonly used nitrogen fertilizers.[190] Their salts' general high solubility give them access to ground- and surface waters, and finally sea- and drinking waters too. Nitrate is the more stable[191] and therefore typically found in higher concentrations.[192,193] However, under anaerobic conditions, nitrate may be reduced by microbes to nitrite and the denitrification process can go even further to nitrogen gas.[194]

Nitrite salts have numerous applications such as corrosion inhibitor[195], in dye manufacturing[196] and food industry,[189,197] and plays a role in aquaculture diseases;[198] its presence in drinking water and foods is harmful to humans and animals as well,[199] therefore, careful monitoring of these pollutants have paramount importance. Numerous methods, like spectrophotometric (e.g. based on the Griess reaction), electrochemical, chromatographic, capillary electrophoretic or spectrofluorometric methods etc. have been developed. Since spectroscopy provides excellent detection limits and simple protocols, they are still the most common ones for nitrate and nitrite determination.[189,200] Among the Griess reaction based spectroscopic methods, as low as a 2-40 μgL^{-1} (0.14-2.85 μM) linear range and 1.4 μgL^{-1} (0.10 μM) detection limit was reported for NO_2^-N by using 8-12 times concentrated samples and light absorbance detection around 537 nm.[189,201] In a more sophisticated method, by applying reduced graphene oxide/aggregated triangular plate-type nanosilver/Rh 6G nanosensor provided very sensitive determination based on surface enhanced Raman scattering. The dye concentration decreased via a nitrosation reaction between the dye and nitrite ions. The SERS intensity was linear to the NO_2^- ion concentration from 0.7 to 72 nmol L^{-1}, with limit of detection as low as 0.2 nmol/L.[202] Another graphene oxide based method reached a detection limit of 5 nM nitrate by a light absorption detection at 520 and 620nm.[203] Fluorescence-based methods typically also very sensitive and used as measurement of the optical response of molecules upon reaction with nitrite. By synthesizing the complex molecule of TMABODIPY[204] and optimizing the reaction conditions, as low as 8-300 nM linear calibration range was achieved for nitrite.

In order to avoid complex synthesis or purchase of expensive fluorescent molecules, but still harvesting the sensitivity of fluorescence methods, we explored the yet less discovered area by using carbon dots (C-dots) as NO_2^- ion sensors.[205-210] Since nitrite ion sensors often bear amino

groups[189,201,203,204,211] as reactive or responding sites, we focused on the amine-capped C-dots, therefore we used the cheap and abundant *p*-phenylenediamine (pPD) as an amine rich precursor for the synthesis of fluorescent C-dots (chapter 5.1). It can be stabilized in acidic water and excited by visible blue light, which results a PL emission in the green region. This property also makes possible the use of cheap plastic cuvettes instead of the expensive and fragile quartz-made ones (possibly even for onsite measurements). Its excitation maxima at 470 nm correlates to the most intense region of a xenon lamp and several LED sources altogether with an intense range of sunlight.[212]

C-dots often exhibit PL quenching in the present of specific ions, therefore, common ions of natural water and some expected problematic contaminant[213-215] (heavy metal ions) must have been tested for possible effects on PL and their interference have been minimized.

5.2.2. Experimental

Chemicals and reagents

p-phenylenediamine (pPD)	Aldrich, 98%
sulfuric acid	Carlo Erba, 96%
sodium nitrite	Alfa Aesar, 98%
sodium chloride	Aldrich, >99%
potassium chloride	Aldrich, >99%
calcium chloride	Molar Chemicals, a.r.
potassium nitrate	Carlo Erba, >99%
magnesium sulfate	Molar Chemicals, a.r.
sodium sulfate	Molar Chemicals, a.r.
ammonium sulfate	Molar Chemicals, a.r.
iron(II) sulfate heptahydrate	Aldrich, >99%
iron(III) sulfate hydrate	Alfa Aesar, 98%
copper sulfate pentahydrate	Aldrich, >99%
chromium(III) chloride hexahydrate	Aldrich, 96%
lead chloride	Aldrich, >99%
nickel chloride hexahydrate	Aldrich, 99.9%
ethanol (EtOH)	Carlo Erba, 99.9%
ethyl acetate (EtOAc)	Alfa Aesar, 99%

In-site produced Milli-Q water was utilized for aqueous solutions.

The chemicals were used without further purification.

Synthesis of carbon dots

The ethanolic C-dots reaction mixture reported in chapter 5.1 was used as starting material.

Preparation of stock solutions

0.50 mL of concentrated sulfuric acid was added to 49.00 mL of stirred water than 0.50 mL of crude ethanolic C-dots solution was dropped into it. Upon mixing, a red solution was obtained. Alternatively, 14.6 g of sodium chloride (for 50 mL 5M concentration) may also be added during the preparation of the 50 mL solution.

Sample preparation

2.00 mL of nitrite containing aqueous sample was mixed with 0.50 ml stock solution in a polystyrene fluorescence cuvette with an optical path of 1.00 cm and analyzed after allowing 15 minutes reaction time at ambient temperature. Typically, the same sample was used for photoluminescence and UV-Vis measurements.

Standard method for nitrite detection (Griess test - in cooperation)

According to the Italian National Institute of Health's method, the nitrite ions concentration was photometrically determined, staining the samples with a mixture of sulfanilamide and N-(1-naphthyl)-ethylenediamine (NEDA) in an acidic medium. Thus, 1 mL of sulfanilamide was added to 50 mL of water sample. Successively (3 minutes elapsed), 1 ml of NEDA was added. After 15 minutes, the absorbance at 543 nm was measured using a molecular absorption spectrophotometer (Perkin-Elmer model 550 S), placing the sample in glass cuvettes with an optical path of 1.00 cm.[216]

5.2.3. Results and discussion

The used C-dots were synthesized by a reported solvothermal method[86] (discussed in chapter 5.1.) by utilizing pPD and different solvents. The reported ethanolic synthesis turned out to be the most suitable, since only this crude product was homogenous and miscible with either water or acidified water, therefore in this case no further purification was necessary before optical tests. The obtained mixture of C-dots and synthesis by-products (altogether: crude C-dots) bear abundant aromatic amines (chapter 5.1), which makes possible to use them as nitrite ion sensors via diazotization/decomposition steps at room temperature (**figure 52.1)**.[217]

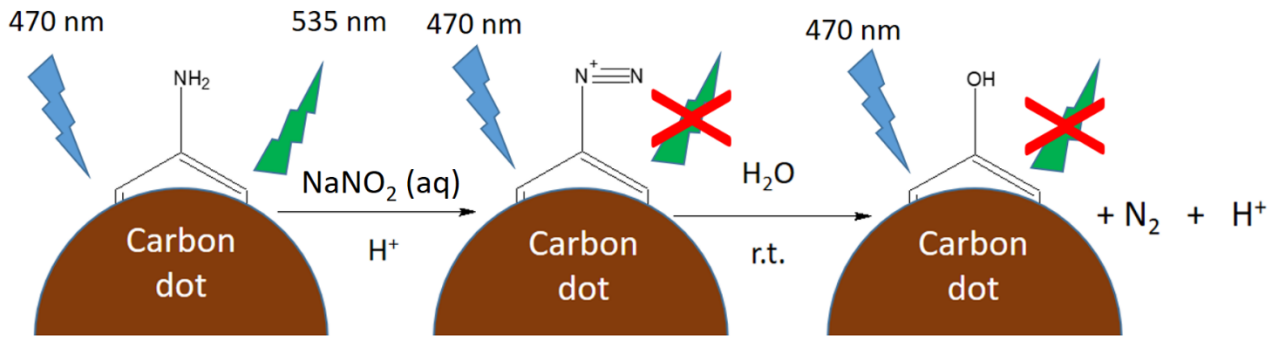

Figure 52.1 displays the expected reaction of (aromatic) amino-capped carbon dots as undergoing diazotization and decomposition in acidic aqueous conditions at ambient temperature with illustration of losing their fluorescence in the presence of nitrite ions.

The stock solution's sulfuric acid in situ generates the nitrous acid from the added nitrite ions, which leads to the formation of diazonium salts. These salts, due to their thermal instability, typically synthesized at low temperature and immediately used for azo-coupling, but in our case, room temperature reactions were also suitable, since the reaction (and slow decomposition) generally changes the PL-properties of the C-dots' solution, therefore makes optical nitrite quantification possible. Because of the simpleness of the analysis, the effect of the possible azo coupling with other reagents (eg. Griess test) was not explored.

The ethanolic C-dots solution kept its optical properties at least up to 2 months at room temperature, but for our purposes, the acidic aqueous samples were more appropriate for the nitrite quantification measurements, as it can also contain all the necessary reagents and additives in one stock solution, which at the end, only requires the addition of the water sample to be analyzed. Interestingly, the C-dots' acidic solution (1% sulfuric acid) showed remarkable PL stability up to at least 6 weeks at room temperature (chapter 5.1**)**, however, addition of the nitrite ions results significant change in appearance as turning the color of the solution from pink to light yellow (**figure 52.2**). This effect may be applied for simple colorimetric determination by bare eyes at higher concentration, while analysis of the gradual change in UV-Vis (at 353 nm, not investigated further) and PL properties lead to more precise determination (**figure 52.8**).

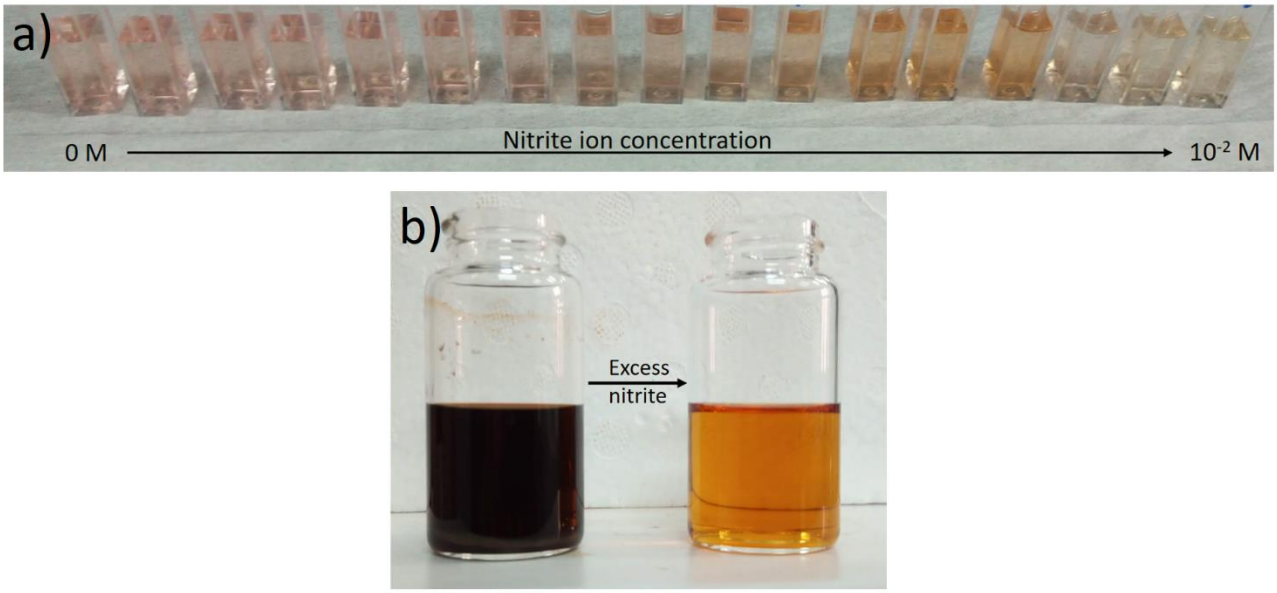

Figure 52.2. shows the color change of C-dots in 1% sulfuric acid upon treating with increasing amount of nitrite ions (up) and a more concentrated, acidic C-dots solution before and after treating it with excess nitrite (bottom).

Photoluminescence

Comparison of the 3D PL maps of crude C-dots diluted in water, in 1% aqueous sulfuric acid and after reaction with nitrite (**figure 52.3**) reveals that using diluted sulfuric acid as solvent approximately doubles the peak PL-intensity (under same conditions), while the maximum emission shifts from 605 nm to 535 nm, which wavelength serves as optimal parameter for detection. The addition of excess amount of nitrite switches off the photoluminescence. It must be noted, that pPD alone in 1% sulfuric acid and its nitrite treated solution did not show any photoluminescence in the examined visible region (while stock solutions' C-dots and the pPD concentrations were equal: starting from 108 mg/10mL ethanolic solutions-not illustrated here).

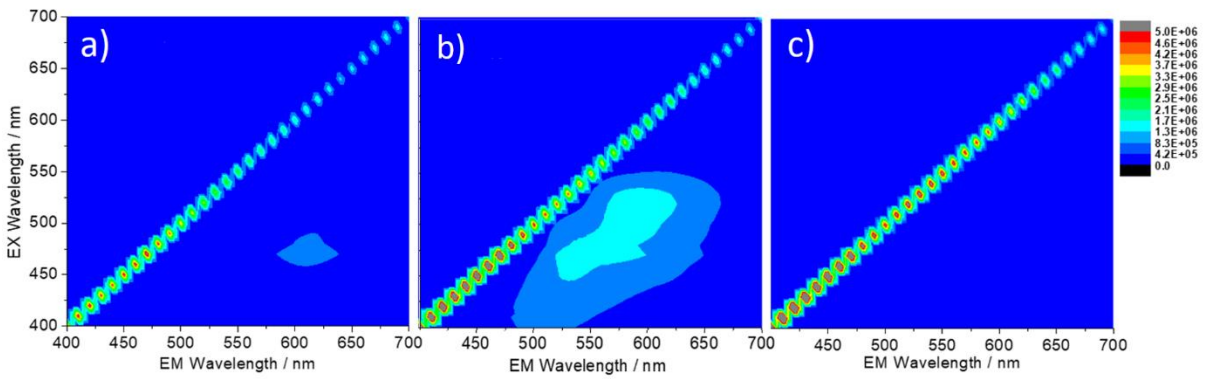

Figure 52.3. shows the 3D PL map (excitation/y-axis and emission/x-axis, false color scale) of the crude C-dots solution diluted by water (a) or 1% sulfuric acid (b). Treatment of acidic solution with nitrite ions results quenched PL (c). All 3D maps apply the same color scaling (see next to figure).

The reaction takes place at room temperature in 10-15 minutes, which can be monitored by a spectrofluorimeter at the peak intensity. The curve indicates an exponential decay (**figure 52.4**).

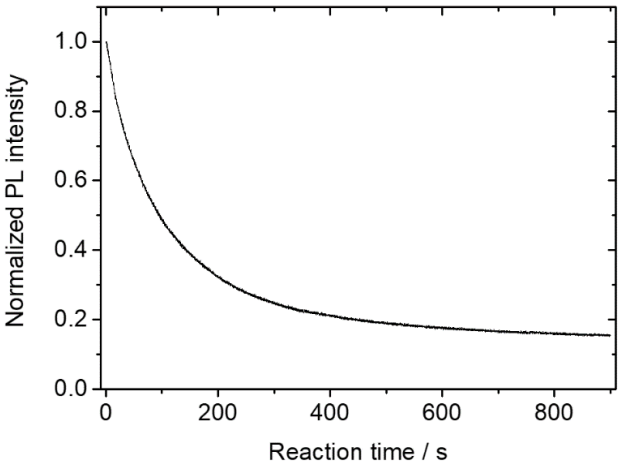

Figure 52.4. Normalized PL intensity change due to the C-dots' reaction with nitrite ions (100 μM) in acidic medium up to 15 minutes (excitation at 470 nm, emission at 535 nm).

UV-Vis

Spectra of pPD, C-dots and nitrite treated C-dots were investigated and plotted in **figure 52.5**. The addition of nitrite significantly changes the main absorption bands in the 200-400 nm region (**figure 52.5a**). While the π–π* and n-π* assigned peaks at 220 and 280 nm of the C-dots seem unchanged (same dilution of C-dots), the peak around 500 nm, which was assigned to the surface groups transition,[86] shifted to 480 nm and became more intense. Additionally, two very intense peaks appeared at 250 and 350 nm. The latter two peaks may be explained by the reaction of residual molecular pPD or relatively small proto C-dots since pure pPD treated with nitrite under the same conditions reproduced those absorption bands (**figure 52.5b**). The obvious difference is the lack of absorption over 400 nm in the case of pPD, which clearly indicates, that the examined photoluminescence at 535 nm originates from the visual light (>400 nm) absorption of C-dots and not from the still molecular impurities. Since this region of absorbance is associated with the C-dots surface groups (chapter 5.1) and only those groups are available for a chemical reaction, thus we can say this nitrite detection method also revealed that the examined photoluminescence of this type of C-dots exclusively originates from the surface groups (amines).

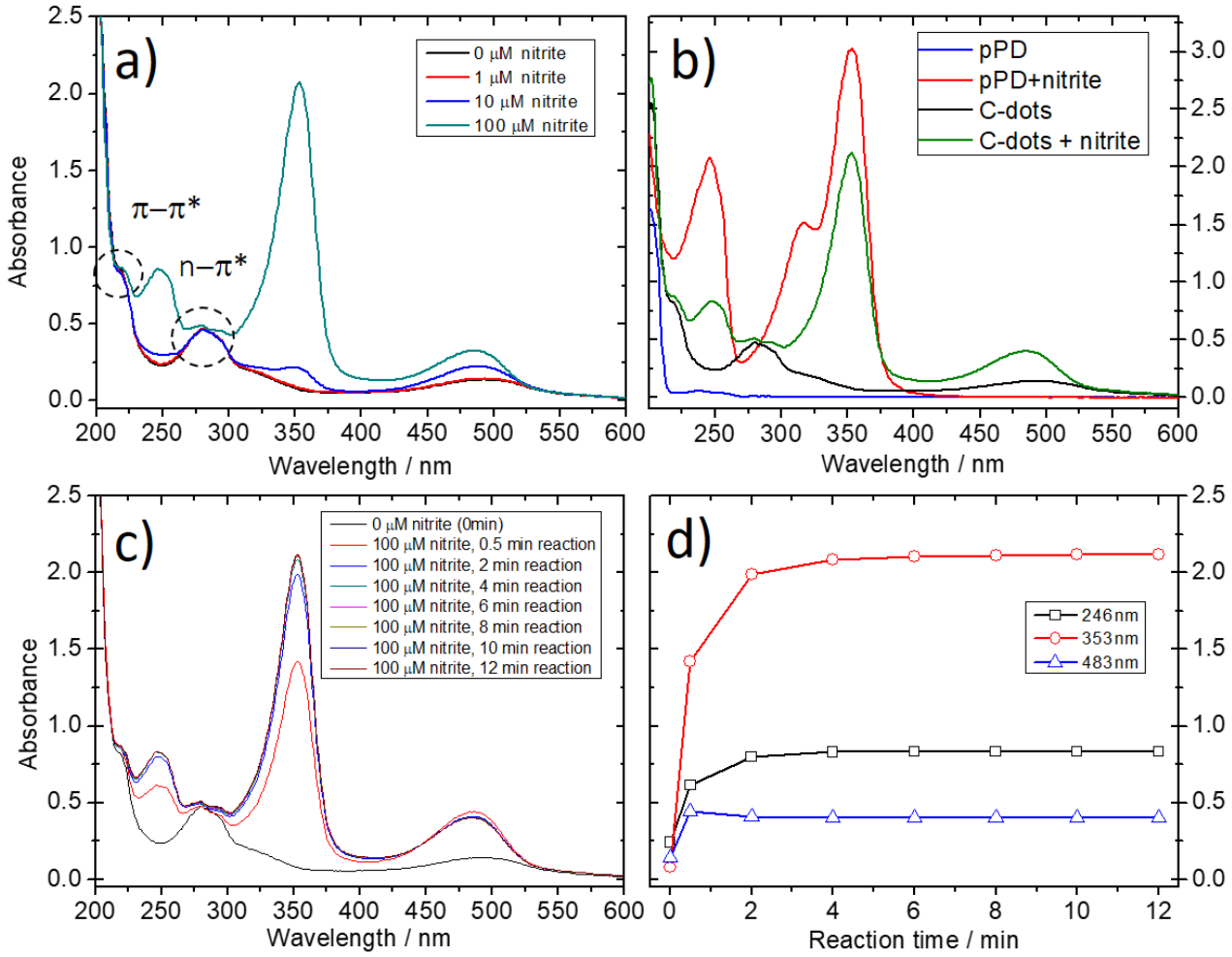

Figure 52.5 shows the UV-Vis spectra of the crude C-dots dissolved in 1% aqueous sulfuric acid and treated with various amount of nitrite ions (0-100 μM). Characteristic bands of C-dots (assigned for π–π* and n-π* transitions) remain unchanged, while chemical reaction on the C-dots surface leads to the emerge of new intense absorption bands (a). To have a clearer picture of the change in optical properties, the behavior of molecular pPD under the same acidic condition and its reaction with nitrite ions were also analyzed and displayed together with the C-dots (b) to reveal that the different behavior restricts to the range of 450-550 nm. The C-dots reaction was also investigated through time up to 12 min (c) and intensity change of the characteristic absorption bands were also plotted (d).

The formation of the new peaks was followed by measuring a sample at different reaction times after addition of nitrite up to 12 minutes (**figure 52.5cd**). Interestingly, the UV-Vis data suggest that the reaction completes in 2-3 minutes, while photoluminescence measurements (excitation at 470 nm, **figure 52.4**) indicates slower (10-15 min) reaction course (compare with **figure 52.5d**). Additionally, even the relevant absorbance band at 483nm increases and seemingly stabilizes in 2 minutes reaction time (**figure 52.5d**), while PL emission quenching (at 535 nm) clearly showing the continuous decrease of fluorescence up to 12-15 minutes. More detailed analysis of the absorption change at 483nm during the reaction, revealed a sudden jump and a slow decrease in absorption,

which correlates well to the PL decay through the reaction (**figure 52.5d**-blue line and **figure 52.6**). This result associate the PL emission peaking at 535 nm with only a very small decrease in absorbance, peaking at 483nm and further confirming the change in the surface groups due a slow chemical reaction.

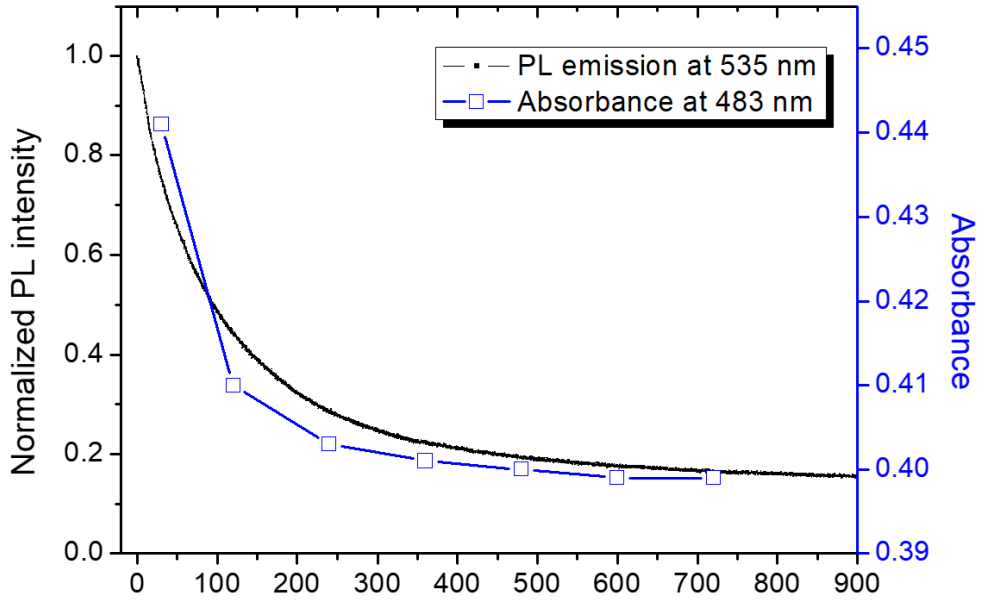

Figure 52.6. Parallel trends of PL emission decay observed at 535 nm (black line) and the absorbance at 483 nm (blue line) during the reaction of C-dots with nitrites. The data of PL plotted from 0 s, while absorbance displayed from 30 s reaction time. The blue line is only guide for the eyes.

FTIR results

Three materials were compared in **figure 52.7**. The dried crude C-dots, pPD as its precursor and the nitrite treated sample, which was obtained by using C-dots in acidic aqueous ethanol at high concentration and treated with excess nitrite for 1h at room temperature. The obtained dark yellow solution (**figure 52.2b**) was neutralized by gradual addition of solid Na_2CO_3, then it was 5x diluted with water and 5x extracted with ethyl acetate. The united organic phase was dried over $MgSO_4$, filtered, concentrated under reduced pressure and kept at 60^{o}C for 24h.

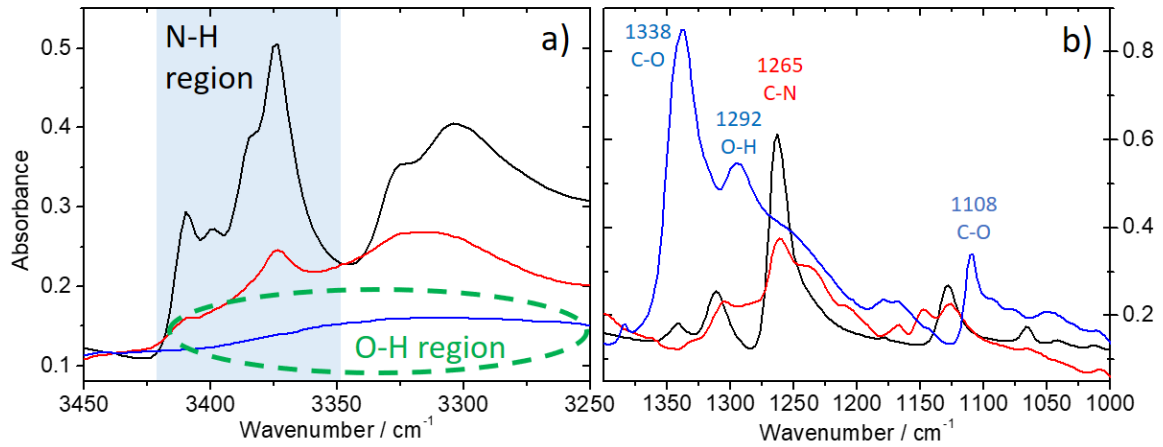

Figure 52.7. Selected regions of FTIR spectra of the precursor (pPD/black), the crude (red) and nitrite-treated C-dots (blue) in the region of the broad O-H and N-H-signals (a) and some identified signals of aromatic amines and phenolic –OH groups confirming the expected reaction of the nitrite sensing (b).

Characteristic peaks of the pPD's N-H signals between 3420 and 3350 cm^{-1} are still noticeable on the crude C-dots' spectrum, while absent on the nitrite treated sample's spectrum. Instead, a wide, but not so intense peak observed between 3400 and 3150 cm^{-1}, which we assigned to phenolic O-H, probably overlapping with residual N-H signals. The region between 1400 and 1000 cm^{-1} also clearly indicates the chemical change. Disappearance of the C-N assigned peak[218] of the pPD and the C-dots at 1265 cm^{-1} and emerge of C-O (1338 and 1108 cm^{-1}) and O-H (1292 cm^{-1})[219,220] also proves the reaction path of nitrite detection.

Calibration for nitrite detection

Freshly prepared nitrite solutions in the range of 10 mM to 1 nM made from solid $NaNO_2$ by dissolution in water and through several dilution. The analyzed samples were prepared in the cuvettes by mixing 2.00 ml of nitrite solution with 0.50 ml of acidic C-dots solution and let to react for 15 minutes. Photoluminescence data were collected at 535 nm upon excitation at 470 nm using always the same fluorimeter settings. PL quenching can be detected even in the range of 1-20 nM, followed by a slow increase and an inconclusive region up to 5 μM where the PL intensity finally fall below the value of all the previous samples, therefore only one possible concentration can be identified from the calibration curve. Precise detection of nitrite is possible in the range of 5-200 μM with a linear range within 5-75 μM (**figure 52.8**). Probably the C-dots can offer more reactive sites in limited number, which takes another reaction path with nitrous acid and at lower nitrite concentrations as a sum of parallel reactions, therefore, first increase of PL intensity occurs, than the main reaction path turns dominant and continuous PL quenching may be observed.

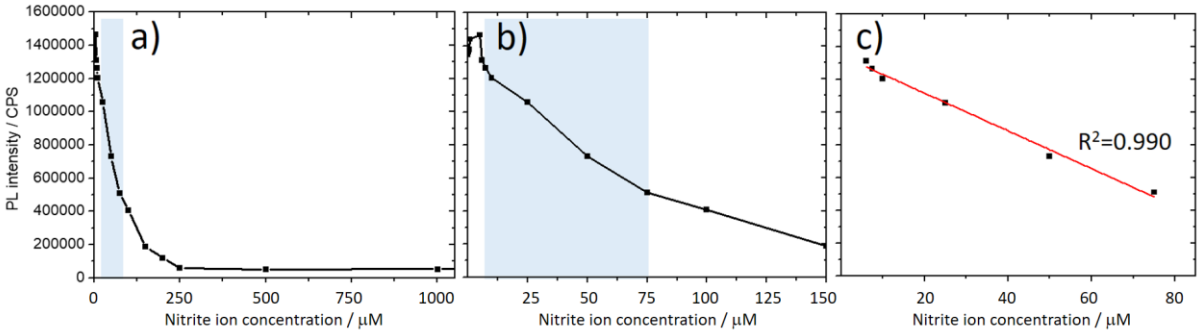

Figure 52.8 Normalized PL intensity change due to the C-dots reaction with nitrite ions at different concentrations (a,b). Linear range highlighted and fitting was applied (c).

Effects of metal ions

Carbon dots often reported as efficient sensor of different metal ions[215] through PL quenching, thus it was necessary to test the acidic C-dots solution in such media. Numerous metal ions (and their anion pairs) were tested and the data summarized in **table 52.1**.

Salt (**A series**):	None	1M $CaCl_2$	1M NaCl	1M KCl	1M KNO_3	1M $MgSO_4$	1M Na_2SO_4	1M $(NH4)_2SO_4$
Normalized PL-intensity:	1	0.961	0.999	1.024	1.021	0.978	0.933	0.912
Salt (**B series**):	None	0.1M $FeSO_4$	0.01M $FeSO_4$	0.1M $Fe_2(SO_4)_3$	0.01M $Fe_2(SO_4)_3$	0.005M $Fe_2(SO_4)_3$	0.1M $CuSO_4$	0.01M $CuSO_4$
Normalized PL-intensity:	1	0.826	0.951	0.335	0.805	0.852	0.440	0.845
Salt + 1M NaCl (**C series**):	None		0.01M $FeSO_4$			0.005M $Fe_2(SO_4)_3$		0.01M $CuSO_4$
Normalized PL-intensity:	1		0.999			0.954		0.889
Salt + 1M NaCl (**D series**):	None	0.01M $CrCl_3$	0.001M $CrCl_3$	0.01M $PbCl_2$	0.001M $PbCl_2$	0.01M $NiCl_2$	0.001M $NiCl_2$	
Normalized PL-intensity:	1	0.694	0.939	0.940	0.985	0.963	0.988	

Table 52.1 shows the normalized PL intensity (excitation at 470 nm, emission 535 nm) change due to the C-dots interaction with common ions in natural water at high concentration (**A series**) and some critical cations (Fe^{2+}, Fe^{3+}, Cu^{2+} at lower concentration (**B series**). The quencing effect of heavy metal cations was partially suppressed by applying high (1M) concentration of NaCl (**C series**). This method was extended (**D series**) to other heavy metal cations (Cr^{3+}, Pb^{2+}, Ni^{2+}).

Firstly, some frequently occurring ions in natural water were tested at high concentration (1M) in the "**A series**". Seemingly, those ions have no or only small effect for the PL. Especially NaCl and KCl shows excellent inertness, thus these C-dots expected to be accurate for seawater samples. Very important to point out that nitrate anions also proved to be completely inert during the analysis. However, application of the typical critical cations, such as Fe^{2+}, Fe^{3+} and Cu^{2+} resulted significant quench on PL even at 5 mM concentration. ("**B series**"). Because of the earlier proved inertness of NaCl and its common occurrence in natural water (seawater), we tried to use it as an "ionic buffer", to limit the effect of other metal ions. For this reason, NaCl (commercial table salt also efficient) was added to the acidic C-dots solution up to 5M concentration (so 5x dilution during the sample preparation results 1M NaCl). These buffered samples were treated with the same metal ions at the same concentration as before and the results listed in the "**C series**". Obviously, this approach had a positive effect (compare B and C series), so natural water samples, which are not expected to be contaminated with heavy metals can be measured by this method, the minimal effect of such ions may be masked by simply adding NaCl to the stock solution. Furthermore, even less common cations in nature were tested in the presence of sodium chloride and gave satisfactory results at 1 mM concentration and under ("**D series**").

Removal of heavy metals before analysis

Since copper(II)-ions have strong effect on PL and still used in agriculture, we decided to try an alternative sample preparation with $CuSO_4$ to solve the problem of such contamination. In this attempt first we used same volume of two $CuSO_4$ solution (0.01M) one was contaminated with known amount of nitrite, the other contained only the metal salt. Both solutions were basified by KOH solution and the resulted blue precipitate was filtered and washed (**figure 52.9**).

Figure 52.9. Copper-sulfate solution on the left, blue precipitation by adding drops of aqueous 1M KOH (middle) and after filtration by 0.22 μm syringe filter (right).

Finally, both transparent solutions were acidified by adding drops of 20% sulfuric acid and then filled up with water to exactly double the starting volume, therefore initial nitrite concentration halved and copper ions were mainly eliminated. The samples were measured for nitrite concentration, and compared to pure aqueous nitrite solutions (**table 52.2**).

	Milli-Q	Supernatant of copper(II) precipitate
0 μM nitrite	1	0.949
50 μM nitrite	0.475	0.451

Table 52.2: Normalized PL intensities (excitation at 470 nm, emission 535 nm) after water samples treated for copper ion removal by precipitation under basic conditions, filtered and the supernatant washed and acidified. The samples are exactly double diluted as a result of the treatment. All samples (with or without nitrite) underwent the same procedure.

Similar relative PL intensity results obtained. This method seems suitable for contaminated water samples. Other heavy metals also form precipitates in basified water, however fine tuning of pH is necessary.[221]

Testing on natural and urban water samples

Water samples were collected from Russia and Hungary for this set of experiments. None of them showed detectable nitrite by this method, therefore same amount of contaminant was added to each sample (and to Milli-Q water as reference). The result (**table 52.3**) indicates that different water samples (tap-, ground-, river- and seawater) can provide very similar results.

Water source	Milli-Q	Neva river, St. Petersburg, Russia	Moscow river, Moscow, Russia	Baltic Sea, St. Petersburg, Russia	Groundwater, Gyál, Hungary	Tapwater, Gyál, Hungary
0 μM nitrite	1	0.988	0.972	1.007	1.020	0.992
80 μM nitrite	0.278	0.279	0.274	0.276	0.267	0.268

Table 52.3 shows the normalized PL intensity (excitation at 470 nm, emission 535 nm) change due to the C-dots interaction with natural/urban waters with or without adding same amount of nitrite ions.

Comparison with a standard method

A natural water sample was collected from the Bay of Tramariglio (Sardinia, Italy) and half of it was contaminated by unknown amount of $NaNO_2$ by our colleague. The samples were analyzed by this present method and in a certified laboratory for water analysis at the University of Sassari. The results are summarized in **table 52.4**.

Tramariglio (Italy) seawater	Measured nitrite concentration	Measured nitrite concentration after nitrite was added
Present method	<0.23 mg/L (<5 μM)	0.46 mg/L (9.9 μM)
Griess method	<0,005 mg/L (<0.1 μM)	0.46 mg/L (10.0 μM)

Table 52.4. Measured nitrite ion concentrations in natural seawater by the presented C-dots and compared to the standard Griess-method (nitrite was not detected). The measurements were repeated after the same sample was contaminated with nitrites.

It was not possible to detect nitrite ions by these methods in the pure sample and the contaminated sample gave similar results.

5.2.4. Conclusions

Amine-capped C-dots, prepared by a solvothermal method from *p*-phenylenediamine were used as obtained (chapter 5.1) for nitrite ion detection at ambient temperature in the visible light range. The particles surface (aromatic) amine groups undergo a reaction with nitrite ions in acidic aqueous media to form diazonium salts, which results a gradual change in light absorbance and PL emission. The relevant absorption band and the PL emission peak successfully associated to the surface states and to their chemical modification. Common inorganic contaminants were also added in some measurements and their influence on nitrite sensing were either negligible or could be minimized by appropriate sample preparation, therefore a linear correlation of PL quenching and the nitrite ion concentration was established in the range of 5-75 μM (in aqueous samples). The method makes use of 470 nm light, therefore plastic cuvettes and even a natural light source may be applied, which makes possible a simple on-site detection of nitrites. The detection limit does not exceed other C-dots based nitrite ion sensors, but further improvement in sensitivity still could be gained by improving the synthetic method in aspect of obtaining stronger fluorescence, as the optical spectra (UV-Vis, IR) suggest that non-fluorescent, small molecular precursors are still abundantly present in the sample.

Conclusions

For the present thesis, I have performed experimental work related to three well separated topics, which were numbered as chapters 3, 4 and 5.

As a first step (chapter 3), I conducted a set of experiments by using the citric acid – Tris model system and reacted them by applying common synthetic approaches, such as microwave assisted reactions in a household MW oven and in a laboratory MW reactor, furthermore, the pyrolysis of the components were also tested by using an initial solvent to dissolve the precursors, or just simply running a reaction in their molten state. Additionally, the common hydrothermal method was also tested. The experiments clearly indicated, that the best results (most intense PL in the shortest reaction) can be achieved by the simple solvent free pyrolysis method, therefore this approach was used for almost all of the later reactions to obtain C-dots. In the same experiment setting, the molar ratio of the precursors (citric acid and Tris) was also varied and the products exhibited different PL properties (by intensity and emission bands). Therefore, a thorough investigation of citric acid based C-dots was performed: pyrolysis of citric acid (chapter 4.1), pyrolysis of citric acid and Tris at its optimized ratio (chapter 4.2 as an extension of chapter 3) and the formation of C-dots from citric acid and urea (chapter 4.3).

In chapter 4 I focused on the better understanding of the formation and emission properties of fluorescent carbon dots made by using citric acid as least one of the precursors in their bottom-up syntheses. The study on purely citric acid based C-dots (chapter 4.1) revealed the correlation of the experienced photoluminescence and the appearance of different pyrocitric acids during the thermal degradation process, most importantly, the *trans*-aconitic acid, as an identified possible fluorophore in the overall emission of the obtained C-dots. We also proved that the intermediates alone are also possible sources of fluorescent C-dots. The main emission band of citric acid C-dots is at 500 nm, which, upon surface functionalization with APTES, due to the formation of a silica protective layer, exhibits a 90 nm blue shift and its stability in water greatly increases. These findings makes possible to use such C-dots in sol-gel methods and extending their storage time in aqueous solutions from days to months.

Investigation of the citric acid - Tris based C-dots (chapter 4.2), produced at the molar ratio of 3/1 revealed the formation of polymeric structures through amide and ester bonds and their intensity on the FTIR spectra was in correlation with the experienced PL emission intensity. Very intense PL was observed from 1/1 to 5/1 precursor ratios, while its variation significantly influenced

the products' water solubility. Functionalization with APTES did not cause shift in the PL emission, however its intensity was enhanced.

Citric-acid urea based C-dots (chapter 4.3) exhibit a peculiar dual emission in the blue and the green region. Upon changing the precursor ratio from 2/1 to 1/8 and varying the reaction time, these band intensities might be tuned. At extreme precursor ratios (less and most urea in the reaction mixture) almost "clean" blue or green emission can be obtained. The formation of citrazinic acid is responsible for the blue, and the molecule called HPPT for the green emission. HPPT may be formed by the reaction of citrazinic acid with the isocyanic acid released during the decomposition of urea, such as citrazinic acid supposedly forms by the reaction of *trans*-aconitic acid (from the pyrolysis of citric acid) with the ammonia released from urea at high reaction temperatures. Functionalization with APTES revealed that the blue band does not shift, but simultaneously the interaction with APTES switching off the green emission, proving that HPPT mainly positioned on the surface of the C-dots (or dissolved as molecules).

The citric acid based C-dots (and their APTES modified derivatives) were co-precipitated with titanium tetraisopropoxide in a simple procedure (chapter 4.4). The filtered and dried hybrid C-dots/TiO_2 samples were tested in a photocatalytic experiment, by decomposing Rhodamine B under direct sunlight. The experiment showed that APTES modified C-dots do not enhance the photocatalytic activity of titania, on the contrary, they hinder the process. The bare C-dots performed better, but none of them could outperform pure titania. Further optimization is needed to find the appropriate way to use the synthesized C-dots as photosensitizers for titania.

To further cover the visible spectrum by emitting C-dots, after obtaining strong emission at 410, 450 and 520 nm wavelengths by the citric acid based C-dots, I explored the possibility to synthetize *p*-phenylenediamine based particles in solvothermal reactions (chapter 5.1), yielding crude products with PL emission at 605 nm in ethanol and at 535 nm in 1% sulfuric acid. The use of acid greatly enhances the PL stability of the samples through months, while it is completely lost in a matter of days upon storing in water. Functionalization was performed by 3-(triethoxysilyl)propyl isocyanate, forming a covalent bond with the surface amino groups, which, similarly to the citric acid based C-dots, resulted an 80 nm blue shift in the PL emission.

In chapter 5.2 the *p*-phenylenediamine based amino-capped carbon dots, as exhibiting good stability in acidic media, found to be an excellent candidate for nitrite ion sensing via a diazotization reaction, which resulted a nitrite ion concentration dependent PL quenching. The method was efficient to detect and quantify nitrites in aqueous samples in the range of 5-75 μM and was tested on natural waters too.

List of acronyms

AA	aconitic acid (*cis* or *trans*), prop-1-ene-1,2,3-tricarboxylic acid
ACA	anhydrous citric acid
APTES	3-(aminopropyl)triethoxysilane
CA	citric acid
CAM	citric acid monohydrate
CDs	carbon dots
C-dots	carbon dots
CNDs	carbon nanodots
CT	citric acid-Tris
CU	citric acid-urea
DLS	dynamic light scattering
DSC	differential scanning calorimetry
EA	elemental analysis
EtOAc	ethyl acetate
EtOH	ethanol
FTIR	Fourier-transform infrared spectroscopy
GQDs	graphene quantum dots
HPLC	high pressure/performance liquid chromatography
IR	infrared
MW	microwave
NHE	normal (or standard) hydrogen electrode
PL	photoluminescence
pPD	*p*-phenylenediamine
QY	quantum yield
TEM	transmission electron microscopy
TGA	thermogravimetric analysis
TLC	thin layer chromatography
Tris	2-amino-2-(hydroxymethyl)propane-1,3-diol
UV-Vis	ultraviolet-visible

List of publications

Carbonaro C.M, Thakkar SV, **Ludmerczki R**, Olla C, Pinna A, Loche D, Malfatti L, Marincola F.C, Casula MF, How porosity affects the emission of fluorescent carbon dot-silica porous composites, *Microporous and Mesoporous Materials,* **2020**, 305, 110302
DOI: 10.1016/j.micromeso.2020.110302
Reference[138]

Mura S, Stagi L, Malfatti L, Carbonaro C.M, **Ludmerczki R**, Plinio Innocenzi P, Modulating the Optical Properties of Citrazinic Acid through the Monomer-to-Dimer Transformation, *Journal of Physical Chemistry A*, **2020**, 124, 197-203
DOI: 10.1021/acs.jpca.9b10884
Reference[130]

Mura S, **Ludmerczki R**, Stagi L, Garroni S, Carbonaro C.M, Ricci P.C, Casula M.F, Malfatti L, Innocenzi P, Integrating sol-gel and carbon dots chemistry for the fabrication of fluorescent hybrid organic-inorganic films, *Scientific Reports*, **2020**, 10, 4770
DOI: 10.1038/s41598-020-61517-x
Reference[119]

Ludmerczki R, Mura S, Carbonaro C.M, Mandity I.M, Carraro M, Senes N, Garroni S, Granozzi G, Calvillo L, Marras S, Malfatti L, Innocenzi P, Carbon Dots from Citric Acid and its Intermediates Formed by Thermal Decomposition, *Chemistry - A European Journal*, **2019**, 25, 11963-11974
DOI: 10.1002/chem.201902497
Reference[88]

Acknowledgements

First and foremost, I owe many thanks to my supervisor, Prof. Luca Malfatti (University of Sassari) for the PhD student position and his continuous advice, education, caring and great support! The thesis would not be possible without his help, encouragement and a free seat in his car. Banzai!

I also would like to thank to Prof. Plinio Innocenzi (University of Sassari) for gently supervising and guiding my research and offering me his patience and teachings of writing. A modern polymath or a Renaissance man?

Great great thanks to my dear friend, Dr. Stefania Mura (University of Sassari) for guiding my first steps in the laboratories and to fruitfully exchange ideas about research. Surely one of the most friendly and helpful person I have ever met! Also the one and only of my Italian colleagues who drives an Italian car! Forza Fiat! (I also drive a Fiat in Hungary!)

I am grateful to Dr. Marco Faustini (Sorbonne/Pierre and Marie Curie University, Paris) for giving me the great opportunities for working in their laboratories.

I wish to thank to Dr. Laura Borgese at the Smart Solutions s.r.l. in Brescia, and Dr. Ivano Alessandri for the very interesting collaboration with the University of Brescia.

Thanks so much to my colleagues: Dr. Yu Jiang, Junkai Ren and Dr. Luigi Stagi (LMNT laboratory, University of Sassari) and Prof. Maria Francesca Casula, Prof. Carlo Maria Carbonaro and Dr. Swapneel Thakkar (University of Cagliari) for their collaborations.

A great thanks to my family for all their love and support and special thanks to my chemistry teachers through my life: Zoltán Gyócsi, Piroska Ütő, Károly Krekács and Ferenc Trischler.

The generous support from Gábor Krajsovszky and István M. Mándity (former and present directors of Department of Organic Chemistry at the Semmelweis University, Budapest, Hungary) for allowing me to participate in this PhD program is also highly appreciated.

I would like to thank to the referees of the present thesis: Prof. Fabrizio Messina (University of Palermo) and Prof. Kazumasa Suzuki (University of Shiga Prefecture) for their important recommendations and for the arised additional questions, which helped me to improve the thesis.

This presented work was possible due to the enthusiastic work and support of the doctoral school of chemical sciences and technologies in the joint program of the Universities of Cagliari and Sassari, with the always-helpful assistance of Prof. Stefano Enzo, and of course, by the financial support from the European Union and the Region of Sardinia.

Finally, thank you Alghero and Sardinia for being the most beautiful corner of the Word!

Gyál, Hungary, May 2020. Róbert Ludmerczki

Bibliography

(1) Xu, X.; Ray, R.; Gu, Y.; Ploehn, H. J.; Gearheart, L.; Raker, K.; Scrivens, W. A. Electrophoretic analysis and purification of fluorescent single-walled carbon nanotube fragments. *J Am Chem Soc* **2004,** *126* (40), 12736.

(2) Hutton, G. A. M.; Martindale, B. C. M.; Reisner, E. Carbon dots as photosensitisers for solar-driven catalysis. *Chem Soc Rev* **2017,** *46* (20), 6111.

(3) Wang, J.; Qiu, J. A review of carbon dots in biological applications. *Journal of Materials Science* **2016,** *51* (10), 4728.

(4) Lim, S. Y.; Shen, W.; Gao, Z. Carbon quantum dots and their applications. *Chem Soc Rev* **2015,** *44* (1), 362.

(5) Tuerhong, M.; Xu, Y.; Yin, X.-B. Review on Carbon Dots and Their Applications. *Chinese Journal of Analytical Chemistry* **2017,** *45* (1), 139.

(6) Geys, J.; Nemmar, A.; Verbeken, E.; Smolders, E.; Ratoi, M.; Hoylaerts, M. F.; Nemery, B.; Hoet, P. H. Acute toxicity and prothrombotic effects of quantum dots: impact of surface charge. *Environ Health Perspect* **2008,** *116* (12), 1607.

(7) Wang, R.; Lu, K.-Q.; Tang, Z.-R.; Xu, Y.-J. Recent progress in carbon quantum dots: synthesis, properties and applications in photocatalysis. *Journal of Materials Chemistry A* **2017,** *5* (8), 3717.

(8) Farshbaf, M.; Davaran, S.; Rahimi, F.; Annabi, N.; Salehi, R.; Akbarzadeh, A. Carbon quantum dots: recent progresses on synthesis, surface modification and applications. *Artif Cells Nanomed Biotechnol* **2018,** *46* (7), 1331.

(9) Georgakilas, V.; Perman, J. A.; Tucek, J.; Zboril, R. Broad family of carbon nanoallotropes: classification, chemistry, and applications of fullerenes, carbon dots, nanotubes, graphene, nanodiamonds, and combined superstructures. *Chem Rev* **2015,** *115* (11), 4744.

(10) Ding, C.; Zhu, A.; Tian, Y. Functional surface engineering of C-dots for fluorescent biosensing and in vivo bioimaging. *Acc Chem Res* **2014,** *47* (1), 20.

(11) Zuo, J.; Jiang, T.; Zhao, X.; Xiong, X.; Xiao, S.; Zhu, Z. Preparation and Application of Fluorescent Carbon Dots. *Journal of Nanomaterials* **2015,** *2015*, 1.

(12) Yuan, F.; Li, S.; Fan, Z.; Meng, X.; Fan, L.; Yang, S. Shining carbon dots: Synthesis and biomedical and optoelectronic applications. *Nano Today* **2016,** *11* (5), 565.

(13) Gayen, B.; Palchoudhury, S.; Chowdhury, J. Carbon Dots: A Mystic Star in the World of Nanoscience. *Journal of Nanomaterials* **2019,** *2019*, 1.

(14) Zhu, H.; Wang, X.; Li, Y.; Wang, Z.; Yang, F.; Yang, X. Microwave synthesis of fluorescent carbon nanoparticles with electrochemiluminescence properties. *Chem Commun (Camb)* **2009,** (34), 5118.

(15) Liu, C.; Zhang, P.; Tian, F.; Li, W.; Li, F.; Liu, W. One-step synthesis of surface passivated carbon nanodots by microwave assisted pyrolysis for enhanced multicolor photoluminescence and bioimaging. *Journal of Materials Chemistry* **2011,** *21* (35), 13163.

(16) Feng, J.; Wang, W. J.; Hai, X.; Yu, Y. L.; Wang, J. H. Green preparation of nitrogen-doped carbon dots derived from silkworm chrysalis for cell imaging. *J Mater Chem B* **2016,** *4* (3), 387.

(17) Zhang, Y.; Liu, X.; Fan, Y.; Guo, X.; Zhou, L.; Lv, Y.; Lin, J. One-step microwave synthesis of N-doped hydroxyl-functionalized carbon dots with ultra-high fluorescence quantum yields. *Nanoscale* **2016,** *8* (33), 15281.

(18) Zhang, B.; Liu, C.-y.; Liu, Y. A Novel One-Step Approach to Synthesize Fluorescent Carbon Nanoparticles. *European Journal of Inorganic Chemistry* **2010,** *2010* (28), 4411.

(19) Pang, Y.; Gao, H.; Wu, S.; Li, X. Facile synthesis the nitrogen and sulfur co-doped carbon dots for selective fluorescence detection of heavy metal ions. *Materials Letters* **2017,** *193*, 236.
(20) Shen, J.; Shang, S.; Chen, X.; Wang, D.; Cai, Y. Facile synthesis of fluorescence carbon dots from sweet potato for Fe(3+) sensing and cell imaging. *Mater Sci Eng C Mater Biol Appl* **2017,** *76*, 856.
(21) Zhang, M.; Zhao, X.; Fang, Z.; Niu, Y.; Lou, J.; Wu, Y.; Zou, S.; Xia, S.; Sun, M.; Du, F. Fabrication of HA/PEI-functionalized carbon dots for tumor targeting, intracellular imaging and gene delivery. *RSC Advances* **2017,** *7* (6), 3369.
(22) Martindale, B. C.; Hutton, G. A.; Caputo, C. A.; Reisner, E. Solar hydrogen production using carbon quantum dots and a molecular nickel catalyst. *J Am Chem Soc* **2015,** *137* (18), 6018.
(23) Guo, Y.; Zhang, L.; Cao, F.; Leng, Y. Thermal treatment of hair for the synthesis of sustainable carbon quantum dots and the applications for sensing Hg(2). *Sci Rep* **2016,** *6*, 35795.
(24) Rong, M.; Feng, Y.; Wang, Y.; Chen, X. One-pot solid phase pyrolysis synthesis of nitrogen-doped carbon dots for Fe3+ sensing and bioimaging. *Sensors and Actuators B: Chemical* **2017,** *245*, 868.
(25) Yu, S. J.; Kang, M. W.; Chang, H. C.; Chen, K. M.; Yu, Y. C. Bright fluorescent nanodiamonds: no photobleaching and low cytotoxicity. *J Am Chem Soc* **2005,** *127* (50), 17604.
(26) Sun, Y. P.; Zhou, B.; Lin, Y.; Wang, W.; Fernando, K. A.; Pathak, P.; Meziani, M. J.; Harruff, B. A.; Wang, X.; Wang, H.et al. Quantum-sized carbon dots for bright and colorful photoluminescence. *J Am Chem Soc* **2006,** *128* (24), 7756.
(27) Zhou, J.; Booker, C.; Li, R.; Zhou, X.; Sham, T. K.; Sun, X.; Ding, Z. An electrochemical avenue to blue luminescent nanocrystals from multiwalled carbon nanotubes (MWCNTs). *J Am Chem Soc* **2007,** *129* (4), 744.
(28) Liu, H.; Ye, T.; Mao, C. Fluorescent carbon nanoparticles derived from candle soot. *Angew Chem Int Ed Engl* **2007,** *46* (34), 6473.
(29) Dong, Y.; Zhou, N.; Lin, X.; Lin, J.; Chi, Y.; Chen, G. Extraction of Electrochemiluminescent Oxidized Carbon Quantum Dots from Activated Carbon. *Chemistry of Materials* **2010,** *22* (21), 5895.
(30) Sharma, A.; Das, J. Small molecules derived carbon dots: synthesis and applications in sensing, catalysis, imaging, and biomedicine. *J Nanobiotechnology* **2019,** *17* (1), 92.
(31) Li, H.; He, X.; Kang, Z.; Huang, H.; Liu, Y.; Liu, J.; Lian, S.; Tsang, C. H.; Yang, X.; Lee, S. T. Water-soluble fluorescent carbon quantum dots and photocatalyst design. *Angew Chem Int Ed Engl* **2010,** *49* (26), 4430.
(32) Donate-Buendia, C.; Torres-Mendieta, R.; Pyatenko, A.; Falomir, E.; Fernandez-Alonso, M.; Minguez-Vega, G. Fabrication by Laser Irradiation in a Continuous Flow Jet of Carbon Quantum Dots for Fluorescence Imaging. *ACS Omega* **2018,** *3* (3), 2735.
(33) Bottini, M.; Balasubramanian, C.; Dawson, M. I.; Bergamaschi, A.; Bellucci, S.; Mustelin, T. Isolation and characterization of fluorescent nanoparticles from pristine and oxidized electric arc-produced single-walled carbon nanotubes. *J Phys Chem B* **2006,** *110* (2), 831.
(34) Dey, S.; Govindaraj, A.; Biswas, K.; Rao, C. N. R. Luminescence properties of boron and nitrogen doped graphene quantum dots prepared from arc-discharge-generated doped graphene samples. *Chemical Physics Letters* **2014,** *595-596*, 203.
(35) Dang, H.; Huang, L.-K.; Zhang, Y.; Wang, C.-F.; Chen, S. Large-Scale Ultrasonic Fabrication of White Fluorescent Carbon Dots. *Industrial & Engineering Chemistry Research* **2016,** *55* (18), 5335.

(36) Shao, T.; Wang, G.; An, X.; Zhuo, S.; Xia, Y.; Zhu, C. A reformative oxidation strategy using high concentration nitric acid for enhancing the emission performance of graphene quantum dots. *RSC Adv.* **2014,** *4* (89), 47977.
(37) Liu, M. L.; Chen, B. B.; Li, C. M.; Huang, C. Z. Carbon dots: synthesis, formation mechanism, fluorescence origin and sensing applications. *Green Chemistry* **2019,** *21* (3), 449.
(38) Liu, M.; Xu, Y.; Niu, F.; Gooding, J. J.; Liu, J. Carbon quantum dots directly generated from electrochemical oxidation of graphite electrodes in alkaline alcohols and the applications for specific ferric ion detection and cell imaging. *Analyst* **2016,** *141* (9), 2657.
(39) Hu, Q.; Gong, X.; Liu, L.; Choi, M. M. F. Characterization and Analytical Separation of Fluorescent Carbon Nanodots. *Journal of Nanomaterials* **2017,** *2017*, 1.
(40) Baker, S. N.; Baker, G. A. Luminescent carbon nanodots: emergent nanolights. *Angew Chem Int Ed Engl* **2010,** *49* (38), 6726.
(41) Emam, A. N.; Loutfy, S. A.; Mostafa, A. A.; Awad, H.; Mohamed, M. B. Cyto-toxicity, biocompatibility and cellular response of carbon dots–plasmonic based nano-hybrids for bioimaging. *RSC Advances* **2017,** *7* (38), 23502.
(42) Kim, S.; Hwang, S. W.; Kim, M. K.; Shin, D. Y.; Shin, D. H.; Kim, C. O.; Yang, S. B.; Park, J. H.; Hwang, E.; Choi, S. H.et al. Anomalous behaviors of visible luminescence from graphene quantum dots: interplay between size and shape. *ACS Nano* **2012,** *6* (9), 8203.
(43) Li, X.; Lau, S. P.; Tang, L.; Ji, R.; Yang, P. Sulphur doping: a facile approach to tune the electronic structure and optical properties of graphene quantum dots. *Nanoscale* **2014,** *6* (10), 5323.
(44) Bao, L.; Zhang, Z. L.; Tian, Z. Q.; Zhang, L.; Liu, C.; Lin, Y.; Qi, B.; Pang, D. W. Electrochemical tuning of luminescent carbon nanodots: from preparation to luminescence mechanism. *Adv Mater* **2011,** *23* (48), 5801.
(45) Li, Y.; Shu, H.; Niu, X.; Wang, J. Electronic and Optical Properties of Edge-Functionalized Graphene Quantum Dots and the Underlying Mechanism. *The Journal of Physical Chemistry C* **2015,** *119* (44), 24950.
(46) Adedokun, O.; Roy, A.; Awodugba, A. O.; Devi, P. S. Fluorescent carbon nanoparticles from Citrus sinensis as efficient sorbents for pollutant dyes. *Luminescence* **2017,** *32* (1), 62.
(47) Zhu, S.; Meng, Q.; Wang, L.; Zhang, J.; Song, Y.; Jin, H.; Zhang, K.; Sun, H.; Wang, H.; Yang, B. Highly photoluminescent carbon dots for multicolor patterning, sensors, and bioimaging. *Angew Chem Int Ed Engl* **2013,** *52* (14), 3953.
(48) Sun, C.; Zhang, Y.; Kalytchuk, S.; Wang, Y.; Zhang, X.; Gao, W.; Zhao, J.; Cepe, K.; Zboril, R.; Yu, W. W.et al. Down-conversion monochromatic light-emitting diodes with the color determined by the active layer thickness and concentration of carbon dots. *Journal of Materials Chemistry C* **2015,** *3* (26), 6613.
(49) Wang, R.; Wang, X.; Sun, Y. One-step synthesis of self-doped carbon dots with highly photoluminescence as multifunctional biosensors for detection of iron ions and pH. *Sensors and Actuators B: Chemical* **2017,** *241*, 73.
(50) Wang, X.; Cao, L.; Lu, F.; Meziani, M. J.; Li, H.; Qi, G.; Zhou, B.; Harruff, B. A.; Kermarrec, F.; Sun, Y. P. Photoinduced electron transfers with carbon dots. *Chem Commun (Camb)* **2009**, 3774.
(51) Krysmann, M. J.; Kelarakis, A.; Dallas, P.; Giannelis, E. P. Formation mechanism of carbogenic nanoparticles with dual photoluminescence emission. *J Am Chem Soc* **2012,** *134* (2), 747.
(52) Ray, S. C.; Saha, A.; Jana, N. R.; Sarkar, R. Fluorescent Carbon Nanoparticles: Synthesis, Characterization, and Bioimaging Application. *The Journal of Physical Chemistry C* **2009,** *113* (43), 18546.
(53) Loh, K. P.; Bao, Q.; Eda, G.; Chhowalla, M. Graphene oxide as a chemically tunable platform for optical applications. *Nat Chem* **2010,** *2* (12), 1015.

(54) Li, L.-L.; Ji, J.; Fei, R.; Wang, C.-Z.; Lu, Q.; Zhang, J.-R.; Jiang, L.-P.; Zhu, J.-J. A Facile Microwave Avenue to Electrochemiluminescent Two-Color Graphene Quantum Dots. *Advanced Functional Materials* **2012,** *22* (14), 2971.
(55) Zeng, Y.-W.; Ma, D.-K.; Wang, W.; Chen, J.-J.; Zhou, L.; Zheng, Y.-Z.; Yu, K.; Huang, S.-M. N, S co-doped carbon dots with orange luminescence synthesized through polymerization and carbonization reaction of amino acids. *Applied Surface Science* **2015,** *342*, 136.
(56) Xu, Q.; Pu, P.; Zhao, J.; Dong, C.; Gao, C.; Chen, Y.; Chen, J.; Liu, Y.; Zhou, H. Preparation of highly photoluminescent sulfur-doped carbon dots for Fe(iii) detection. *Journal of Materials Chemistry A* **2015,** *3* (2), 542.
(57) Zhou, L.; Lin, Y.; Huang, Z.; Ren, J.; Qu, X. Carbon nanodots as fluorescence probes for rapid, sensitive, and label-free detection of Hg2+ and biothiols in complex matrices. *Chem Commun (Camb)* **2012,** *48* (8), 1147.
(58) Hou, J.; Dong, G.; Tian, Z.; Lu, J.; Wang, Q.; Ai, S.; Wang, M. A sensitive fluorescent sensor for selective determination of dichlorvos based on the recovered fluorescence of carbon dots-Cu(II) system. *Food Chem* **2016,** *202*, 81.
(59) Feng, Y.; Zhong, D.; Miao, H.; Yang, X. Carbon dots derived from rose flowers for tetracycline sensing. *Talanta* **2015,** *140*, 128.
(60) Roshni, V.; Ottoor, D. Synthesis of carbon nanoparticles using one step green approach and their application as mercuric ion sensor. *Journal of Luminescence* **2015,** *161*, 117.
(61) Shen, J.; Shang, S.; Chen, X.; Wang, D.; Cai, Y. Highly fluorescent N, S-co-doped carbon dots and their potential applications as antioxidants and sensitive probes for Cr (VI) detection. *Sensors and Actuators B: Chemical* **2017,** *248*, 92.
(62) Liu, Y.; Zhou, Q.; Li, J.; Lei, M.; Yan, X. Selective and sensitive chemosensor for lead ions using fluorescent carbon dots prepared from chocolate by one-step hydrothermal method. *Sensors and Actuators B: Chemical* **2016,** *237*, 597.
(63) Wang, Y.; Wu, W.-t.; Wu, M.-b.; Sun, H.-d.; Xie, H.; Hu, C.; Wu, X.-y.; Qiu, J.-s. Yellow-visual fluorescent carbon quantum dots from petroleum coke for the efficient detection of Cu2+ ions. *New Carbon Materials* **2015,** *30* (6), 550.
(64) Shi, L.; Li, Y.; Li, X.; Zhao, B.; Wen, X.; Zhang, G.; Dong, C.; Shuang, S. Controllable synthesis of green and blue fluorescent carbon nanodots for pH and Cu(2+) sensing in living cells. *Biosens Bioelectron* **2016,** *77*, 598.
(65) Zhou, M.; Zhou, Z.; Gong, A.; Zhang, Y.; Li, Q. Synthesis of highly photoluminescent carbon dots via citric acid and Tris for iron(III) ions sensors and bioimaging. *Talanta* **2015,** *143*, 107.
(66) Sun, X.-Y.; Wu, L.-L.; Shen, J.-S.; Cao, X.-G.; Wen, C.; Liu, B.; Wang, H.-Q. Highly selective and sensitive sensing for Al3+ and F− based on green photoluminescent carbon dots. *RSC Advances* **2016,** *6* (99), 97346.
(67) Xu, J.; Zhou, Y.; Cheng, G.; Dong, M.; Liu, S.; Huang, C. Carbon dots as a luminescence sensor for ultrasensitive detection of phosphate and their bioimaging properties. *Luminescence* **2015,** *30* (4), 411.
(68) Li, Z.; Yu, H.; Bian, T.; Zhao, Y.; Zhou, C.; Shang, L.; Liu, Y.; Wu, L.-Z.; Tung, C.-H.; Zhang, T. Highly luminescent nitrogen-doped carbon quantum dots as effective fluorescent probes for mercuric and iodide ions. *Journal of Materials Chemistry C* **2015,** *3* (9), 1922.
(69) Kumar, S.; Venkatramaiah, N.; Patil, S. Fluoranthene Based Derivatives for Detection of Trace Explosive Nitroaromatics. *The Journal of Physical Chemistry C* **2013,** *117* (14), 7236.
(70) Tenhaeff, W. E.; McIntosh, L. D.; Gleason, K. K. Synthesis of Poly(4-vinylpyridine) Thin Films by Initiated Chemical Vapor Deposition (iCVD) for Selective Nanotrench-Based Sensing of Nitroaromatics. *Advanced Functional Materials* **2010,** *20* (7), 1144.

(71) Zhang, L.; Han, Y.; Zhu, J.; Zhai, Y.; Dong, S. Simple and sensitive fluorescent and electrochemical trinitrotoluene sensors based on aqueous carbon dots. *Anal Chem* **2015,** *87* (4), 2033.
(72) Chen, B. B.; Liu, Z. X.; Zou, H. Y.; Huang, C. Z. Highly selective detection of 2,4,6-trinitrophenol by using newly developed terbium-doped blue carbon dots. *Analyst* **2016,** *141* (9), 2676.
(73) Zheng, M.; Liu, S.; Li, J.; Qu, D.; Zhao, H.; Guan, X.; Hu, X.; Xie, Z.; Jing, X.; Sun, Z. Integrating oxaliplatin with highly luminescent carbon dots: an unprecedented theranostic agent for personalized medicine. *Adv Mater* **2014,** *26* (21), 3554.
(74) Shu, Y.; Lu, J.; Mao, Q.-X.; Song, R.-S.; Wang, X.-Y.; Chen, X.-W.; Wang, J.-H. Ionic liquid mediated organophilic carbon dots for drug delivery and bioimaging. *Carbon* **2017,** *114*, 324.
(75) Fu, H.; Ji, Z.; Chen, X.; Cheng, A.; Liu, S.; Gong, P.; Li, G.; Chen, G.; Sun, Z.; Zhao, X.et al. A versatile ratiometric nanosensing approach for sensitive and accurate detection of Hg(2+) and biological thiols based on new fluorescent carbon quantum dots. *Anal Bioanal Chem* **2017,** *409* (9), 2373.
(76) Piliego, C.; Protesescu, L.; Bisri, S. Z.; Kovalenko, M. V.; Loi, M. A. 5.2% efficient PbS nanocrystal Schottky solar cells. *Energy & Environmental Science* **2013,** *6*, 3054.
(77) Gupta, V.; Chaudhary, N.; Srivastava, R.; Sharma, G. D.; Bhardwaj, R.; Chand, S. Luminscent graphene quantum dots for organic photovoltaic devices. *J Am Chem Soc* **2011,** *133* (26), 9960.
(78) Wang, Y.; Zhang, J.; Chen, S.; Zhang, H.; Li, L.; Fu, Z. Surface passivation with nitrogen-doped carbon dots for improved perovskite solar cell performance. *Journal of Materials Science* **2018,** *53* (12), 9180.
(79) Yang, J.; Tang, Q.; Meng, Q.; Zhang, Z.; Li, J.; He, B.; Yang, P. Photoelectric conversion beyond sunny days: all-weather carbon quantum dot solar cells. *Journal of Materials Chemistry A* **2017,** *5* (5), 2143.
(80) Sakdaronnarong, C.; Sangjan, A.; Boonsith, S.; Kim, D. C.; Shin, H. S. Recent Developments in Synthesis and Photocatalytic Applications of Carbon Dots. *Catalysts* **2020,** *10* (3), 320.
(81) Phang, S. J.; Tan, L.-L. Recent advances in carbon quantum dot (CQD)-based two dimensional materials for photocatalytic applications. *Catalysis Science & Technology* **2019,** *9* (21), 5882.
(82) Qu, D.; Zheng, M.; Du, P.; Zhou, Y.; Zhang, L.; Li, D.; Tan, H.; Zhao, Z.; Xie, Z.; Sun, Z. Highly luminescent S, N co-doped graphene quantum dots with broad visible absorption bands for visible light photocatalysts. *Nanoscale* **2013,** *5* (24), 12272.
(83) Schneider, C. A.; Rasband, W. S.; Eliceiri, K. W. NIH Image to ImageJ: 25 years of image analysis. *Nat Methods* **2012,** *9* (7), 671.
(84) Khan, Z. M. S. H.; Saifi, S.; Shumaila; Aslam, Z.; Khan, S. A.; Zulfequar, M. A facile one step hydrothermal synthesis of carbon quantum dots for label -free fluorescence sensing approach to detect picric acid in aqueous solution. *Journal of Photochemistry and Photobiology A: Chemistry* **2020,** *388*.
(85) Yue, J.; Li, L.; Cao, L.; Zan, M.; Yang, D.; Wang, Z.; Chang, Z.; Mei, Q.; Miao, P.; Dong, W. F. Two-Step Hydrothermal Preparation of Carbon Dots for Calcium Ion Detection. *ACS Appl Mater Interfaces* **2019,** *11* (47), 44566.
(86) Zhang, T.; Zhu, J.; Zhai, Y.; Wang, H.; Bai, X.; Dong, B.; Wang, H.; Song, H. A novel mechanism for red emission carbon dots: hydrogen bond dominated molecular states emission. *Nanoscale* **2017,** *9* (35), 13042.
(87) Li, L.; Dong, T. Photoluminescence tuning in carbon dots: surface passivation or/and functionalization, heteroatom doping. *Journal of Materials Chemistry C* **2018,** *6* (30), 7944.

(88) Ludmerczki, R.; Mura, S.; Carbonaro, C. M.; Mandity, I. M.; Carraro, M.; Senes, N.; Garroni, S.; Granozzi, G.; Calvillo, L.; Marras, S.et al. Carbon Dots from Citric Acid and its Intermediates Formed by Thermal Decomposition. *Chemistry* **2019,** *25* (51), 11963.
(89) Dong, Y.; Shao, J.; Chen, C.; Li, H.; Wang, R.; Chi, Y.; Lin, X.; Chen, G. Blue luminescent graphene quantum dots and graphene oxide prepared by tuning the carbonization degree of citric acid. *Carbon* **2012,** *50* (12), 4738.
(90) Wang, S.; Chen, Z.-G.; Cole, I.; Li, Q. Structural evolution of graphene quantum dots during thermal decomposition of citric acid and the corresponding photoluminescence. *Carbon* **2015,** *82*, 304.
(91) Kasprzyk, W.; Swiergosz, T.; Bednarz, S.; Walas, K.; Bashmakova, N. V.; Bogdal, D. Luminescence phenomena of carbon dots derived from citric acid and urea - a molecular insight. *Nanoscale* **2018,** *10* (29), 13889.
(92) Qu, D.; Zheng, M.; Zhang, L.; Zhao, H.; Xie, Z.; Jing, X.; Haddad, R. E.; Fan, H.; Sun, Z. Formation mechanism and optimization of highly luminescent N-doped graphene quantum dots. *Sci Rep* **2014,** *4*, 5294.
(93) Carbonaro, C. M.; Chiriu, D.; Stagi, L.; Casula, M. F.; Thakkar, S. V.; Malfatti, L.; Suzuki, K.; Ricci, P. C.; Corpino, R. Carbon Dots in Water and Mesoporous Matrix: Chasing the Origin of their Photoluminescence. *The Journal of Physical Chemistry C* **2018,** *122* (44), 25638.
(94) Khan, S.; Sharma, A.; Ghoshal, S.; Jain, S.; Hazra, M. K.; Nandi, C. K. Small molecular organic nanocrystals resemble carbon nanodots in terms of their properties. *Chem Sci* **2018,** *9* (1), 175.
(95) Vallan, L.; Urriolabeitia, E. P.; Ruipérez, F.; Matxain, J. M.; Canton-Vitoria, R.; Tagmatarchis, N.; Benito, A. M.; Maser, W. K. Supramolecular-Enhanced Charge Transfer within Entangled Polyamide Chains as the Origin of the Universal Blue Fluorescence of Polymer Carbon Dots. *Journal of the American Chemical Society* **2018,** *140* (40), 12862.
(96) Shan, D.; Hsieh, J. T.; Bai, X.; Yang, J. Citrate-Based Fluorescent Biomaterials. *Adv Healthc Mater* **2018,** *7* (18), e1800532.
(97) Xin, Q.; Liu, Q.; Geng, L.; Fang, Q.; Gong, J. R. Chiral Nanoparticle as a New Efficient Antimicrobial Nanoagent. *Adv Healthc Mater* **2017,** *6* (4).
(98) Liu, Q.; Guo, B.; Rao, Z.; Zhang, B.; Gong, J. R. Strong two-photon-induced fluorescence from photostable, biocompatible nitrogen-doped graphene quantum dots for cellular and deep-tissue imaging. *Nano Lett* **2013,** *13* (6), 2436.
(99) Cai, Q. Y.; Li, J.; Ge, J.; Zhang, L.; Hu, Y. L.; Li, Z. H.; Qu, L. B. A rapid fluorescence "switch-on" assay for glutathione detection by using carbon dots-MnO2 nanocomposites. *Biosens Bioelectron* **2015,** *72*, 31.
(100) Barbooti, M. M.; Al-Sammerrai, D. A. Thermal decomposition of citric acid. *Thermochimica Acta* **1986,** *98*, 119.
(101) Wyrzykowski, D.; Hebanowska, E.; Nowak-Wiczk, G.; Makowski, M.; Chmurzyński, L. Thermal behaviour of citric acid and isomeric aconitic acids. *Journal of Thermal Analysis and Calorimetry* **2010,** *104* (2), 731.
(102) Ehrat, F.; Bhattacharyya, S.; Schneider, J.; Lof, A.; Wyrwich, R.; Rogach, A. L.; Stolarczyk, J. K.; Urban, A. S.; Feldmann, J. Tracking the Source of Carbon Dot Photoluminescence: Aromatic Domains versus Molecular Fluorophores. *Nano Lett* **2017,** *17* (12), 7710.
(103) Wang, H.; Gao, P.; Wang, Y.; Guo, J.; Zhang, K.-Q.; Du, D.; Dai, X.; Zou, G. Fluorescently tuned nitrogen-doped carbon dots from carbon source with different content of carboxyl groups. *APL Materials* **2015,** *3* (8).
(104) Suzuki, K.; Malfatti, L.; Takahashi, M.; Carboni, D.; Messina, F.; Tokudome, Y.; Takemoto, M.; Innocenzi, P. Design of Carbon Dots Photoluminescence through Organo-Functional Silane Grafting for Solid-State Emitting Devices. *Sci Rep* **2017,** *7* (1), 5469.

(105) Wang, F.; Xie, Z.; Zhang, H.; Liu, C.-y.; Zhang, Y.-g. Highly Luminescent Organosilane-Functionalized Carbon Dots. *Advanced Functional Materials* **2011,** *21* (6), 1027.
(106) Innocenzi, P.; Malfatti, L.; Carboni, D. Graphene and carbon nanodots in mesoporous materials: an interactive platform for functional applications. *Nanoscale* **2015,** *7* (30), 12759.
(107) Lin, Y.; Wang, C.; Li, L.; Wang, H.; Liu, K.; Wang, K.; Li, B. Tunable Fluorescent Silica-Coated Carbon Dots: A Synergistic Effect for Enhancing the Fluorescence Sensing of Extracellular Cu(2)(+) in Rat Brain. *ACS Appl Mater Interfaces* **2015,** *7* (49), 27262.
(108) Bichara, L. C.; Lanús, H. E.; Ferrer, E. G.; Gramajo, M. B.; Brandán, S. A. Vibrational Study and Force Field of the Citric Acid Dimer Based on the SQM Methodology. *Advances in Physical Chemistry* **2011,** *2011*, 1.
(109) Askew, F. A.; Tawn, A. R. H. The catalytic pyrolysis of citric acid to itaconic and citraconic acids. *Journal of the Society of Chemical Industry* **1950,** *69* (4), 97.
(110) Sharma, A.; Gadly, T.; Gupta, A.; Ballal, A.; Ghosh, S. K.; Kumbhakar, M. Origin of Excitation Dependent Fluorescence in Carbon Nanodots. *J Phys Chem Lett* **2016,** *7* (18), 3695.
(111) Qian, J.; Quan, F.; Zhao, F.; Wu, C.; Wang, Z.; Zhou, L. Aconitic acid derived carbon dots: Conjugated interaction for the detection of folic acid and fluorescence targeted imaging of folate receptor overexpressed cancer cells. *Sensors and Actuators B: Chemical* **2018,** *262*, 444.
(112) Zhao, F.; Qian, J.; Quan, F.; Wu, C.; Zheng, Y.; Zhou, L. Aconitic acid derived carbon dots as recyclable "on–off–on" fluorescent nanoprobes for sensitive detection of mercury(ii) ions, cysteine and cellular imaging. *RSC Advances* **2017,** *7* (70), 44178.
(113) Ramanan, V.; Subray, S. H.; Ramamurthy, P. A green synthesis of highly luminescent carbon dots from itaconic acid and their application as an efficient sensor for Fe3+ ions in aqueous medium. *New Journal of Chemistry* **2018,** *42* (11), 8933.
(114) Suzuki, K.; Malfatti, L.; Carboni, D.; Loche, D.; Casula, M.; Moretto, A.; Maggini, M.; Takahashi, M.; Innocenzi, P. Energy Transfer Induced by Carbon Quantum Dots in Porous Zinc Oxide Nanocomposite Films. *The Journal of Physical Chemistry C* **2015,** *119* (5), 2837.
(115) Suzuki, K.; Takahashi, M.; Malfatti, L.; Innocenzi, P. Carbon dots in ZnO macroporous films with controlled photoluminescence through defects engineering. *RSC Advances* **2016,** *6* (60), 55393.
(116) Malfatti, L.; Innocenzi, P. Sol-Gel Chemistry for Carbon Dots. *Chem Rec* **2018,** *18* (7-8), 1192.
(117) Xie, Z.; Wang, F.; Liu, C. Y. Organic-inorganic hybrid functional carbon dot gel glasses. *Adv Mater* **2012,** *24* (13), 1716.
(118) Sciortino, A.; Mauro, N.; Buscarino, G.; Sciortino, L.; Popescu, R.; Schneider, R.; Giammona, G.; Gerthsen, D.; Cannas, M.; Messina, F. β-C3N4 Nanocrystals: Carbon Dots with Extraordinary Morphological, Structural, and Optical Homogeneity. *Chemistry of Materials* **2018,** *30* (5), 1695.
(119) Mura, S.; Ludmerczki, R.; Stagi, L.; Garroni, S.; Carbonaro, C. M.; Ricci, P. C.; Casula, M. F.; Malfatti, L.; Innocenzi, P. Integrating sol-gel and carbon dots chemistry for the fabrication of fluorescent hybrid organic-inorganic films. *Sci Rep* **2020,** *10* (1), 4770.
(120) Xia, C.; Zhu, S.; Feng, T.; Yang, M.; Yang, B. Evolution and Synthesis of Carbon Dots: From Carbon Dots to Carbonized Polymer Dots. *Adv Sci (Weinh)* **2019,** *6* (23), 1901316.
(121) Zhou, Y.; Sharma, S. K.; Peng, Z.; Leblanc, R. M. Polymers in Carbon Dots: A Review. *Polymers (Basel)* **2017,** *9* (2), 67.
(122) Liu, J.; Geng, Y.; Li, D.; Yao, H.; Huo, Z.; Li, Y.; Zhang, K.; Zhu, S.; Wei, H.; Xu, W.et al. Deep Red Emissive Carbonized Polymer Dots with Unprecedented Narrow Full Width at Half Maximum. *Adv Mater* **2020,** *32* (17), 1906641.

(123) Song, Y.; Zhu, S.; Zhang, S.; Fu, Y.; Wang, L.; Zhao, X.; Yang, B. Investigation from chemical structure to photoluminescent mechanism: a type of carbon dots from the pyrolysis of citric acid and an amine. *Journal of Materials Chemistry C* **2015,** *3* (23), 5976.
(124) Zhu, S.; Song, Y.; Shao, J.; Zhao, X.; Yang, B. Non-Conjugated Polymer Dots with Crosslink-Enhanced Emission in the Absence of Fluorophore Units. *Angew Chem Int Ed Engl* **2015,** *54* (49), 14626.
(125) Schneider, J.; Reckmeier, C. J.; Xiong, Y.; von Seckendorff, M.; Susha, A. S.; Kasák, P.; Rogach, A. L. Molecular Fluorescence in Citric Acid-Based Carbon Dots. *The Journal of Physical Chemistry C* **2017,** *121* (3), 2014.
(126) Xia, C.; Tao, S.; Zhu, S.; Song, Y.; Feng, T.; Zeng, Q.; Liu, J.; Yang, B. Hydrothermal Addition Polymerization for Ultrahigh-Yield Carbonized Polymer Dots with Room Temperature Phosphorescence via Nanocomposite. *Chemistry* **2018,** *24* (44), 11303.
(127) Halpern, J. M.; Urbanski, R.; Weinstock, A. K.; Iwig, D. F.; Mathers, R. T.; von Recum, H. A. A biodegradable thermoset polymer made by esterification of citric acid and glycerol. *J Biomed Mater Res A* **2014,** *102* (5), 1467.
(128) Mariano-Torres, J. A.; López-Marure, A.; Domiguez-Sánchez, M. Á. Synthesis and characterization of polymers based on citric acid and glycerol: Its application in non-biodegradable polymers. *Dyna* **2015,** *82* (190), 53.
(129) Khan, S.; Jain, S.; Nandi, C. K. Towards Understanding Citric Acid Derived High Quantum Yield Molecular Fluorophores: From Carbon Dots to Spherical Organic Nanocrystals. *Journal of Material Science & Engineering* **2018,** *07* (05), 1000490.
(130) Mura, S.; Stagi, L.; Malfatti, L.; Carbonaro, C. M.; Ludmerczki, R.; Innocenzi, P. Modulating the Optical Properties of Citrazinic Acid through the Monomer-to-Dimer Transformation. *J Phys Chem A* **2020,** *124* (1), 197.
(131) Chen, X.; Wu, S.; Yi, M.; Ge, J.; Yin, G.; Li, X. Preparation and Physicochemical Properties of Blend Films of Feather Keratin and Poly(vinyl alcohol) Compatibilized by Tris(hydroxymethyl)aminomethane. *Polymers (Basel)* **2018,** *10*, 1054.
(132) Kong, J.; Yu, S. Fourier transform infrared spectroscopic analysis of protein secondary structures. *Acta Biochim Biophys Sin (Shanghai)* **2007,** *39* (8), 549.
(133) Iwamoto, R.; Murase, H. Infrared spectroscopic study of the interactions of nylon-6 with water. *Journal of Polymer Science Part B: Polymer Physics* **2003,** *41* (14), 1722.
(134) Emmons, E. D.; Fallas, J. C.; Kamisetty, V. K.; Chien, W. M.; Covington, A. M.; Chellappa, R. S.; Gramsch, S. A.; Hemley, R. J.; Chandra, D. High-pressure Raman spectroscopy of tris(hydroxymethyl)aminomethane. *J Phys Chem B* **2010,** *114* (17), 5649.
(135) Katon, J. E.; McDevitt, N. T. The vibrational spectra of propynoic acid and sodium propynoate. *Spectrochimica Acta* **1965,** *21* (10), 1717.
(136) Lin-Vien, D.; Colthup, N.; Fateley, W.; Grassell, J. *The Handbook of Infrared and Raman Characteristic Frequencies of Organic Molecules*; 1st ed.; Academic Press: London, 1991.
(137) Gremlich, H.-U.; Yan, B. *Infrared and Raman Spectroscopy of Biological Materials*; 1st ed.; Marcel Dekker, Inc: New York-Basel, 2001.
(138) Carbonaro, C. M.; Thakkar, S. V.; Ludmerczki, R.; Olla, C.; Pinna, A.; Loche, D.; Malfatti, L.; Cesare Marincola, F.; Casula, M. F. How porosity affects the emission of fluorescent carbon dot-silica porous composites. *Microporous and Mesoporous Materials* **2020,** *305*, 110302.
(139) Zholobak, N. M.; Popov, A. L.; Shcherbakov, A. B.; Popova, N. R.; Guzyk, M. M.; Antonovich, V. P.; Yegorova, A. V.; Scrypynets, Y. V.; Leonenko, II; Baranchikov, A. Y.et al. Facile fabrication of luminescent organic dots by thermolysis of citric acid in urea melt, and their use for cell staining and polyelectrolyte microcapsule labelling. *Beilstein J Nanotechnol* **2016,** *7*, 1905.
(140) Messina, F.; Sciortino, L.; Popescu, R.; Venezia, A. M.; Sciortino, A.; Buscarino, G.; Agnello, S.; Schneider, R.; Gerthsen, D.; Cannas, M.et al. Fluorescent nitrogen-rich carbon

nanodots with an unexpected β-C3N4nanocrystalline structure. *Journal of Materials Chemistry C* **2016,** *4* (13), 2598.
(141) Qu, D.; Sun, Z. The formation mechanism and fluorophores of carbon dots synthesized via a bottom-up route. *Materials Chemistry Frontiers* **2020,** *4* (2), 400.
(142) Kottegoda, N.; Sandaruwan, C.; Perera, P.; Madusanka, N.; Karunaratne, V. Modified Layered Nanohybrid Structures for the Slow Release of Urea. *Nanoscience &Nanotechnology-Asia* **2015,** *4* (2), 94.
(143) Manivannan, M.; Rajendran, S. Investigation of inhibitive action of urea-Zn2+ system in the corrosion control of carbon steel in sea water. *International Journal of Engineering Science and Technology* **2011,** *3* (11), 8048.
(144) Schaber, P. M.; Colson, J.; Higgins, S.; Thielen, D.; Anspach, B.; Brauer, J. Thermal decomposition (pyrolysis) of urea in an open reaction vessel. *Thermochimica Acta* **2004,** *424* (1-2), 131.
(145) Nakata, K.; Fujishima, A. TiO2 photocatalysis: Design and applications. *Journal of Photochemistry and Photobiology C: Photochemistry Reviews* **2012,** *13* (3), 169.
(146) Daghrir, R.; Drogui, P.; Robert, D. Modified TiO2For Environmental Photocatalytic Applications: A Review. *Industrial & Engineering Chemistry Research* **2013,** *52* (10), 3581.
(147) Mura, S.; Seddaiu, G.; Bacchini, F.; Roggero, P. P.; Greppi, G. F. Advances of nanotechnology in agro-environmental studies. *Italian Journal of Agronomy* **2013,** *8* (3), 127.
(148) Guo, W.; Liu, X.; Huo, P.; Gao, X.; Wu, D.; Lu, Z.; Yan, Y. Hydrothermal synthesis spherical TiO2 and its photo-degradation property on salicylic acid. *Applied Surface Science* **2012,** *258* (18), 6891.
(149) Imran, M.; Riaz, S.; Naseem, S. Synthesis and Characterization of Titania Nanoparticles by Sol-gel Technique. *Materials Today: Proceedings* **2015,** *2* (10), 5455.
(150) Ganganagappa, N.; Bychapur Siddaiah, G.; Phattepur, H. Synthesis and Characterisation of Mesoporous TiO2 Nanoparticles by Novel Surfactant Assisted Sol-gel Method for the Degradation of Organic Compounds. *Periodica Polytechnica Chemical Engineering* **2018,** *63* (1), 85.
(151) Duvarci, Ö. Ç.; Çiftçioğlu, M. Preparation and characterization of nanocrystalline titania powders by sonochemical synthesis. *Powder Technology* **2012,** *228*, 231.
(152) Prakash, T.; Navaneethan, M.; Archana, J.; Ponnusamy, S.; Muthamizhchelvan, C.; Hayakawa, Y. Synthesis of TiO2 nanoparticles with mesoporous spherical morphology by a wet chemical method. *Materials Letters* **2012,** *82*, 208.
(153) Pelaez, M.; Nolan, N. T.; Pillai, S. C.; Seery, M. K.; Falaras, P.; Kontos, A. G.; Dunlop, P. S. M.; Hamilton, J. W. J.; Byrne, J. A.; O'Shea, K.et al. A review on the visible light active titanium dioxide photocatalysts for environmental applications. *Applied Catalysis B: Environmental* **2012,** *125*, 331.
(154) Henderson, M. A. A surface science perspective on TiO2 photocatalysis. *Surface Science Reports* **2011,** *66*, 185.
(155) Cai, S.-S.; Stark, J. Evaluation of five fluorescent dyes and triethyl phosphate as atmospheric tracers of agricultural sprays. *Journal of Environmental Science and Health, Part B* **1997,** *32* (6), 969.
(156) Fujishima, A.; Honda, K. Electrochemical photolysis of water at a semiconductor electrode. *Nature* **1972,** *238* (5358), 37.
(157) Gupta, S. M.; Tripathi, M. A review of TiO2 nanoparticles. *Chinese Science Bulletin* **2011,** *56* (16), 1639.
(158) Xu, A.-W.; Gao, Y.; Liu, H.-Q. The Preparation, Characterization, and their Photocatalytic Activities of Rare-Earth-Doped TiO2 Nanoparticles. *Journal of Catalysis* **2002,** *207* (2), 151.

(159) Pookmanee, P.; Phanichphant, S. Titanium dioxide powder prepared by a sol-gel method. *Journal of Ceramic Processing Research* **2009,** *10* (2), 167.
(160) Akpan, U. G.; Hameed, B. H. The advancements in sol–gel method of doped-TiO2 photocatalysts. *Applied Catalysis A: General* **2010,** *375* (1), 1.
(161) Alphas Jebasingh, J.; Stanley, R.; Manisha Vidyavathy, S. Low temperature titania nano particles for high performance solar photo degradation. *Optik* **2019,** *179*, 901.
(162) Vassalini, I.; Gjipalaj, J.; Crespi, S.; Gianoncelli, A.; Mella, M.; Ferroni, M.; Alessandri, I. Alginate-Derived Active Blend Enhances Adsorption and Photocatalytic Removal of Organic Pollutants in Water. *Advanced Sustainable Systems* **2020**, DOI:10.1002/adsu.201900112 10.1002/adsu.201900112, 1900112.
(163) Mura, S.; Jiang, Y.; Vassalini, I.; Gianoncelli, A.; Alessandri, I.; Granozzi, G.; Calvillo, L.; Senes, N.; Enzo, S.; Innocenzi, P.et al. Graphene Oxide/Iron Oxide Nanocomposites for Water Remediation. *ACS Applied Nano Materials* **2018,** *1* (12), 6724.
(164) Zheng, J.; Xie, Y.; Wei, Y.; Yang, Y.; Liu, X.; Chen, Y.; Xu, B. An Efficient Synthesis and Photoelectric Properties of Green Carbon Quantum Dots with High Fluorescent Quantum Yield. *Nanomaterials (Basel)* **2020,** *10*, 82.
(165) Zheng, K.; Li, X.; Chen, M.; Gong, Y.; Tang, A.; Wang, Z.; Wei, Z.; Guan, L.; Teng, F. Controllable synthesis highly efficient red, yellow and blue carbon nanodots for photo-luminescent light-emitting devices. *Chemical Engineering Journal* **2020,** *380*, 122503.
(166) Han, Z.; Ni, Y.; Ren, J.; Zhang, W.; Wang, Y.; Xie, Z.; Zhou, S.; Yu, S. F. Highly efficient and ultra-narrow bandwidth orange emissive carbon dots for microcavity lasers. *Nanoscale* **2019,** *11* (24), 11577.
(167) Ding, H.; Wei, J. S.; Zhong, N.; Gao, Q. Y.; Xiong, H. M. Highly Efficient Red-Emitting Carbon Dots with Gram-Scale Yield for Bioimaging. *Langmuir* **2017,** *33* (44), 12635.
(168) Bao, X.; Yuan, Y.; Chen, J.; Zhang, B.; Li, D.; Zhou, D.; Jing, P.; Xu, G.; Wang, Y.; Hola, K.et al. In vivo theranostics with near-infrared-emitting carbon dots-highly efficient photothermal therapy based on passive targeting after intravenous administration. *Light Sci Appl* **2018,** *7*, 91.
(169) Gan, Z.; Xu, H.; Hao, Y. Mechanism for excitation-dependent photoluminescence from graphene quantum dots and other graphene oxide derivates: consensus, debates and challenges. *Nanoscale* **2016,** *8* (15), 7794.
(170) Zhu, S.; Song, Y.; Zhao, X.; Shao, J.; Zhang, J.; Yang, B. The photoluminescence mechanism in carbon dots (graphene quantum dots, carbon nanodots, and polymer dots): current state and future perspective. *Nano Research* **2015,** *8* (2), 355.
(171) Cayuela, A.; Soriano, M. L.; Carrillo-Carrion, C.; Valcarcel, M. Semiconductor and carbon-based fluorescent nanodots: the need for consistency. *Chem Commun (Camb)* **2016,** *52* (7), 1311.
(172) Bhunia, S. K.; Saha, A.; Maity, A. R.; Ray, S. C.; Jana, N. R. Carbon nanoparticle-based fluorescent bioimaging probes. *Sci Rep* **2013,** *3*, 1473.
(173) Bao, L.; Liu, C.; Zhang, Z. L.; Pang, D. W. Photoluminescence-tunable carbon nanodots: surface-state energy-gap tuning. *Adv Mater* **2015,** *27* (10), 1663.
(174) Hu, S.; Trinchi, A.; Atkin, P.; Cole, I. Tunable photoluminescence across the entire visible spectrum from carbon dots excited by white light. *Angew Chem Int Ed Engl* **2015,** *54* (10), 2970.
(175) Jiang, B. P.; Zhou, B.; Shen, X. C.; Yu, Y. X.; Ji, S. C.; Wen, C. C.; Liang, H. Selective Probing of Gaseous Ammonia Using Red-Emitting Carbon Dots Based on an Interfacial Response Mechanism. *Chemistry* **2015,** *21* (52), 18993.
(176) Craciun, A. M.; Diac, A.; Focsan, M.; Socaci, C.; Magyari, K.; Maniu, D.; Mihalache, I.; Veca, L. M.; Astilean, S.; Terec, A. Surface passivation of carbon nanoparticles with p-phenylenediamine towards photoluminescent carbon dots. *RSC Advances* **2016,** *6* (62), 56944.

(177) Sun, S.; Zhang, L.; Jiang, K.; Wu, A.; Lin, H. Toward High-Efficient Red Emissive Carbon Dots: Facile Preparation, Unique Properties, and Applications as Multifunctional Theranostic Agents. *Chemistry of Materials* **2016,** *28* (23), 8659.
(178) Yuan, F.; Wang, Z.; Li, X.; Li, Y.; Tan, Z.; Fan, L.; Yang, S. Bright Multicolor Bandgap Fluorescent Carbon Quantum Dots for Electroluminescent Light-Emitting Diodes. *Adv Mater* **2017,** *29*, 1604436.
(179) Zhao, D.; Liu, X.; Wei, C.; Qu, Y.; Xiao, X.; Cheng, H. One-step synthesis of red-emitting carbon dots via a solvothermal method and its application in the detection of methylene blue. *RSC Advances* **2019,** *9* (51), 29533.
(180) Pawar, S.; Kaja, S.; Nag, A. Red-Emitting Carbon Dots as a Dual Sensor for In(3+) and Pd(2+) in Water. *ACS Omega* **2020,** *5* (14), 8362.
(181) Yu, P.; Wen, X.; Toh, Y.-R.; Tang, J. Temperature-Dependent Fluorescence in Carbon Dots. *The Journal of Physical Chemistry C* **2012,** *116* (48), 25552.
(182) Ali, H.; Bhunia, S. K.; Dalal, C.; Jana, N. R. Red Fluorescent Carbon Nanoparticle-Based Cell Imaging Probe. *ACS Appl Mater Interfaces* **2016,** *8* (14), 9305.
(183) Jiang, K.; Sun, S.; Zhang, L.; Lu, Y.; Wu, A.; Cai, C.; Lin, H. Red, green, and blue luminescence by carbon dots: full-color emission tuning and multicolor cellular imaging. *Angew Chem Int Ed Engl* **2015,** *54* (18), 5360.
(184) Ding, H.; Yu, S. B.; Wei, J. S.; Xiong, H. M. Full-Color Light-Emitting Carbon Dots with a Surface-State-Controlled Luminescence Mechanism. *ACS Nano* **2016,** *10* (1), 484.
(185) Wang, C.; Jiang, K.; Wu, Q.; Wu, J.; Zhang, C. Green Synthesis of Red-Emitting Carbon Nanodots as a Novel "Turn-on" Nanothermometer in Living Cells. *Chemistry* **2016,** *22* (41), 14475.
(186) Wang, H.; Sun, C.; Chen, X.; Zhang, Y.; Colvin, V. L.; Rice, Q.; Seo, J.; Feng, S.; Wang, S.; Yu, W. W. Excitation wavelength independent visible color emission of carbon dots. *Nanoscale* **2017,** *9* (5), 1909.
(187) Sciortino, A.; Marino, E.; Dam, B.; Schall, P.; Cannas, M.; Messina, F. Solvatochromism Unravels the Emission Mechanism of Carbon Nanodots. *J Phys Chem Lett* **2016,** *7* (17), 3419.
(188) Mel'nik, I. V.; Lyashenko, O. V.; Zub, Y. L.; Chuiko, A. A.; Cauzzi, D.; Predieri, G. Synthesis of alkoxysilanes as starting substances for preparation of new materials by the sol-gel procedure. Silanes with urea functional group. *Russian Journal of General Chemistry* **2004,** *74* (11), 1658.
(189) Singh, P.; Singh, M. K.; Beg, Y. R.; Nishad, G. R. A review on spectroscopic methods for determination of nitrite and nitrate in environmental samples. *Talanta* **2019,** *191*, 364.
(190) Quan, Z.; Huang, B.; Lu, C.; Shi, Y.; Chen, X.; Zhang, H.; Fang, Y. The fate of fertilizer nitrogen in a high nitrate accumulated agricultural soil. *Sci Rep* **2016,** *5*, 21539.
(191) *Background document for development of WHO Guidelines for Drinking-water Quality*; WHO Press, World Health Organization: Geneva, 2011.
(192) Nolan, B. T.; Stoner, J. D. Nutrients in Groundwaters of the Conterminous United States, 1992−1995. *Environmental Science & Technology* **2000,** *34* (7), 1156.
(193) Schullehner, J.; Stayner, L.; Hansen, B. Nitrate, Nitrite, and Ammonium Variability in Drinking Water Distribution Systems. *Int J Environ Res Public Health* **2017,** *14*, 276.
(194) Appelo, C. A. J.; Postma, D. *Geochemistry, Groundwater and Pollution* 2nd ed.; A.A. Balkema Publishers: Leiden, The Netherlands, 2005.
(195) Kim, K. T.; Kim, H. W.; Chang, H. Y.; Lim, B. T.; Park, H. B.; Kim, Y. S. Corrosion Inhibiting Mechanism of Nitrite Ion on the Passivation of Carbon Steel and Ductile Cast Iron for Nuclear Power Plants. *Advances in Materials Science and Engineering* **2015,** *2015*, 408138.

(196) Mohammadi, A.; Yazdanbakhsh, M. R.; Farahnak, L. Synthesis and evaluation of changes induced by solvent and substituent in electronic absorption spectra of some azo disperse dyes. *Spectrochim Acta A Mol Biomol Spectrosc* **2012,** *89*, 238.
(197) Cammack, R.; Joannou, C. L.; Cui, X.-Y.; Torres Martinez, C.; Maraj, S. R.; Hughes, M. N. Nitrite and nitrosyl compounds in food preservation. *Biochimica et Biophysica Acta (BBA) - Bioenergetics* **1999,** *1411* (2-3), 475.
(198) Jensen, F. B. Nitrite disrupts multiple physiological functions in aquatic animals. *Comparative Biochemistry and Physiology Part A: Molecular & Integrative Physiology* **2003,** *135* (1), 9.
(199) *Guidelines for drinking-water quality*; 4th ed.; WHO Press, World Health Organization: Geneva, 2011.
(200) Wang, Q. H.; Yu, L. J.; Liu, Y.; Lin, L.; Lu, R. G.; Zhu, J. P.; He, L.; Lu, Z. L. Methods for the detection and determination of nitrite and nitrate: A review. *Talanta* **2017,** *165*, 709.
(201) Wang, G. Spectrophotometric determination of nitrate and nitrite in water and some fruit samples using column preconcentration. *Talanta* **1998,** *46* (4), 671.
(202) Luo, Y.; Wen, G.; Dong, J.; Liu, Q.; Liang, A.; Jiang, Z. SERS detection of trace nitrite ion in aqueous solution based on the nitrosation reaction of rhodamine 6G molecular probe. *Sensors and Actuators B: Chemical* **2014,** *201*, 336.
(203) Ren, W.; Mura, S.; Irudayaraj, J. M. K. Modified graphene oxide sensors for ultra-sensitive detection of nitrate ions in water. *Talanta* **2015,** *143*, 234.
(204) Li, M.; Wang, H.; Zhang, X.; Zhang, H.-s. Development of a new fluorescent probe: 1,3,5,7-tetramethyl-8-(4′-aminophenyl)-4,4-difluoro-4-bora-3a,4a-diaza-s-indacence for the determination of trace nitrite. *Spectrochimica Acta Part A: Molecular and Biomolecular Spectroscopy* **2004,** *60* (4), 987.
(205) Doroodmand, M. M.; Askari, M. Synthesis of a novel nitrogen-doped carbon dot by microwave-assisted carbonization method and its applications as selective probes for optical pH (acidity) sensing in aqueous/nonaqueous media, determination of nitrate/nitrite, and optical recognition of NOX gas. *Anal Chim Acta* **2017,** *968*, 74.
(206) Feng, Z.; Li, Z.; Zhang, X.; Shi, Y.; Zhou, N. Nitrogen-Doped Carbon Quantum Dots as Fluorescent Probes for Sensitive and Selective Detection of Nitrite. *Molecules* **2017,** *22* (12), 2061.
(207) Lin, H.; Ding, L.; Zhang, B.; Huang, J. Detection of nitrite based on fluorescent carbon dots by the hydrothermal method with folic acid. *R Soc Open Sci* **2018,** *5* (5), 172149.
(208) Zan, M.; Rao, L.; Huang, H.; Xie, W.; Zhu, D.; Li, L.; Qie, X.; Guo, S.-S.; Zhao, X.-Z.; Liu, W.et al. A strong green fluorescent nanoprobe for highly sensitive and selective detection of nitrite ions based on phosphorus and nitrogen co-doped carbon quantum dots. *Sensors and Actuators B: Chemical* **2018,** *262*, 555.
(209) Bhattacharya, S.; Sarkar, R.; Chakraborty, B.; Porgador, A.; Jelinek, R. Nitric Oxide Sensing through Azo-Dye Formation on Carbon Dots. *ACS Sens* **2017,** *2* (8), 1215.
(210) Liu, Y.; Luo, S.; Wu, P.; Ma, C.; Wu, X.; Xu, M.; Li, W.; Liu, S. Hydrothermal synthesis of green fluorescent nitrogen doped carbon dots for the detection of nitrite and multicolor cellular imaging. *Anal Chim Acta* **2019,** *1090*, 133.
(211) Jia, J.; Lu, W.; Li, L.; Gao, Y.; Jiao, Y.; Han, H.; Dong, C.; Shuang, S. Orange-emitting N-doped carbon dots as fluorescent and colorimetric dual-mode probes for nitrite detection and cellular imaging. *J Mater Chem B* **2020,** *8* (10), 2123.
(212) Abdel-Rahman, F.; Okeremgbo, B.; Alhamadah, F.; Jamadar, S.; Anthony, K.; Saleh, M. A. Caenorhabditis elegans as a model to study the impact of exposure to light emitting diode (LED) domestic lighting. *J Environ Sci Health A Tox Hazard Subst Environ Eng* **2017,** *52* (5), 433.

(213) Shah, H.; Xin, Q.; Jia, X.; Gong, J. R. Single precursor-based luminescent nitrogen-doped carbon dots and their application for iron (III) sensing. *Arabian Journal of Chemistry* **2019,** *12* (7), 1083.
(214) Salinas-Castillo, A.; Ariza-Avidad, M.; Pritz, C.; Camprubi-Robles, M.; Fernandez, B.; Ruedas-Rama, M. J.; Megia-Fernandez, A.; Lapresta-Fernandez, A.; Santoyo-Gonzalez, F.; Schrott-Fischer, A.et al. Carbon dots for copper detection with down and upconversion fluorescent properties as excitation sources. *Chem Commun (Camb)* **2013,** *49* (11), 1103.
(215) Yoo, D.; Park, Y.; Cheon, B.; Park, M. H. Carbon Dots as an Effective Fluorescent Sensing Platform for Metal Ion Detection. *Nanoscale Res Lett* **2019,** *14* (1), 272.
(216) Ottaviani, M.; Bonadonna, L. Metodi analitici di riferimento per le acque destinate al consumo umano ai sensi del D.L.vo 31/2001 Metodi chimici. *Istituto Superiore di Sanità* **2007**.
(217) Griess, P. XLVI.—On a new class of organic compounds in which hydrogen is replaced by nitrogen. *J. Chem. Soc.* **1865,** *18*, 298.
(218) Zhu, H.; Peng, S.; Jiang, W. Electrochemical properties of PANI as single electrode of electrochemical capacitors in acid electrolytes. *ScientificWorldJournal* **2013,** *2013*, 940153.
(219) Dıblan, S.; Kadiroğlu, P.; Aydemir, L. Y. Ft-Ir Spectroscopy Characterization and Chemometric Evaluation of Legumes Extracted with Different Solvents. *Food and Health* **2018,** *4* (2), 80.
(220) Silva, S. D.; Feliciano, R. P.; Boas, L. V.; Bronze, M. R. Application of FTIR-ATR to Moscatel dessert wines for prediction of total phenolic and flavonoid contents and antioxidant capacity. *Food Chem* **2014,** *150*, 489.
(221) Abdullah, S.; Rahman, R.; Mohamad, A.; Mustafa, M.; Khadum, A. Removal of Mixed Heavy Metals by Hydroxide Precipitation. *Jumal Kejunneraan* **1999,** *11* (2), 85.

La borsa di dottorato è stata cofinanziata con risorse del
Programma Operativo Nazionale Ricerca e Innovazione 2014-2020 (CCI 2014IT16M2OP005),
Fondo Sociale Europeo, Azione I.1 “Dottorati Innovativi con caratterizzazione Industriale”

UNIONE EUROPEA
Fondo Sociale Europeo